Experiments versus simulations: modelling of instrumentation for X-ray scattering experiments.

by Jana Baltser

A dissertation for the degree of Doctor of Philosophy in physics

Nanoscience Center
Niels Bohr Institute
University of Copenhagen

March 2013

Publications by Jana Baltser

J. Baltser, E. Knudsen, A. Vickery, O. Chubar, A. Snigirev, G. Vaughan, R. Feidenhans'l, K. Lefmann, *Advanced simulations of X-ray beam propagation through CRL transfocators using ray-tracing and wavefront propagation methods*, Proc. SPIE 8141 (2011), 814111

A. Fluerasu, O. Chubar, K. Kaznatcheev, J. Baltser, L. Wiegart, K. Evans-Lutterodt, M. Carlucci-Dayton, L. Berman, *Analysis of the optical design of the NSLS-II coherent hard X-ray beamline*, Proc. SPIE 8141 (2011), 81410J

E. Knudsen, A. Prodi, J. Baltser, M. Thomsen, P. Willednrup, M. Sanchez del Rio, C. Ferrero, E. Farhi, K. Haldrup, A. Vickery, R. Feidenhans'l, K. Mortensen, M. Meedom Nielsen, H. Friis Poulsen, S. Schmidt, K. Lefmann, *McXtrace - a Monte Carlo software package for simulating x-ray optics, beamlines, and experiments*, J. Applied Cryst. (2012), to be published

O. Chubar, L. Berman, Y. S. Chu, A. Fluerasu, S. Hulbert, M. Idir, K. Kaznatcheev, D. Shapiro, Q. Shen, J. Baltser, *Development of partially-coherent wavefront propagation simulation methods for 3d and 4th generation synchrotron radiation sources*, Proc. SPIE 8141, 814107(2011)

J. Gulden, S. O. Mariager, A. P. Mancuso, O. M. Yefanov, J. Baltser, P. Krogstrup, J. Patommel, M. Burghammer, R. Feidenhans'l, I. A. Vartanyants, *Coherent X-ray nanodiffraction on single GaAs nanowires*, Phys. Solidi A 208, No. 11, 2495-2498 (2011)

O. Chubar, A. Fluerasu, Y. S. Chu, L. Bermann, L. Wiegart, W-K. Lee, J. Baltser, *Experimental characterization of X-ray transverse coherence in the presence of beam transport optics*, Proc. SRI (2012)

Preamble

The world of instrumentation utilising X-ray radiation is expanding: new technological advances entail state-of-the-art materials, industrial application of which yields novel devices in this field. It leads to more sophisticated instruments and beamlines, which in turn results in more complex experiments. Every step of this cycle requires accurate calculation, and that is where simulation plays an important role.

With the advert of modern computers and technologies, simulation has become a very powerful tool, which allows prediction of experimental outcomes with high precision and accuracy, optimisation and improvement of existing setups and can even reveal otherwise unattainable qualities of a modelled instrument by, for instance, disentangling various features of the system. X-rays beamlines must be constructed in the most cost-efficient way, as this field is extremely expensive, hence modelling helps achieving optimal solutions. At present, numerical modelling is truly valuable, therefore it is given a lot of attention.

Despite the high significance of simulations, there are only a handful of software packages available for the X-ray range. There are two approaches to modelling such radiation and its interaction with matter: one based on the laws of geometric optics, ray-tracing, and another one formulated by the laws of physical optics and Fourier integrals, wavefronts propagation.

The physical optics method is represented by the Synchrotron Radiation Workshop code [1] and PHASE [2], [3]; this method provides extremely accurate results for those simulations considering the wave nature of X-rays, although due to the complexity of calculations the simulation time can be very long. The licenses for these packages are proprietary, which limits their availability.

The ray-tracing method is represented by software such as SHADOW [4], [5] and RAY [6]; it provides reliable results for those modelling cases that emphasise the particle nature of X-rays. SHADOW is well known and widely used among X-ray scientists. It is built under an open source license, therefore it is one of the most available ray-tracing packages. Areas for development were identified in SHADOW, for example, improving the usability of its interface and increasing the number of photon rays. Thus, a necessity of a new ray-tracing code that would develop along with SHADOW in the atmosphere of friendly competition, be user-friendly and freely available has led to the appearance of a new package: McXtrace.

The work that underlay the present dissertation was dedicated primarily to software development (defining optical components that are set into a beamline) and benchmarking virtual experiments simulated with McXtrace against physical experiments and other simulation packages. In order to coherently present the projects, the dissertation is structured in the following fashion: one half of it is focused on the theoretical basis and description of methods , whereas the second half presents the simulation projects, their analysis and obtained results.

The first chapter briefly introduces the area of X-ray scattering and provides some basic definitions of the method. The second chapter shows how the Monte Carlo simulation technique can be applied to ray-tracing, explains

the structure of McXtrace and gives an example of how the actual creation of a component can be done. The third chapter introduces in finer details the generation of synchrotron radiation, whose precise modelling is explained via the wavefronts propagation package SRW. Chapter four shows the simulation of the small-angle scattering instrument: the X-ray beam's propagation was measured experimentally, a model of the instrument was then implemented in McXtrace, whose results were benchmarked against those obtained empirically. An interpretation of the simulation results aided in deeper understanding of the instrument's geometry. Chapter five presents simulations of a transfocator, a novel and practical device with a growing popularity, the performance of which was modelled by both McXtrace and SRW. The two methods produced comparable results, although SRW provided a better agreement with the experiment. Benchmarking the simulation results from two packages against one another identified a McXtrace component that requires additional development, which is an excellent opportunity for further improvement of the package. The results of this project were presented at the SPIE conference in San Diego in August 2011, and later were published in the conference proceedings journal. The sixth chapter describes McXtrace simulations of a series of focusing experiments: a compound refractive lens and a kinoform lens were tested in various setups at a synchrotron. The subsequent comparison of the simulated and experimental results shows an excellent agreement, which characterises McXtrace as reliable software. To finalise the dissertation, chapter seven gives the summary conclusions and the author's outlook on a general development of simulation methods within the present research area.

The component codes written by the author along with the instrument codes used in the simulations are provided in the appendices.

Acknowledgements

A great many people have helped to make my Ph.D. possible, so I'll do my best not to leave anyone out; anyone unfairly omitted of course has my apologies as well as my thanks.

Firstly, my great supervisors Kim Lefmann and Robert Feidenhans'l have welcomed me in the world of X-ray physics, outlined my path in it and guided me thoroughly through the rough corners of the trajectory, of which I am sincerely grateful. The two people working nearest to me, Erik B. Knudsen and Jesper B. Jensen, have provided so much guidance, have shown so much patience and were always there to answer my never ending questions. I have been very lucky to work with each of them. The people involved with the McXtrace project (partly or fully), Andrea Prodi and Peter K. Willendrup, have provided favourable inspiration and good mood, aside from other scientific help.

A big thanks goes to Karsten Joensen, the founder of SAXSLAB ApS, who has not only helped with data acquisition for further modelling of the SAXS instrument, but has also provided a good deal of fruitful discussions. Carsten Cooper-Jensen and Anette Vickery were so kind to help with the SAXS project as well.

The help of other people directly or indirectly involved in the McXtrace project and external collaborators from the ESRF, particularly Kell Mortensen, Lise Arleth, Henning F. Poulsen, Søren Schmidt, Claudio Ferrero, Manuel Sanchez del Rio and Niccolò Canestrari, is highly appreciated.

My Ph. D. work couldn't have been done without the enthusiasm from my colleagues during the overseas visit to Brookhaven National Laboratory, therefore I genuinely thank Andrei Fluerasu and Lutz Wiegart for the wonderful early morning/ late evening discussions during long hours of commute between New York City and Brookhaven. A special warm-hearted gratitude is given to Dr. Oleg Chubar not only for his profound insight into my research, his valuable guidance and immense help, but also for his unconventional style of mentoring and emotional support.

Last but not least, great thanks go to my wonderful family, particularly to my father, Arkady Baltser, for igniting the initial interest in physics in me ever since I was very little. My dearest friends have expressed unbelievable support, of which I am honoured. A particular appreciation goes to Dr. Thomas P. Burton, whose generous support and encouragement have helped tremendously to pass through the darker stages of the thesis writing process, and whose wise corrections and notes made this dissertation and my writing style in general much more elegant.

Contents

Chapter 1

Introduction

In this chapter the basics of X-ray scattering as a research tool are described. Firstly, the history back to the first scientific postulates of the nature of light is traced, which eventually leads to the discovery of X-rays and its wide usage. Secondly, the concept of generation of X-rays at synchrotron sources is introduced, as well as the principles of delivery of produced beams through optical systems of synchrotron beamlines. Thirdly, the general method of X-ray scattering is presented, revealing what kind of experiments it could be applied for, which sorts of samples could be investigated and, of course, the purpose of utilising X-ray scattering - something unique that makes researchers choose this technique over a vast variety of others. Fourthly, some of the X-ray detection systems are covered.

1.1 Historical discovery and development of scientific interest

From its ancient history, mankind has been constantly exploring the world, asking questions about the nature of the universe and gradually finding answers. This has maintained a strong interest and kept expanding the quest for knowledge. People were particularly fascinated by light, now known to be part of the spectrum of electromagnetic radiation. It was Newton who first developed a theory in the 17th century that light consisted of small particles of energy - a point of view which was opposed by Huygens, who proposed light to have a wave nature instead. Both theories had legitimate proofs that it was certain that both points of view were reasonable. As unimaginable as it seemed at first sight, light does indeed behave as particles in some cases and as waves in others. The modern point of view concludes that light has properties of both a wave and a particle.

Early experiments were done with candle light, which the great progress of the 19th century and the development of electricity replaced with electric bulbs. At that time scientists were able to manipulate light but they were constrained to work with a very narrow bandwidth of electromagnetic spectrum, visible light. It wasn't up until the very end of the 19th century when a German physicist Wilhelm Röntgen started a systematic study of a particular range of radiation, which he named X-rays.

Both the beauty and danger of X-rays lies in their wavelength, which is of the order of 10^{-10} m. High frequency X-ray photons penetrate most materials and interact with electrons, which allows them to unveil the previously unreachable atomic structures of the study materials. On the other hand, there is a distinct biological hazard originating from the careless use of X-rays and their exposure to biological cells, as they can cause irreversible changes inside the cells' structure.

The development of techniques utilising this kind of radiation depended hugely on the way they were generated. For the first half of the 20th century the main method was through X-ray tubes, which produced radiation beams of sufficient intensity, but were rather unstable. In 1946 a new machine to produce powerful beams of X-rays was announced and launched a year after, which was named a synchrotron. This signified a novel and rapid development for X-ray science, as powerful, stable and intense radiation fluxes were now conveniently available to researchers. At present, there are many synchrotrons in use around the world and more powerful ones are being built, which opens more opportunities for further development of X-ray scattering methods.

1.2 X-ray scattering as a research tool

X-ray scattering is a research method for investigating the structure of materials. It is a versatile technique that provides information about the chemical composition and crystallographic structure of materials. The sketch in fig. 1.1 illustrates the process of scattering from two different samples: scattering from a single crystal results in a diffraction pattern that captures reflections as symmetric dots dissipated in a distinct fashion throughout a sensitive plate, and scattering from a powder sample provides a diffraction pattern of concentric circles.

When a beam of radiation hits the sample the incoming photons interact with its atoms and molecules, change their direction and/or intensity as a result of the collision and finally hit the sensitive plate of the radiation detector. The scattered arrangement of the photons on a sensitive plate, referred to as diffraction pattern, is then analysed. Analysis of this pattern reveals unknown characteristics of the study object, such as its structure, chemical composition and physical properties (for example, its spatial orientation and crystalline phases).

There are two types of scattering: elastic and inelastic. On the general level the difference lies in whether the energy of the scattered photons is conserved or not. The two processes are then described by classical or quantum mechanics.

In elastic scattering X-rays are treated classically, i.e. as waves: the electric field of an incident X-ray wave exerts a force on the charge of a free electron, making it accelerate and therefore radiate a scattered wave. The wavelengths of the scattered and incident X-ray waves are the same in this representation, therefore the energy is conserved, but the direction of the scattered wave is changed. It is the most frequently used process that is exploited in investigations of the structure of materials, and is known as Thomson scattering.

The quantum mechanical description of X-ray photons, which is used in inelastic scattering, implies them to have momentum $\hbar\vec{k}$ and energy $\hbar\omega$. The

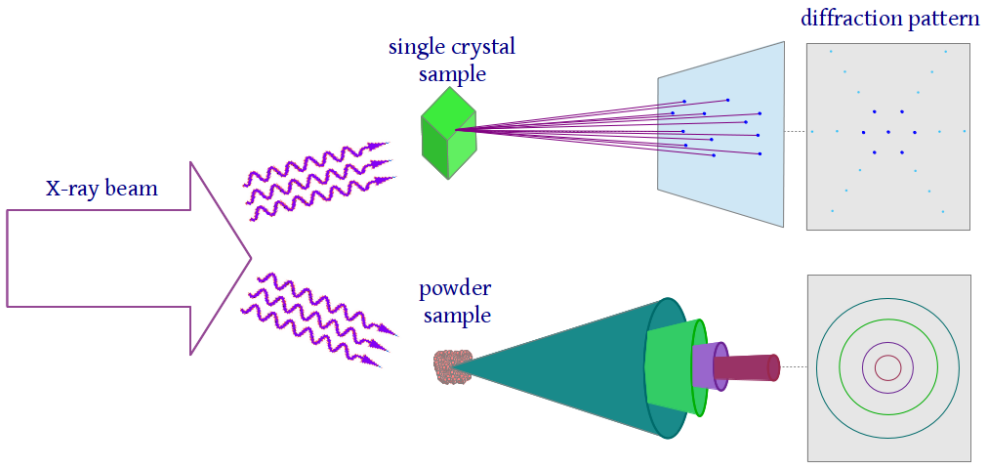

Figure 1.1: Schematic depicting a basic process of scattering.

energy of an incoming photon is not conserved, and the scattered photon carries less energy than the incoming one. The energy difference between the incoming and scattered photons makes the interaction atom elevate to an excited state, which allows investigation of the electronic structures of the sample's molecules. Inelastic scattering is also known as Compton scattering.

X-ray scattering has become a leading technique for structural research. Firstly, application of X-rays allows investigation of atomic structure. Secondly, it is a relatively easy and a fast method (compared to, for instance, neutron scattering). Finally, modern X-ray sources provide experimentalists with powerful beams of high fluxes, which enhances data statistics and leads to deeper analysis and better precision.

A typical X-ray scattering experiment consists of four main units:

- radiation source,
- optical system,
- sample,
- detection system.

All parts are equally important, and they are briefly described in the following section with an emphasis on some peculiarities from the point of view of the X-ray range of radiation.

1.2.1 Sources of X-ray radiation: synchrotrons

In a laboratory environment X-ray beams are usually produced with the help of modern X-ray tubes, the principles of which are explained in detail in chapter 4.1.1. The generation of powerful fluxes of X-ray radiation suitable for experiments of high precision and complexity is done at large facilities called synchrotrons, the fundamental structure of which is illustrated in fig. 1.2.

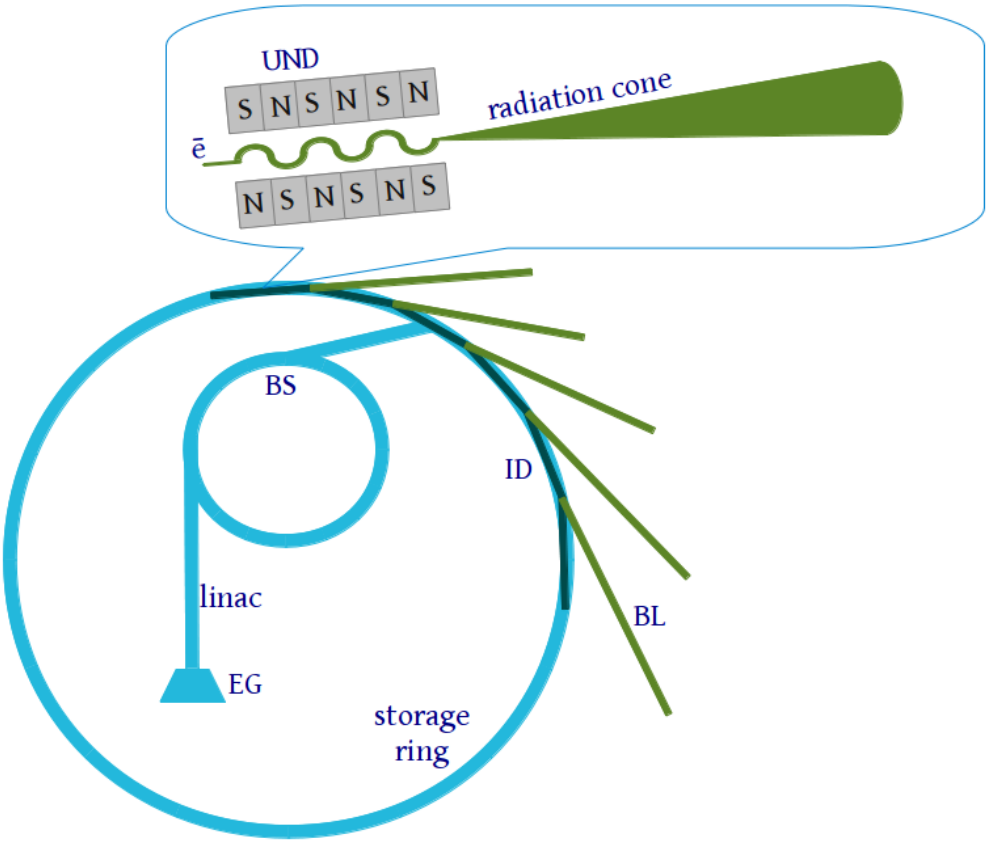

Figure 1.2: Schematic of a synchrotron radiation facility: electron gun EG, linear accelerator linac, booster synchrotron BS, insertion devices ID, beamlines BL. Magnified area: undulator UND and electron bunch ē.

An electron bunch is produced by the electron gun via thermionic emission[1]. A stream of liberated electrons is emitted in pulses into the linear accelerator, which is a hollow pipe vacuum chamber containing electrically isolated cylindrical electrodes. When an electron bunch passes through the linac tube a maximum voltage is applied between the electrodes by the energies of the radio frequencies. This acceleration enhances electrons' energy up to 100-400 MeV[2]. After the linac the electron bunch enters the booster synchrotron, which consists of straight sections and a collection of bending magnets bringing the segments together. As the electron beam passes through the BS, it obtains an ultra relativistic (99.999% of the speed of light) speed and gets a massive boost in energy reaching a maximum electron energy for a particular synchrotron, typically in the range of 2 to 7 GeV. The electrons are finally injected into the storage ring[3]. The construction of the storage ring resembles that of the booster, but on a significantly larger scale: straight line segments are united by bending mag-

[1] A cathode of high voltage is heated in vacuum, giving the electrons of the cathode material sufficient thermal energy to overcome the binding potential and escape from the surface.

[2] Precise numbers depend on particular synchrotrons.

[3] A circumference of a modern third- generation storage ring, like the European Synchrotron Radiation Facility, is about 300 meters.

nets. Insertion devices, which are specific magnetic structures for generation of certain types of X-ray spectra, can be placed inside the straight sections. There are two types of ID widely used in third-generation synchrotrons: wigglers and undulators. Both of these structures are sets of magnets (as shown in the magnified area in fig. 1.2), whose main purpose is to extract X-ray photons from the electron bunch, traversing the cavity. This is done via an alternating magnetic field, which causes the electrons to oscillate and emit photons. The applied fields and magnetic periods are different for wigglers and undulators, resulting in different spectra. The narrow radiation cone illustrated in fig. 1.2 is typical of an undulator, whereas the radiation cone produced by a wiggler is broader. Beamlines are placed at tangents to the storage ring to guide narrow photon beams to experimental stations. Each beamline is optimised for a particular type of experiment, but all beamlines have three main sections: the optics hutch, where the X-ray beam is filtered and focused; the experimental hutch, where the photons interact with the sample; the control cabin, where users control the experiment and collect data.

One of the most important qualities of synchrotron radiation is a beam's intensity, which is defined as the number of photons emitted within a particular energy range per second. The spectral bandwidth is defined as 0.1% of the range of emitted photon energies, referred to as 0.1% BW. The photon flux in this range is normalised to a beam current of 1 A and the time s, yielding to its definition [7]:

$$F = \frac{\text{photons}}{s \cdot 0.1\%\text{BW} \cdot A}. \tag{1.1}$$

The quality of the beam is described by its brightness S, which describes the angular divergence of the beam in the horizontal and vertical directions respectively σ'_x and σ'_y through:

$$S = \frac{F}{2\pi\sigma'_x\sigma'_y}, \tag{1.2}$$
$$S = \frac{\text{photons}}{s \cdot 0.1\%\text{BW} \cdot \text{mrad}^2 \cdot A}.$$

The most important property of the beam is its brilliance B, which is defined through brightness as:

$$B = \frac{S}{2\sigma_x\sigma_z}, \tag{1.3}$$
$$B = \frac{\text{photons}}{s \cdot 0.1\%\text{BW} \cdot \text{mm}^2 \cdot \text{mrad}^2 \cdot A},$$

where σ_x and σ_z are the beams' dimensions in the respective directions.

1.2.2 Optical system: beamline optics

A first optical element of a beamline is always a monochromator, which could be placed either at the end of an insertion device section (which limits any access to it), or in the beginning of a beamline. Typically it is either a set of

silicon crystals or a set of slits. The system allows only a single wavelength from the whole spectrum to pass through. Optical elements that are mounted in the beamline serve to manipulate the beam's propagation, i.e. to deliver the photon beam to a sample being studied without any losses of the flux. It is often necessary to focus the photon beam to a spot of micro- or sometimes even nanometer size, therefore various types of focusing devices are present in the beamline, such as X-ray lenses and zone plates. Zone plates provide superior transmission and stronger focusing, but are much more expensive than X-ray lenses.

Development and production of X-ray optics progressed slowly up until the beginning of the 90's, as such physical phenomena as refraction, absorption and reflection considered for the X-ray region implied certain constraints for available materials. The index of refraction for those materials that display resonant behaviour of radiation frequencies corresponding to electronic transitions in atoms and molecules is less than unity for the X-ray range of frequencies[4]. The relationship between the refractive index of a material and its scattering properties is:

$$n = 1 - \delta + i\beta, \tag{1.4}$$

where δ is a refractive index decrement relating the scattering properties of the medium, such as electron density ρ, scattering amplitude per electron r_0 and the wave vector k; and β is an attenuation coefficient of the medium connecting its absorption coefficient μ with wave vector k:

$$\delta = \frac{2\pi\rho r_0}{k^2}, \tag{1.5}$$

$$\beta = \frac{\mu}{2k}. \tag{1.6}$$

δ is usually of the order of 10^{-6} and β tends to be about two orders of magnitude smaller, therefore the refractive index is very close to unity, which makes it very difficult to focus such a beam, as it refracts almost negligibly. The focal length of a single X-ray lens with a parabolic profile is $f = R/2\delta$, where R is the radius at the tip of the parabola; usually R is of the order of half a mm. The focal length of a single lens is typically of the order of a hundred metres, which is too long to be of practical use in beamlines. A number of such lenses stacked together reduce the focal length considerably according to:

$$f = \frac{R}{2N\delta}. \tag{1.7}$$

In order to focus a beam of X-ray photons with a lens whose refractive index is smaller than unity, its interface should have a concave shape (as opposed to focusing lenses for visible light, whose surfaces is convex). A lens's material is chosen according to its absorption properties, i.e. it should have a small atomic

[4]The X-ray frequencies are higher than most frequencies of the electronic transitions in atoms, which means that an incident photon gets a phase shift of π at a material's interface that influences the refraction index; without a phase shift a refractive index is larger than unity.

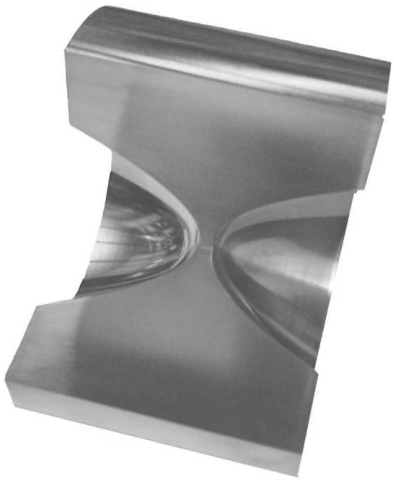

Figure 1.3: Model of an aluminium refractive X-ray lens with a double parabolic profile taken from [8].

number Z (as a beam's transmission is inversely proportional to Z^4). For this reason the most commonly used materials for X-ray lenses are lithium (Z=3), beryllium (Z=4), aluminium (Z=13) and silicon (Z=14).

Another interesting aspect of manipulating X-ray beams with mirrors is connected with their reflectivity, particularly the phenomenon of total external reflection. For incident angles below a certain critical angle α_c the rays will no longer penetrate into the material, but will be totally reflected from it. This means that the material does not absorb any radiation, which completely eliminates absorption losses in the mirror. The critical angle depends on the refractive index decrement δ according to eq. 1.8, and typically has a value of the order of several mrad:

$$\alpha_c = \sqrt{2\delta} = \frac{\sqrt{4\pi\rho r_0}}{k}. \tag{1.8}$$

Operation at such small glancing angles is not performed, as the incident beam's footprint would be so long that the mirror required would be too large. To overcome this difficulty and to maintain the benefits from operation at small glancing angles, the mirror is covered with several layers of specially designed highly reflective coatings. This type of mirrors is referred to as a multilayer mirror. The application of multilayer mirrors has increased in recent years, which is connected with new technologies for depositing thin layers of reflective coatings. The physical principle of a multilayer mirror is the same as the one describing operation of diffraction gratings for visible light.

By using compound refractive lenses and multilayer mirrors X-ray beams are delivered from the end of an insertion device section throughout various beamlines without significant losses and are focused at sample planes.

1.2.3 Sample: principles of X-ray diffraction

The main ideas of the theory of X-ray diffraction are underlined in the current section, emphasising the logic behind this experimental technique. A full theory of X-ray diffraction is given in [9] and [10].

After passing through all optical elements of a beamline, the X-ray beam is collimated and ready to interact with a sample. The illustration in fig. 1.4 shows the principle of this process, where the incoming X-ray beam I_{inc} gets transformed into I_{out} after the interaction with the crystal lattice of a sample. The resulting diffraction pattern carries information regarding the structural arrangements of the lattice, hence its correct interpretation is the main focus of the method.

An incident photon can be described by a wave vector $\vec{k_{\text{inc}}}$. Its interaction with a sample gives rise to a new photon, whose vector is $\vec{k_{\text{out}}}$. The difference of these two vectors is a scattering vector, or wave vector transfer $\vec{Q}$, whose magnitude is defined as $|\vec{Q}| = 2|\vec{k}|\sin\theta$, where θ is half of the scattering angle.

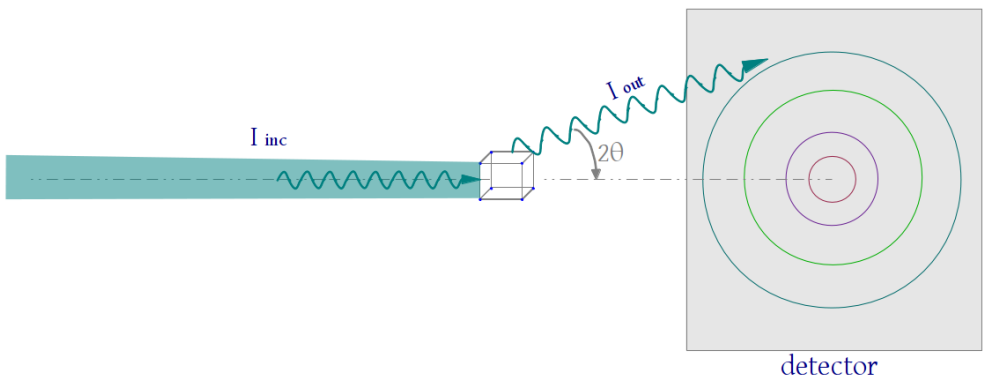

Figure 1.4: Schematic of a very simple case of Bragg scattering.

A sample is characterised by a crystal lattice - a regular three-dimensional distribution of atoms in space, which are arranged in such a fashion so they form a series of parallel planes (marked in pale red in fig. 1.5) separated from one another by a distance d. The building blocks of the crystal lattice are called unit cells; the atoms of one such cell are depicted in green in fig. 1.5. The distribution of electrons within one unit cell, or electron density $\rho(\vec{r})$, is called a basis, and it completes the description of the structure of a unit cell. The vectors $\vec{a_1}$, $\vec{a_2}$ and $\vec{a_3}$ define a unit cell, whilst a lattice is specified by a set of vectors: $\vec{R_n} = n_1\vec{a_1} + n_2\vec{a_2} + n_3\vec{a_3}$, where n_1, n_2 and n_3 are integers.
It is assumed that the amplitude of the scattered wave after interaction with a volume of the sample's unit cell is proportional to the electron density $\rho(\vec{r})$ of the unit cell. The total amplitude of the scattered wave is then proportional to the integral over the entire crystal of $\rho(\vec{r})\mathrm{d}\vec{r}$ multiplied by the phase factor, $e^{i\vec{Q}\cdot\vec{r}}$, according to:

$$A(\vec{Q}) \propto \int_{\text{crystal}} \rho(\vec{r}) e^{i\vec{Q}\cdot\vec{r}} \mathrm{d}\vec{r}. \tag{1.9}$$

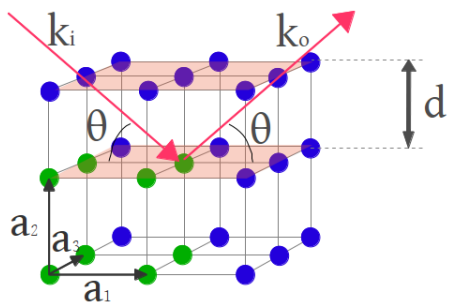

Figure 1.5: Illustration of a sample structure and its interaction with an incoming photon. A cubic lattice of a crystalline material with its basic unit cell defined through a set of vectors $\vec{a_1}$, $\vec{a_2}$ and $\vec{a_3}$ marked in green; diffraction planes are filled with a pale red colour and separated by a space labeled d; incident and reflected photons k_i and k_o, respectively, form equal angles θ with diffraction planes.

In other words, an extension of eq. 1.9 yields eq. 1.10 with two main constituents: a lattice sum and a unit cell structure factor presented respectively:

$$A(\vec{Q}) \propto \sum_n e^{i\vec{Q}\cdot\vec{R_n}} \sum_{u.c.} f_j(\vec{Q}) e^{i\vec{Q}\cdot\vec{r}}. \tag{1.10}$$

The total scattered intensity is then the multiplication product of the amplitude with its conjugate:

$$I_{sc} = A(\vec{Q}) \cdot A(\vec{Q})^*. \tag{1.11}$$

The first term in eq. 1.10, the lattice sum, is large only under the condition of observing diffraction maxima, referred to as the Laue condition[5]. A mathematical derivation of this condition requires the introduction of crystallographic parameters beyond the scope of the current discussion. In practice, the Laue condition is confirmed through the Bragg law (only when the radiation wavelength and d-spacings are comparable, i.e. $\lambda \leqslant 2d$), which states that when a monochromatic beam with a wavelength λ is projected onto a crystalline material at an angle θ (fig. 1.5), diffraction occurs only when the distance travelled by the rays and reflected from successive planes differs by an integer number of wavelengths n:

$$n\lambda = 2d \sin\theta. \tag{1.12}$$

The diffraction angle θ is varied throughout the experiment, therefore different conditions are satisfied according to the Bragg law, which brings multiple reflections from various planes with different d-spacings of the sample crystal. The second term in eq. 1.10 shows the arrangement of electrons in the unit cell,

[5]The number of terms in the lattice sum is enormous. Each of the terms is a complex number, $e^{i\phi_n}$. The sum of phase factors is of order unity, except when all phases are 2π or its multiple, in which case the sum will be equal to a huge number of terms. In order to resolve it, an additional reciprocal lattice is built. Therefore, the Laue condition requires the set of reciprocal lattice vectors $\vec{G}$, to coincide with $\vec{Q}$, $\vec{G} = \vec{Q}$.

i.e. how the electrons are distributed in the atoms and molecules within the sample crystal. In fact, it is the primary goal of the X-ray diffraction technique.

The total scattered intensity of the beam I_{sc} is obtained from an experimentally measured differential cross-section of the beam $d\sigma/d\Omega$:

$$I_{sc} = I_0 N \Delta\Omega \frac{d\sigma}{d\Omega}, \tag{1.13}$$

where I_0 is the beam's initial intensity, N is the number of particles in the unit cell and $\Delta\Omega$ is the solid angle subtended by the detector.

However, the conversion of a diffraction pattern immediately into the sample's structure is not straightforward, as the measured intensity depends on the squared amplitude $|A|^2$, and phase information is not readily available from it. Therefore more techniques are needed to decompose the measured data.

1.2.4 Detection system: X-rays detectors

Constant engineering development over the last few years have resulted in a variety of types of X-ray detectors. A good overview of currently available detectors is given in [11]. Usually, detection systems contain two parts: an X-ray sensitive detector block itself and an analyser block including electronics that transform the incoming radiation into electric pulses. Depending on what exactly needs to be determined, there are a few categories:

- Semiconductor detectors. In one mode they measure and resolve energy of single photons (commonly used for soft X-rays up to 6 keV); in another mode they're able to measure the whole flux;

- CCD detectors. Typically a phosphor screen is used to convert incident X-rays into optical photons, which further are detected by a CCD censor; these detectors are primarily used for imaging purposes;

- Scintillator counters;

The detection principles of CCD and semiconductor detectors are going to be described in chapter 4.1.3, whilst an overview of a scintillator follows here.

Scintillation detectors measure both energy and intensity of X-rays. An incoming X-ray photon is absorbed by a crystal, which is typically NaI doped with Tl. It excites the atoms of the crystal, causing the production of a visible light photon with intensity proportional to the energy of the X-ray. The newly appeared light photon is then directed towards a photo-cathode and liberates an electron via the photoelectric effect. The electron is accelerated and multiplied in a cascade in a photomultiplier. The output signal at the anode is amplified, analysed by the processing electronics unit and is displayed as a pulse. A collection of such pulses with different heights is then presented as a 2D spectrum with X-ray energy on one axis and intensity on the other. Scintillation counters are commonly used in laboratories for many applications requiring high count rate and only moderate energy resolution.

A few general parameters define detectors' qualities. First of all, the detector's energy resolution is a pivotal attribute describing its quality: the smaller the better. When a photon of a particular energy E is registered by a detector, the resulting signal is transformed into an electric pulse with voltage proportional to the incoming energy. The ratio of the full width at half-maximum of this pulse (FWHM) to the primary energy of the photon, $\Delta E/E$, is then the energy resolution.

Secondly, a signal-to-noise ratio (STN). The noise is the activity in the detector in the absence of a genuine signal. The concept of signal-to-noise ratio is used to describe the proportion between the signal amplitude and the size of the noise, both of which should be measured in the same units.

Thirdly, the detective quantum efficiency (DQE), which is a measure of how a detector affects the incoming STN ratio. Ideally, a detector should produce an output signal with the same STN ration as the incoming signal. In reality, however, a detector does increase the incoming STN, as other aspects of the system's performance influence the result:

$$\mathrm{DQE} = \left(\frac{\mathrm{STN_{out}}}{\mathrm{STN_{in}}}\right)^2 . \tag{1.14}$$

Modern detectors have high DQE (starting from 90% and higher).

Chapter 2

The new ray-tracing programme McXtrace

The chapter presents a new software for X-ray scattering instrumentation McXtrace. The history of the code is traced back towards the appearance of its sister package for neutron simulations, McStas. Both packages are based on the Monte Carlo simulation strategy, the principles of which are outlined in the chapter. The McXtrace code structure and functionality are introduced followed by a discussion of its advantages and limitations.

2.1 Historical background

In the world of neutron scattering in the last decades of the 20th century there were only two simulation packages: the pioneering neutron transport code MCNP [12] and a package for scattering purposes NISP [13] (developed in Los Alamos National Laboratory, USA). The codes were able to perform all types of calculations, however it took tremendous amount of time, as they were initially created for simulations of nuclear plants.

In the late years of the past century at Risø National Laboratory, there appeared a particular necessity for an efficient neutron simulation tool, as the existing instrument RITA-1 needed optimisation, and a plan for a new instrument RITA-2 was conceived[1]. New instruments for new sources were conceptualised, but there was a lack of modelling software that could simulate a whole instrument's performance at once. The available packages could only provide calculations of independent parts of an instrument as they were not monolithic, so each new simulation required a separate code, which expended the time of obtaining results, as extra time for debugging was essential.

A concept of virtual experiments was first proposed to become a preferred direction at that time: an entire neutron experiment could be simulated at once. An established term for virtual experiments encompasses the following criteria [14]:

[1] Ultimately, the implementation of the RITA-2 instrument, however, was done at the Paul Scherrer Institut in Villigen, Switzerland, as the nuclear reactor at Risø was terminated in the beginning of 2000.

- The X-ray photons must have absolute intensity units and should be traced through the whole instrument, from source to detector. This can be done either by simulating each photon through the instrument or by breaking the simulation up into several bits.
- The description of the instrument should be as close as possible to reality. This is in particular the case for the sample.
- The virtual instrument is controlled like the real instrument, and the resulting data are analysed like the real data.

The concept provided a whole spectrum of benefits valuable to instrument builders as well as in training users. The decision was made about developing such a functional tool at Risø by Kim Lefmann and Kristian Nielsen. That is how the first version of McStas [15], an abbreviation for Monte Carlo simulation of triple-axis spectrometer, was released in October 1998.

It has to be mentioned that the field of neutron ray-tracing simulation for scattering purposes has significantly expanded in the last decade of the 20th century. Aside from McStas, several other open source simulation packages were initialised, namely Vitess [16] (a German in-kind contribution to the European Spallation Source) , ResTrax [17] (a code developed in Czech Republic) and Ideas [18] (created in the Oak Ridge National Laboratory, USA). At present, the concurrent and independent development of these programmes occurs in the atmosphere of friendly competition, therefore the knowledge transfer between the packages serves the common benefit.

McStas turned out to be a fast and versatile software tool for neutron ray-tracing simulations. It is based on a meta-language specially designed for neutron simulation. Specifications are written in this language by users and automatically translated into efficient simulation codes in C. The package is actively being developed and supported by the Danish Technical University Risø, the Institut Laue Langevin in France, the Paul Scherrer Institut in Switzerland and the University of Copenhagen.

Over the last fourteen years since its launch the code has gain enormous popularity among the neutron community - the software is used all over the world. The points making the package so widely appreciated lie in the user-friendliness (the interface is self-explanatory), modularity (as each component of an instrument is a separate module, it is easily accessible and changeable when necessary), swiftness (a simulation of a typical instrument of an average level of difficulty requires a few hours), accuracy (simulations predictions lie within 5-10% of real data) and availability (it is an open source code freely available on its web page [19]).

In the end of the 90's the simulations of X-ray scattering instruments and experiments was supported by several packages: Shadow, Ray [6] and SRW. The SRW code is based on the methods of physical optics, whilst Ray and Shadow utilise ray-tracing. Shadow was the most commonly used package among the X-ray scientists. However, it was initially built in Fortran and had a limited number of simulated rays, which imposed certain difficulties and restricted the statistical accuracy. Therefore there was a necessity of a modern simulation

tool, which, like in the neutron world, would develop concurrently and independently yet sharing the common principles of ray-tracing.

The processes of X-ray and neutron scattering are strikingly similar, therefore an agreement between the ESRF and DTU Risø was made to merge the two world leading packages, Shadow and McStas, in order to develop a novel tool. That was the initiation of the McXtrace simulation software. The previously obtained wide experience of McStas in solving similar types of problems would greatly enhance the development of McXtrace. The main objectives of the new project was to provide the X-ray community with a state-of-the-art ray-tracing tool, which would be easy in usage, fast, reliable and freely available.

2.2 Monte Carlo ray-tracing simulation technique

The method is named after the world's most famous casino, as its gambling style is serious and sophisticated as opposed to the glamourous and frivolous casinos of Vegas. Certainly, there is an obvious contradiction between the unpredictability of the gambling process and the seriousness of the results - a distinct aspect of the Monte Carlo method.

Generally speaking, Monte Carlo integration is a method to approximate integrals with random numbers, especially when analytical solutions are impossible. A more enlightening definition is given by Halton [20]: "the Monte Carlo (MC) method is defined as representing the solution of a problem as a parameter of a hypothetical population, and using a random sequence of numbers to construct a sample of the population, from which statistical estimates of parameters can be obtained".

The method is widely used in multiple areas. For instance, in particle physics (simulation of high energy particles collisions), in mathematics (solving complex integrals in multiple dimensions), in finance (estimation of different market uncertainties and risk assessments), and in computer science (optimisation of multi-variable functions).

2.2.1 Mathematical foundation for the Monte Carlo integration

A few important definitions are introduced, which are essential for the explanation of MC integration.

Suppose, there is a random variable x that can take on any value in the interval $(-\infty, +\infty)$. Probability density function $p(x)$, PDF, is a function, which defines the distribution of values associated with x [21]. The probability that x will taken on a value in some arbitrary interval $[a, b]$ is given by the integral:

$$P = \int_a^b p(x)\mathrm{d}x, \tag{2.1}$$

which basically shows the relative likelihood of a random variable taking on a certain value.

The mathematical expectation (or expected value) E of a function $f(x)$ is defined as the average value of this function:

$$E(f(x)) = \int f(x)p(x)\mathrm{d}x. \tag{2.2}$$

The expectation has an important property, which is crucial for most applications of the method: the expected value of the sum of two random variables is the sum of the expected values of those variables:

$$E(f(x) + g(y)) = E(f(x)) + E(g(y)). \tag{2.3}$$

The variance of a function or variable $V(x)$ is the average of the squared difference between a function (variable) and its expectation (this definition is used for the derivation of error estimates in eq. 2.14):

$$V(x) = E([x - E(x)]^2). \tag{2.4}$$

When dealing with large numbers, the law of large numbers is concerned, which governs the sums of large numbers of random variables. For example, suppose there is an N numbers of x_i chosen randomly with a uniform PDF on an interval $[a, b]$. The function $f(x_i)$ is evaluated for each x_i. The law postulates that the sum of this function values divided by N will converge to the expectation of f:

$$\frac{1}{N}\sum_{i=1}^{N} f(x_i) \to \frac{1}{b-a}\int_a^b f(x)\mathrm{d}x. \tag{2.5}$$

The left side of ex. 2.5 shows the MC estimate of the integral on the right. Therefore the law is interpreted in the following fashion: the MC estimate of an integral is consistent, i.e. it converges to the correct answer, as the random sample size becomes large.

The MC integration applied to a function of a random variable $f(x)$ with a defined PDF $p(x)$ yields the expected value to be approximated by a sum:

$$E(f(x)) = \int f(x)p(x)\mathrm{d}x \approx \frac{1}{N}\sum_{i=1}^{N} f(x_i). \tag{2.6}$$

It is more convenient to apply the approximation to a single function $f(x)$ rather than to the multiplication product $f(x)p(x)$, that is why a substitution is used:

$$g(x) = f(x) \cdot p(x) \Rightarrow \int g(x)\mathrm{d}x \approx \frac{1}{N}\sum_{i=1}^{N} \frac{g(x_i)}{p(x_i)}. \tag{2.7}$$

The substitution is only applicable under certain conditions: $p(x)$ must be positive and $g(x)$ must be nonzero.

2.2.2 Ray-tracing strategies

The method of tracing rays was first mentioned in the 60's, and it is described in detail in [22]. It relies on the laws of geometrical optics, which assumes light to travel along straight lines. Phenomena accounting for the wave-nature properties of radiation and governing interference and diffraction are not considered in the basic principles of ray-tracing. However, a few successful attempts have been explored to expand the method, but yet they are not fully integrated.

This approach is widely used in computer graphics to solve tasks of realistic illumination of 3D objects. In science ray-tracing is widespread for studying

non-interacting radiation, i.e. neutrons and X-rays, and for high energy particles.

The concept of the method is illustrated in fig. 2.1. Suppose, a radiation photon is emitted from a point S_0, located on a surface of an area A_0. The direction of the photon takes it further to intersect another surface at a point S_1, which area is A_1. The resulting new direction of the photon brings it to the last surface A_2 to a point S_2.

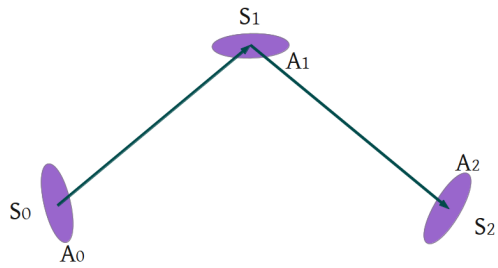

Figure 2.1: The concept of ray-tracing.

Each photon is characterised by a number of parameters: its position in space, energy, direction and phase[2]. It is convenient to specify the state of each surface with its radiance[3] L_0, L_1 and L_2, which is proportional to the photon's parameters. The interacting surfaces are characterised by their own PDFs, i.e. p_0 and p_1. An important assumption is used in ray-tracing: in free space the radiance does not change along the path of a photon in the absence of scattering or absorption. To account for the cumulative effects of scattering and absorption at each surface, coefficients T_0 and T_1 are introduced. The radiance of the last surface is then characterised by the contributions from the previous surfaces:

$$L_2 = L_0 + L_1, \tag{2.8}$$

$$L_2 = \int_{A_0} p_0 \cdot L_0 \cdot T_0 \int_{A_1} p_1 \cdot L_1 \cdot T_1 \mathrm{d}A_0 \mathrm{d}A_1. \tag{2.9}$$

The integrals represent a combination of photons' paths. Each path is characterised by a set of vertices: the first one is a point on the surface of the light source S_0, the subsequent vertex is the point on the reflecting surface S_1 and the final vertex is the point on the receiving surface S_2. The total contribution of all paths is obtained by integrating over all possible light and surface positions. The solution of these integrals is approximated by the MC method:

$$L_2 = \sum_{i=0}^{\infty} K^i \circ L_0, \tag{2.10}$$

where K is an operator of mapping one function to another.

[2]The specification of the mentioned parameters is currently omitted.

[3]Radiance is quite often confused with intensity. The original definition of radiance is conserved for the explanation of the concept. In simulations, however, a term *weight* is used.

2.2.3 Application of the simulation strategy to X-rays

Weight.
To run a simulation of any beamline model and to get some valuable results from it, one needs to generate a large number of events, which in McXtrace language is equivalent to a number of photon rays. To save computational resources, each photon ray is given a weight factor p, the core meaning of which is just a statistical representation of a particular photon ray in the beam.

The weight of a photon ray is adjusted according to its trajectory through the modelled instrument. For instance, if the photon is passing through a component, whose reflectivity is only 36%, the initial weight is multiplied by 0.36. The weight multiplication factor in the j'th component is denoted by π_j. The final weight of the photon ray after it's travelled through an entire instrument reads

$$p(x) = p_n(x) = p_0(x) \prod_{j=1}^{n} \pi_j. \tag{2.11}$$

It is rather logical, that the weight can rarely exceed 1. In fact, it is most often decreasing towards the end of the instrument.

Directional sampling.
Another way to overcome unnecessary computational resource is to carefully consider the direction, in which to sample the photon rays. Instead of integrating over an entire hemisphere from the photons' emission point on a source, it is considered that a ray is emitted only into a solid angle Ω subtended by an arbitrary aperture, as seen from the source. The weight factor $p_i(x)$ is then adjusted according to:

$$p_i(x) = \frac{\Omega}{4\pi} p_0(x). \tag{2.12}$$

Error estimates. In a usual beamline experiment, intensity is measured as a number of detected photons per exposure time (the value is taken from a detector). In simulations, a beam's intensity corresponds to a product of the weights of photon rays hitting the detector $p(x)$ and their number N:

$$I = \sum_{j=1}^{N} p_j(x) = N\bar{p}(x). \tag{2.13}$$

To estimate the errors, the central limit theorem for stochastic variables [23] is applied. It postulates that a sum of a set of independent stochastic variables of any distribution is approximately normally distributed. Suppose that $p_i(x)$ is an observation of a stochastic variable $P_i(x)$, then the variance of the sum

defined previously in eq. 2.4 is estimated according to:

$$\sigma(p(x))^2 = \frac{1}{N-1}\sum_{j=1}^{N}(p_j(x) - \bar{p}(x))^2$$
$$\approx \frac{1}{N}\sum_{j=1}^{N} p_j(x)^2 - \frac{1}{N^2}\left(\sum_{j=1}^{N} p_j(x)\right)^2 . \tag{2.14}$$

2.3 The structure of the McXtrace code

Since McXtrace is closely interlinked with McStas, the core of the software is almost identical to that in the latter programme, as the foundation of modelling neutron and X-ray scattering is the same. Hence, McXtrace is based on its own meta-language, originally designed for simulations of beamlines. Therefore to perform a simulation project a beamline should be specified in the meta-language. The McXtrace compiler then translates it into a monolithic C-code, which is run by the software. The simulation results are typically stored in data files, which could be immediately visualised. There are a few options regarding the visual display of the result: it could be shown either inside the software using a built-in Pgplot, it could be transferred to Matlab and Scilab or it could be visualised in Gnuplot.

The design of the software consists of three conceptual layers:

- The physical processes of photons' interaction with matter (scattering, absorption or reflection) are described in a *component* layer;
- Gathering all components comprising a modelled beamline, defining its geometry and sequence is realised in an *instrument* layer;
- Execution of simulations, i.e. calculation of the fate of photons through the Monte Carlo techniques is performed in the *kernel* layer.

The layers have different levels of complexity: for instance, at the component level there is only a mathematical description of the physics, which effectively doesn't require long and computationally heavy algorithms, yet the knowledge of physics is essential; proficiency at the instrument level depends primarily on the fluency in the meta-language, whilst all computationally demanding algorithms are inside the kernel level. However, the experience gained with a similar kernel of McStas yielded to smooth operation and swift processes at the kernel level, which are, in fact, invisible to a great extend for users.

2.3.1 Component level

In the current version of the code, there are all necessary components to simulate most modern beamlines. All components are divided into categories for convenience: source, optics, samples and monitors. Each component is independent, it has its local coordinate system and generally has its own micro-realm for photons.

The following parameters define an X-ray photon throughout a simulation: position $\vec{r}$ (in Cartesian coordinates x, y and z), wave vector $\vec{k}$ (or rather its projections on the axes, i.e. k_x, k_y and k_z), phase ϕ, polarisation $\vec{E}$ (E_x, E_y and E_z) and weight p.

The component frequently used for the simulation projects presented in the present dissertation (chapters 5 and 6) *Lens_parab_Cyl* is illustrated to explain the concept. A single lens with two interfaces of parabolic cylinders is targeted to focus an X-ray beam in one direction [24]. Geometrical description of the lens is defined through a number of settings: radius of curvature at the tip of parabola R, geometrical apertures along the appropriate directions h_y and h_x, distance between the apices of the interfaces d (fig. 2.2). The algorithm implemented in the component allows to extend a single lens to a compound one, if necessary, by defining a number of lenses N. All the properties of the material of the lens (various X-ray constants) are taken from the software database, which is based on the NIST data, therefore a mere specification of the material suffices.

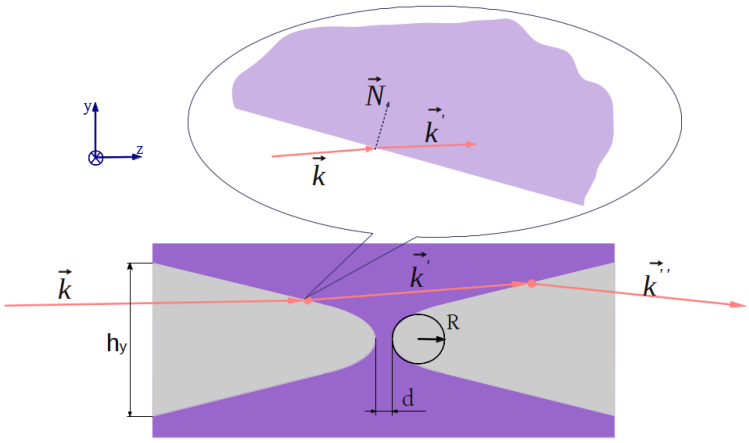

Figure 2.2: Sketch underlying the physics of a photon's interaction with *Lens_parab_Cyl* component with a parabolic cylinder profile: an incoming photon $\vec{k}$ is transformed into $\vec{k}''$.

The algorithm of the photon's transformation upon its interaction with the lens presented in the code is very simple. A photon $\vec{k}$ is incident on the surface of the lens at a particular angle. The determination of the photon's intersection point is given a small uncertainty, which reflects the roughness characteristic of the material[4]. The calculation of the incidence angle (by using an auxiliary normal vector $\vec{N}$ built at the intersection point) and the implementation of the Snell's law [9] triggers the definition of the transformed photon $\vec{k}'$. The new photon carries on traversing the material of the lens until it reaches the second interface. The exact same method is used to determine a new direction of the outgoing photon $\vec{k}''$. The influence of the material on the photon, i.e.

[4]Such a feature allows the code to more closely approximate reality.

transmission T, is calculated according to [8]:

$$T = \exp(-\mu N d)\frac{1}{2a_p}[1 - \exp(-2a_p)], \tag{2.15}$$

where μ is the absorption coefficient and a_p is the absorption aperture, different to the geometrical one and defined as:

$$a_p = \frac{\mu}{\rho}\frac{R_0^2 \cdot N \cdot \delta \cdot k^2}{R \cdot \pi}\frac{A}{N_a \cdot r_e \cdot (Z + f)} \tag{2.16}$$

with mass-absorption coefficient μ/ρ, half of the geometrical aperture R_0: $2R_0 = h_y$, refractive index decrement δ, Avogadro's constant N_a, classical electron radius r_e, atomic mass A and the atomic form factor with a dispersion correction $Z + f$.

The weight of the photon is adjusted according to the transmission factor. The component is finalised with a few lines of code defining the geometrical structure of the lens[5], so it is correctly visualised upon simulations (particularly in the ray-tracing mode of the software's operation).

2.3.2 Instrument level

A collection of components sequentially placed determining a simulated beamline represents an instrument[6]. To set up an instrument for simulations, a user has to know the meta-language, as it is conventionally used to orient components relative to each other and to the origin. It is rather straightforward and very intuitive, therefore doesn't require a lot of effort. It is also possible to include additional lines of C-code to extend the functionality of existing components. For instance, sometimes it could be useful to display and store particular photons' parameters or positions during simulation.

An example of a typical instrument is illustrated in fig. 2.3: the origin of the beamline most often coincides with the source and the remaining components are positioned and/or rotated either relative to the preceding components or with respect to the origin.

2.3.3 Kernel level

The Monte Carlo calculations are executed at the kernel level: the routines are invoked with every run of the compiled code. The task of the kernel is to always keep track of each photon travelling through an instrument during a simulation: its position, direction, energy, phase and weight.

The meta-language is described at the kernel level. For maximum flexibility and portability, it is based on C. Originally it was custom designed for simulations of neutron scattering, then it was modified for X-rays. At present it gets updated when necessary. For instance, the photons are transported from one point to another at a distance dl by a routine **PROP_dl**, which automatically updates the photon's coordinates in accordance with its new position.

[5] Or any other component for that matter.

[6] The term *instrument* is preserved in McXtrace from McStas, since in the neutron world the beamlines are referred to as instruments.

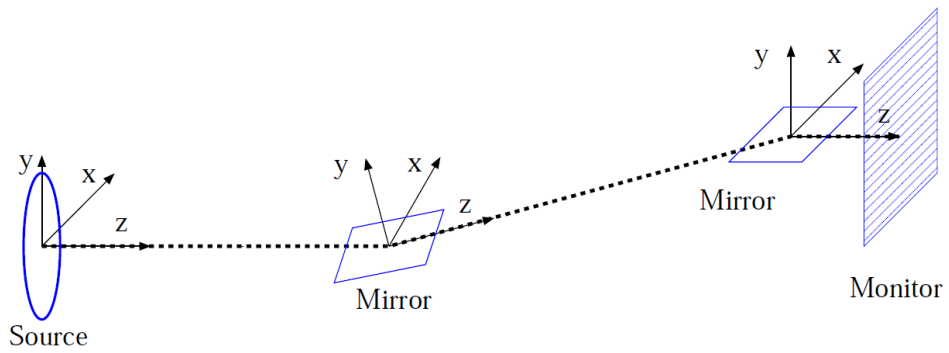

Figure 2.3: Sketch of the McXtrace positioning mechanism, courtesy of E. Knudsen [25].

A number of library functions are also included in the kernel: intersection calculations (a photon's trajectory intersecting various surfaces), random numbers generators, reading or writing from/to data files and unit conversion.

2.4 Advantages and limitations

It is important to evaluate the software firstly according to its own success criteria and secondly relatively other programmes of the same sort.

At its inception the McXtrace project was targeting to fulfill the following three objectives:

- Correctness. The design of the system is as simple as it can get with a single purpose of minimising the appearance of bugs influencing the simulation results. However, bugs are ubiquitous in programming, therefore a simple design allows to identify and correct the faults.
- Flexibility. The modular structure of the code is necessary in order to simulate different kinds of beamlines, when new components are developed to reflect the needs of instrument builders.
- Power. The speed at which an instrument simulation is executed is certainly a powerful criterion: the sooner the better.

However, the development of new X-ray sources and lasers requires a more thorough representation of X-rays with accord to their wave-nature. Hence, such properties like partial and full coherence and polarisation are becoming of primary importance. These phenomena are not yet mastered by the McXtrace package, although a few successful tests have been made already [26].

Chapter 3

Calculation of synchrotron radiation

The chapter describes a strategy for modelling synchrotron radiation presented in the Synchrotron Radiation Workshop (SRW) programme. It was developed in late 90's at the ESRF by Oleg Chubar and Pascal Elleaume as a separate library for a mathematical package IgorPro. The core of the software is written in C++, whilst the part related to the interface is implemented in the IgorPro own meta language. The copyright of the code currently belongs to the Brookhaven National Laboratory.

The SRW code consists of two parts. The first one is calculation of initial wavefront of synchrotron radiation, the second one is propagation of this wavefront along an instrument or a beamline of interest. Thus, firstly, the chapter introduces a vast subject of synchrotron radiation (as initially the programme was originated only for quantifying this aspect): its generation by different types of magnetic structures (bending magnets, wigglers and undulators). Secondly, the chapter describes theoretical concepts underlying the radiation calculation in SRW. The wavefronts propagation method used in the second part of the code is discussed, and a computational example is presented. Finally, the code is considered from a user's perspective, emphasising its advantages and drawbacks.

3.1 Generation of synchrotron radiation

According to the laws of electrodynamics, any charged particle undergoing acceleration will radiate energy in the form of electromagnetic waves. An electron will therefore emit radiation of a specific frequency proportional to the speed at which it is travelling. When the electron speed is close to the speed of light, the emitted radiation is in the X-ray range.

At a modern third-generation synchrotron facility there are three ways of obtaining X-rays from ultra relativistic electrons - through bending magnets, wigglers and undulators. Bending magnets connect the straight segments of storage rings, where wigglers and undulators could be inserted. The three magnetic structures produce different kinds of X-ray beams, whose characteristics are explained in the following sections.

3.1.1 Bending magnets

Bending magnets connect the straight sections of a storage ring, therefore when a relativistic electron reaches it, the vertical magnetic field applied by the magnets makes the electron turn and emit a wavefront of radiation. Description of this radiation is unfolded from the electrons' motion equation. Fig. 3.1 illustrates an arbitrary electron at an instantaneous position along a circular path, at which it has just emitted a radiation wavefront. The wavefront is explored from an observation point located at a distance D from the electron and set by $\vec{r}$ from the centre of the electron's trajectory O. $\vec{R}(\tau)$ is setting the electron's position and time according to the centre of the system, whereas t is the time, at which the wavefront arrives to the observation point.

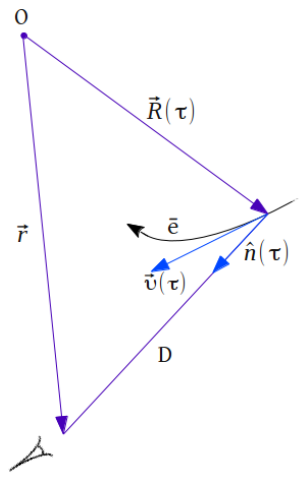

Figure 3.1: Observation of a radiation wavefront emitted by an arbitrary relativistic electron.

As the radiated field propagates with the speed of light, the time τ of the wavefront's emission (also known as retarded time) and the time t of receiving the radiation at the observation point are related via:

$$t = \tau - \frac{D(\tau)}{c}, \tag{3.1}$$

where D is the distance between the electron's position and the observation point at the time τ. D is expressed through the two vectors: $D(\tau) = |\vec{r} - \vec{R}(\tau)|$. After differentiating eq. 3.1 with respect to the retarded time τ, the general relation between the two times is obtained:

$$\frac{\mathrm{d}t}{\mathrm{d}\tau} = 1 - \hat{n}(\tau)\vec{\vartheta}(\tau), \tag{3.2}$$

where $\hat{n}(\tau)$ is a unit vector at the electron's position oriented towards the observation point $\hat{n}(\tau) = (\vec{r} - \vec{R}(\tau))/(|\vec{r} - \vec{R}(\tau)|)$ and $\vec{\vartheta}(\tau)$ is the electron velocity divided by the speed of light c. The times ratio for ultra-relativistic electrons propagating towards the observation point at an angle θ then reads:

$$\frac{\mathrm{d}t}{\mathrm{d}\tau} = 1 - \vartheta \cos\theta = 1 - \sqrt{1 - \frac{1}{\gamma^2}} \cos\theta, \tag{3.3}$$

where γ is the electron energy, measured in units of its rest mass energy, $\gamma = E_e/mc^2$. The angle θ, at which the radiation is emitted, tends to be quite small, as it is connected with γ via $\theta = 1/2\gamma$. With $\theta \approx 0$ and $\gamma \approx 10^4$ the relativistic compression of time experienced at the observation point (Doppler shift) is enormous, that is why the wavelength of the generated radiation is extremely short and lies in the X-ray region. The same relativistic effects cause the different perception of emitted radiation according to two frames - the one moving along with the electron at its centre-of-mass and the other, stationary one, located at an observation point away from the electron. In the electron-rest frame the emitted radiation field resembles that of a standard dipole, whilst in the laboratory frame of reference it becomes significantly elongated in the horizontal direction. The emission of a radiation cone seen in the laboratory frame of reference is depicted in fig. 3.2 (left).

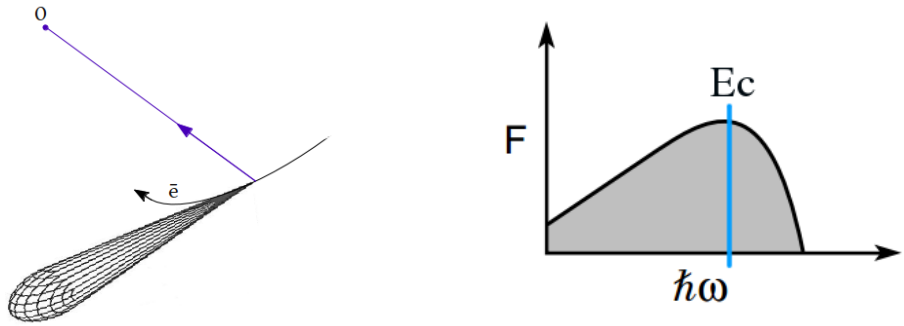

Figure 3.2: Radiation generated by a bending magnet. Left: radiation cone observed in the laboratory frame of reference. Right: typical spectrum as a function of photon flux F against energy $\hbar\omega$ (the picture is taken from [27]).

The spectrum of radiation generated by bending magnets is characterised by critical energy E_c:

$$E_c = \frac{3e\hbar B\gamma^2}{2m}, \tag{3.4}$$

where $\hbar$ is Planck's constant and B is magnetic field. With γ being very large for bending magnets and opening angles lying in the microradians area[1] there is a practical implication on the resulting frequency spectrum - it turns out broad as illustrated in fig. 3.2 (right). At present, bending magnets radiation is used at second-generation synchrotrons, as it is easiest to obtain. One of its main downsides is the limited coverage of the hard X-ray energies.

3.1.2 Wigglers

Wigglers and undulators are both periodic magnetic structures, which have different lengths of periods λ_0. The magnetic fields in wiggler magnets are very

[1] A handy expression for γ is $\gamma = 1957E_e$. The electron energy E_e at the ESRF is around 6 GeV, therefore the opening angles θ are of the order of 40 µrad.

strong, which change the relativistic effect in the horizontal direction: an electron comes through the vertical part of the magnet, it gets a very sharp peak of the field, hence it receives big acceleration, which makes it radiate just as it would do in a strong bending magnet. Subsequently the electron moves towards another side of the period, where it gets another sharp magnetic push the other way, so it turns and radiates again. Hence within one period the electron undergoes two strong kicks, and the amplitude of its trajectory (that resembles sinusoidal) is large. A parameter defining the maximum angle of electron's oscillations in the horizontal plane (non-dimensional magnetic deflection parameter), K, is therefore high.

Each oscillation of the passing electron causes emission of radiation as a harmonic. The number of harmonics, n, is proportional to the value of K (eq. 3.5), and it is usually high as K is high (in the range of 20-40) as well.

$$n = \frac{3K}{4}\left(1 + \frac{K^2}{2}\right). \tag{3.5}$$

At high K the radiated energy appears in high harmonics, and it is emitted at large horizontal angles $\theta \approx K/\gamma$, therefore the collection angles also tend to be large, which leads to spectral merging of nearby harmonics. This results in a continuum at high photon energies, similar to that of a bending magnet radiation, but enhanced by a factor of $2N$, where N is the number of periods (fig. 3.3).

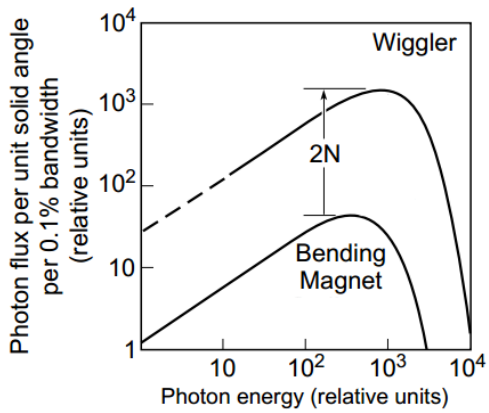

Figure 3.3: Comparison of the spectra generated by bending magnet and wiggler. The graph is taken from [27].

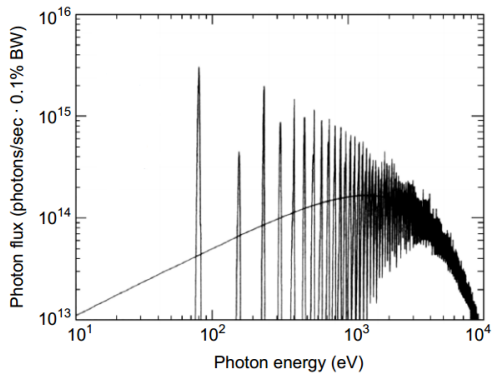

Figure 3.4: A spectrum of a wiggler at Elettra in Trieste, Italy: E=2 GeV, I=0.4 A, λ_u=6 cm, N=72, K=3.7, n=22. The plot is taken from [27].

However, at low photon energies (in the region of the fundamental and the first few harmonics) wigglers exhibits strong interference effects typical of an undulator, therefore the beginning of the spectrum is marked with a dashed line in fig. 3.3. A realistic spectrum of a wiggler is illustrated in fig. 3.4, where there are distinct harmonics at low photon energies, which spectrally merge and create a smooth curve with the increase of the photon energies.

Wigglers are frequently used at synchrotron facilities, as they provide access to higher photon energies and higher photon fluxes than bending magnets, but

are less expensive than undulators.

3.1.3 Undulators

A periodic magnetic structure inside which an electron beam undergoes a sinusoidal trajectory is called an undulator (fig. 3.5). The operating principle of an undulator is rather similar to that of a wiggler, although there are a few major differences. The magnetic deflection parameter K tend to be around unity (eq. 3.6), as the field amplitudes B_0 are not as large as in wigglers (in the order of 0.5 T) and the periods λ_u are shorter than in wigglers (of the order of 50 cm):

$$K = \frac{eB_0\lambda_u}{2\pi mc}. \tag{3.6}$$

The radiation is emitted at a very narrow angle (fig. 3.5): the opening angle of the central radiation cone is inversely proportional to the square root of the number of periods N, $\theta_{cen} \simeq 1/\gamma\sqrt{N}$. Usually, the number of periods is high (of the order of 100), which makes the opening angle lie in the order of 30-40 µrad.

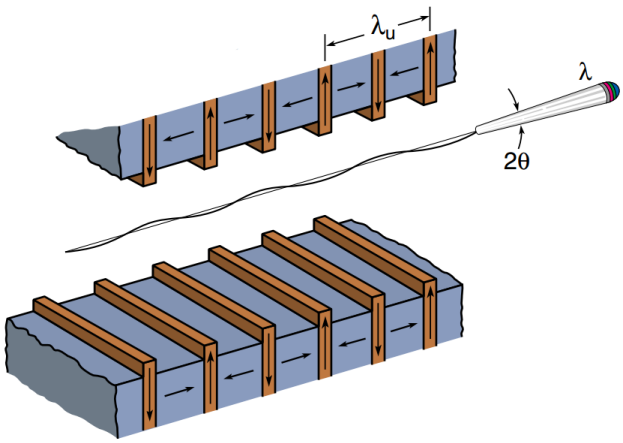

Figure 3.5: Undulator magnetic structure with a period λ_u and an opening angle 2θ. The image is taken from [27].

The spectral bandwidth $\Delta\lambda/\lambda$ of the emitted radiation is also inversely proportional to N, $\Delta\lambda/\lambda = 1/N$, which results in a very narrow bandwidth. That is why undulator radiation has the most brilliance (eq. 1.3), as it comes out from a very small spot in a really narrow cone.

The relationship between a primary radiation wavelength and main undulator parameters unfolds in the following fashion. A relativistic electron is emitting radiation, the wavelength of which in the electron's own moving frame is calculated according to $\lambda' = \lambda_u/\gamma$. The Lorentz transformation of this moving frame into a stationary laboratory one yields a Doppler shortening of the wavelength $\lambda = \lambda'\gamma(1 - \beta\cos\theta)$, where β is the electron speed measured in the units of the velocity of light, $\beta = v/c$. The derivation of the fundamental wavelength of undulator radiation is done with the account of the electron's

transverse motion due to the periodic magnetic field, it reads:

$$\lambda = \frac{\lambda_u}{2\gamma^2}\left(1 + \frac{K^2}{2} + \gamma^2\theta^2\right). \tag{3.7}$$

A typical spectrum of undulator radiation is illustrated in fig. 3.6. In the electron's centre-of-mass frame the emitted harmonics are very sharp and narrow (dashed lines), whilst the Lorentz transformation of this moving frame into a stationary one yields the Doppler broadening of the harmonics (solid line) and introduces the background radiation at off-resonant frequencies. In reality, the off-resonant radiation is filtered out either by a slit or monochromator.

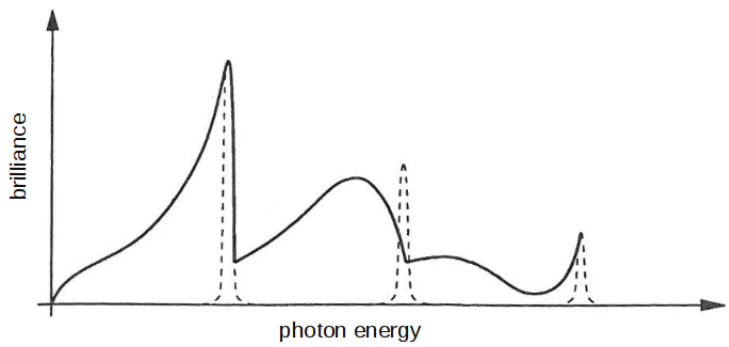

Figure 3.6: A radiation spectrum obtained from an undulator: solid line - spectrum in the laboratory frame of reference; dashed line - spectrum in the electron's centre-of-mass frame. The graph is taken from [7].

Electrons are contained in an electron beam that is going around the storage ring in bunches. Each of these bunches is elliptically shaped in cross-section, as illustrated in fig. 3.7. The horizontal and vertical sizes respectively, σ_x and σ_y, are considered to have Gaussian distributions. The electron density as a function of coordinates $n(x, y)$ inside the bunches is calculated according to:

$$n(x, y) = \frac{N_0}{2\pi\sigma_x\sigma_y} e^{-x^2/2\sigma_x^2} e^{-y^2/2\sigma_y^2}, \tag{3.8}$$

where N_0 is the total number of electrons.
The angular divergences of the beam σ'_x and σ'_y (which are also considered to have Gaussian distributions in the respective directions) are important as well. If σ'_x and σ'_y are smaller than the central radiation cone, then there's no broadening effect on the spectral bandwidth of harmonics; whilst if the divergences are comparable to the central radiation cone, they tend to smears out the sharp peaks, lowering the intensity of the harmonics.

Despite the high cost, undulators are most frequently used at the third-generation synchrotron sources.

3.2 Theoretical concepts underlying the SRW code

The structure of the code consists of two main parts: firstly, an initial wavefront is calculated at an observation distance according to parameters, which

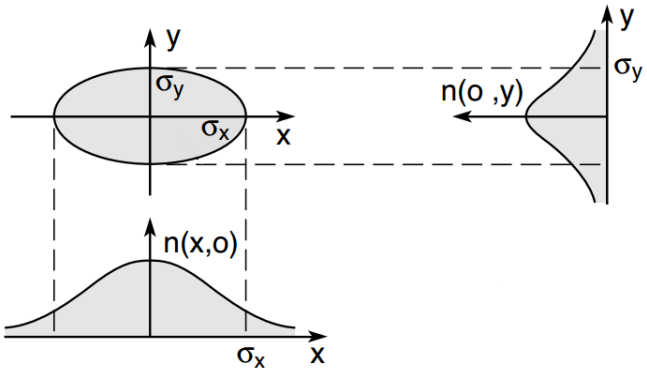

Figure 3.7: Electron beam's spatial parameters: horizontal and vertical dimensions σ_x and σ_y [27].

correspond to those of a source of synchrotron radiation SR (i.e. electric and magnetic fields of an insertion device's magnets, transverse and angular dimensions of the electron bunch, the number of electrons per bunch, its energy and average current, etc.). Secondly, this initial wavefront is propagated along the simulated setup, which can include different optical components, and correspond to a modelled beamline or an instrument of a synchrotron. These two parts are illustrated in fig. 3.8.

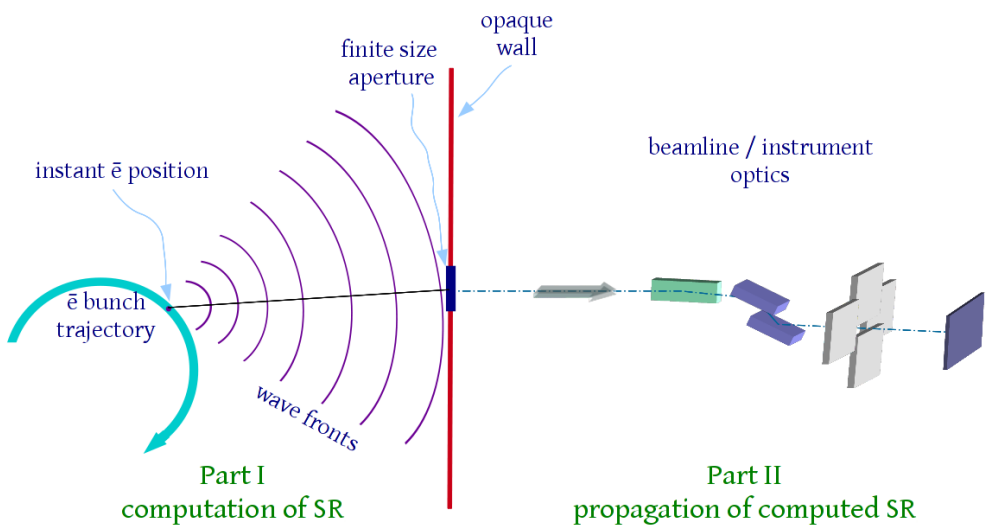

Figure 3.8: Schematic showing the two steps of the SRW code: part I calculates an initial synchrotron radiation wavefront, which is propagated through the components of a beamline in part II. The optical elements are not specified, as they vary for different setups.

Numeric computation of the electric field emitted by a single electron requires high CPU efficiency. In order to avoid having to calculate electric fields of every single electron within a bunch, the total electric field is obtained by averaging the radiation from a single electron over the phase space of the entire

bunch.

3.2.1 Computation of synchrotron radiation

Most of the programmes for computing synchrotron radiation at present use a far field approximation, where the distance between the source and the observation point is large compared to the undulator length, hence diffraction effects are negligible. A near field approximation [28], on the other hand, allows to regard an arbitrary observation distance, however far away or close to the source it might be, hence it allows to account for phenomena of wave nature.

The calculation of synchrotron radiation in SRW is done using an approximation, that could be applicable for both near field and far field observations. The method of determining the electric field of spontaneous emission by relativistic electrons in the frequency domain is based on the scalar and vector retarded potentials (Gaussian system) [29]. The electric field represents an exact solution of the Maxwell equations for such a case:

$$\begin{aligned} \vec{A} &= e\int_{-\infty}^{+\infty} \frac{\vec{\beta}}{R}\delta(\tau - t + \frac{R}{c})\mathrm{d}\tau, \\ \phi &= e\int_{-\infty}^{+\infty} \frac{1}{R}\delta(\tau - t + \frac{R}{c})\mathrm{d}\tau, \end{aligned} \tag{3.9}$$

where $\vec{\beta} = \vec{\beta}(\tau)$ is the electron's instantaneous relative velocity, R is the distance between the observation point $\vec{r}$ and an instant electron position $\vec{r_e}(\tau)$, t is time in the laboratory frame of reference, τ is the integration variable (which has the dimension of time) and $\delta(x)$ is a delta-function. The delta-function represented by a Fourier integral $\delta(t) = \frac{1}{2\pi}\int_{-\infty}^{\infty}\exp(i\omega t)\mathrm{d}\omega$ is inserted in eq. 3.9 yields:

$$\begin{aligned} \vec{A} &= \frac{e}{2\pi}\int_{-\infty}^{+\infty}\exp(-i\omega t)\mathrm{d}\omega\int_{-\infty}^{+\infty}\frac{\vec{\beta}}{R}\cdot\exp\left[i\omega(\tau+\frac{R}{c})\right]\mathrm{d}\tau, \\ \phi &= \frac{e}{2\pi}\int_{-\infty}^{+\infty}\exp(-i\omega t)\mathrm{d}\omega\int_{-\infty}^{+\infty}\frac{1}{R}\cdot\exp\left[i\omega(\tau+\frac{R}{c})\right]\mathrm{d}\tau, \end{aligned} \tag{3.10}$$

where ω is a frequency. Differentiating the potentials and assuming the convergence of all integrals, an expression for the electric field in the time domain is derived:

$$\begin{aligned} \vec{E} &= -\frac{1}{c}\frac{\partial\vec{A}}{\partial t} - \nabla\phi \\ &= \frac{ie}{2\pi c}\int_{-\infty}^{+\infty}\omega\cdot\exp(-i\omega t)\mathrm{d}\omega\int_{-\infty}^{+\infty}\frac{1}{R}[\vec{\beta} - \vec{n}\cdot(1+\frac{ic}{\omega R})]\cdot\exp\left[i\omega(\tau+\frac{R}{c})\right]\mathrm{d}\tau, \end{aligned} \tag{3.11}$$

where $\vec{n}$ is the unit vector at an instant electron's position, which is oriented towards the observation point. An expression for the electric field in the frequency domain is obtained via:

$$\vec{E}_\omega = \frac{ie\omega}{c}\int_{-\infty}^{+\infty}\frac{1}{R}\left[\vec{\beta}-\vec{n}(1+\frac{ic}{\omega R})\right]\cdot\exp\left[i\omega(\tau+\frac{R}{c})\right]\mathrm{d}\tau. \tag{3.12}$$

An analogous derivation of an expression for the magnetic field in the frequency domain $\vec{H} = \nabla\times\vec{A}$ could be concluded as well, however, the estimate $\vec{H} = \bar{\vec{n}}\times\vec{E}$, where $\bar{\vec{n}}$ is the average value of the unit vectors $\vec{n}$, is sufficient.

The approach shown above gives an expression for the electric field defined through the far field approximation (eq. 3.12); yet there are numerous practical cases where an observation point is close to the source and diffraction phenomena must be considered as well. For such cases the expression of eq. 3.12 could still be used with a few additional corrections. The first one is a phase expansion - it accounts for the relativistic motion of an electron and small angles of observation:

$$\tau+\frac{R}{c}\approx\frac{z-z_{e0}}{c}+\frac{1}{2}\left[\tau\gamma_e^{-2}+\int_0^\tau(x_e'^2+y_e'^2)\mathrm{d}\tilde{\tau}+\frac{(x-x_e)^2+(y-y_e)^2}{c(z-c\tau)}\right], \tag{3.13}$$

where γ_e is the reduced electron energy ($\gamma \gg 1$); x, y, z are the horizontal, vertical and longitudinal coordinates of the observation point $\vec{r}$ respectively; x_e and y_e are the transverse coordinates of an electron trajectory; x_e' and y_e' are the transverse components of the velocity vector $\vec{\beta}$ and z_{e0} is the initial longitudinal electron position. The second correction involves the transverse components of the unit vector $\vec{n}$ from eq. 3.12 to be approximated according to:

$$n_x\approx\frac{x-x_e}{z-c\tau};\qquad n_y\approx\frac{y-y_e}{z-c\tau}. \tag{3.14}$$

The third correction is acquired through solving the equation of motion under the influence of the Lorentz force in an external magnetic field. It allows to obtain a correlation between the transverse coordinates and angles of the electron's trajectory and τ. It is presented in a linear approximation:

$$\begin{pmatrix}x_e\\y_e\\x_e'\\y_e'\end{pmatrix}\approx\mathbf{A}\begin{pmatrix}x_{e0}\\y_{e0}\\x_{e0}'\\y_{e0}'\end{pmatrix}+\mathbf{B}, \tag{3.15}$$

where $\mathbf{A} = \mathbf{A}(\tau)$ is a 4×4 matrix and $\mathbf{B} = \mathbf{B}(\tau)$ is a vector with scalar functions components.

The approximations in eq. 3.13 - 3.15 consider a variety of distances between an electron's instantaneous position and the observation point, therefore the electric field calculated under these assumptions is acceptable for observation also in the near field range. Moreover, to simplify the electric field calculation, integration in eq. 3.12 and 3.13 is done over a finite interval through defining a finite aperture.

The electric field acquired via eq. 3.12 represents radiation emitted only from a single electron. In reality, electrons travel around storage rings in bunches, thus they provide an average electron current I. An important characteristic of a photon beam, which is provided by an electron bunch, flux, is

defined as the number of photons dN_{ph} per unit time dt per relative spectral interval $d\omega/\omega$ per electron current I and is correlated with the frequency domain electric field of the electron bunch:

$$\frac{\mathrm{d}N_{ph}}{\mathrm{d}t(\mathrm{d}\omega/\omega)I} = \frac{c^2\alpha \mathrm{d}S}{4\pi^2 e^3 N_e}|\vec{E}_{\omega,\mathrm{bunch}}|^2, \tag{3.16}$$

where α is a fine structure constant. The square amplitude of the bunch electric field $|\vec{E}_{\omega,\mathrm{bunch}}|^2$ is defined through a sum of two components, incoherent and coherent synchrotron radiation respectively:

$$\begin{aligned}|\vec{E}_{\omega,bunch}|^2 \approx N_e \int & |\vec{E}_\omega(\vec{r}; x_{e0}, y_{e0}, x'_{e0}, y'_{e0}, \gamma_{e0})|^2 \\ & \times \tilde{f}(x_{e0}, y_{e0}, x'_{e0}, y'_{e0}, \gamma_{e0})\mathrm{d}x_{e0}\mathrm{d}y_{e0}\mathrm{d}x'_{e0}\mathrm{d}y'_{e0}\mathrm{d}\gamma_{e0} \\ & + N_e(N_e-1)|\int \vec{E}_\omega(\vec{r}; x_{e0}, y_{e0}, x'_{e0}, y'_{e0}, \gamma_{e0}) \\ & \times f(x_{e0}, y_{e0}, x'_{e0}, y'_{e0}, \gamma_{e0})\mathrm{d}x_{e0}\mathrm{d}y_{e0}\mathrm{d}x'_{e0}\mathrm{d}y'_{e0}\mathrm{d}\gamma_{e0}|^2,\end{aligned} \tag{3.17}$$

where $\vec{E}_\omega$ is the electric field emitted by a single electron with initial phase-space coordinates $x_{e0}, y_{e0}, x'_{e0}, y'_{e0}, \gamma_{e0}$ and $f(x_{e0}, y_{e0}, x'_{e0}, y'_{e0}, \gamma_{e0})$ is the electron distribution function in 6D phase space.

3.2.2 Propagation of the computed synchrotron radiation

The concept exploited in the second part of the code is illustrated in fig. 3.9. In the first part of the code the electromagnetic field of the radiation wavefront of a single electron at a position $P_e(x_e, y_e, z_e)$ is calculated at a distance $P_1(x_1, y_1, z_1)$. It is determined within a finite aperture A (marked as a pink coloured rectangle in fig. 3.9). The second part of the programme propagates the field from P_1 to an observation point $P_2(x_2, y_2, z_2)$ at a distance S. In order to compute a field at this point, the Kirchhoff integral theorem is applied [30].

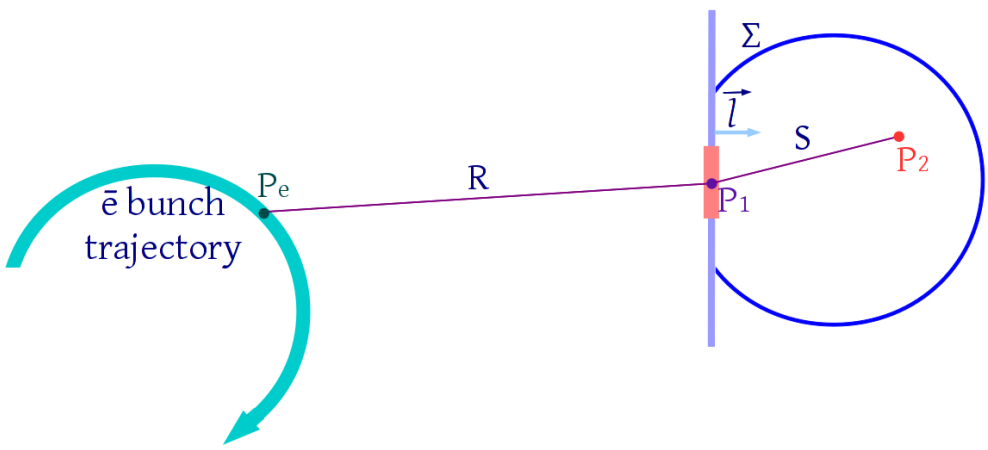

Figure 3.9: Illustration explaining the basis of the Kirchhoff theorem.

This theorem allows calculation of an electric field of synchrotron radiation at the point P_2 (fig. 3.9) from the values of the electric field and its derivative at each point of an arbitrary surface Σ enclosing the point P_2:

$$U(P_2) = \frac{1}{4\pi} \iint_\Sigma \left[U \frac{\partial}{\partial \vec{l}} \left(\frac{\exp(ikS)}{S} \right) - \frac{\exp(ikS)}{S} \frac{\partial U}{\partial \vec{l}} \right] \mathrm{d}\Sigma \tag{3.18}$$

To derive an expression exploited in the SRW code, Kirchhoff boundary conditions are applied to the transverse components of the electric field of single electron (eq. 3.12), which yields:

$$\vec{E}_{\omega 2\perp}(P_2) \approx \frac{k^2 e}{4\pi} \int_{-\infty}^{+\infty} \mathrm{d}\tau \iint_A \frac{\vec{\beta}_{e\perp} - \vec{n}_\perp}{RS} \exp[ik(c\tau + R + S)] \cdot (\vec{l} \cdot \vec{n}_{p_e p_1} + \vec{l} \cdot \vec{n}_{p_1 p_2}) \mathrm{d}\Sigma, \tag{3.19}$$

where $\vec{n}_{p_e p_1}$ and $\vec{n}_{p_1 p_2}$ are unit vectors from P_e to P_1, and from P_1 to P_2 respectively and $\vec{l}$ is a unit vector normal to the surface Σ, which is directed towards P_2. The necessary conditions for eq. 3.19 to be valid are $\lambda \ll R$ and $\lambda \ll S$; it is representing a coherent superposition of the radiation wavefronts from virtual point sources located along the electron's trajectory (the amplitudes and phases of which are correlated with their positions). This is a generalised version of the Kirchhoff-Helmholtz theorem, which is used in calculations at large observational angles (when $(\vec{l} \cdot \vec{n}_{p_e p_1} + \vec{l} \cdot \vec{n}_{p_1 p_2})$ is greater than two). Observation at small angles, on the other hand, reduces eq. 3.19 to a well-known Huygens-Fresnel principle:

$$\vec{E}_{\omega 2\perp}(P_2) \approx \frac{k}{4\pi i} \iint_A \vec{E}_{\omega 1\perp}(P_1) \frac{\exp(ikS)}{S} (\vec{l} \cdot \tilde{\vec{n}} + \vec{l} \cdot \vec{n}_{p_1 p_2}) \mathrm{d}\Sigma, \tag{3.20}$$

where $\vec{E}_{\omega 1\perp}(P_1)$ is the electric field at P_1 calculated according to eq. 3.12.

In practice, the implementation of the described above theorem is done in a following way. Firstly, the entire beamline of interest (or an instrument that's being modelled) is presented in a table format where each component is defined parametrically. For instance, a parabolic refractive lens is specified through its radius of curvature at the tip of the parabola, its geometrical aperture, refractive index decrement, absorption coefficient and a focal length. The propagation of radiation between parallel planes with no refractive media is also a separate element of the component's table, it is referred to as drift space and is defined by a mere distance. Secondly, propagation of electric fields through the components of this table is done according to eq. 3.19 or eq. 3.20. The application of these equations is different depending on the type of an element of the component's table. For example, the propagation of the electric field through a drift space is calculated according to:

$$\vec{E}_{\omega 2\perp}(x_2, y_2) \approx \iint \vec{E}_{\omega 1\perp}(x_1, y_1) \exp[ik[L^2 + (x_2 - x_1)^2 + (y_2 - y_1)^2]^{1/2}] \mathrm{d}x_1 \mathrm{d}x_2, \tag{3.21}$$

where L is the drift space distance. Propagation of the electric field through any optical component that could fall under a thin lens approximation (most

of the focusing optics, for instance) is done through a multiplication of the field by a complex transmission function T_{12}, which takes into account a phase shift and attenuation phenomena:

$$\vec{E}_{\omega 2\perp}(x,y) \approx \vec{E}_{\omega 1\perp}(x,y)T_{12}(x,y). \tag{3.22}$$

In those cases where the thin lens approximation isn't applicable (so-called "thick" optical elements), the electric field is determined via:

$$\vec{E}_{\omega 2\perp}(x_2,y_2) \approx G(x_2,y_2,\omega)\exp[ik\Lambda(x_2,y_2,k)]\vec{E}_{\omega 1\perp}(x_1(x_2,y_2),y_1(x_2,y_2)). \tag{3.23}$$

The different routines mentioned above propagate the synchrotron radiation emitted only by a single electron. This electron's initial contribution is integrated over an entire phase-space volume occupied by the beam to consider the radiation impact from the remaining electrons of the bunch.

$$\begin{aligned} I_\omega(x,y) = &\int I_{\omega_0}(x,y;x_{e0},y_{e0},z_{e0},x'_{e0},y'_{e0},\delta\gamma_{e0}) \\ &\times f(x_{e0},y_{e0},z_{e0},x'_{e0},y'_{e0},\delta\gamma_{e0})\mathrm{d}x_{e0}\mathrm{d}y_{e0}\mathrm{d}z_{e0}\mathrm{d}x'_{e0}\mathrm{d}y'_{e0}\mathrm{d}\delta\gamma_{e0} \end{aligned} \tag{3.24}$$

3.3 Simulation example

To exemplify the practical implementation of the above theory, a model of a coherent hard X-ray beamline (CHX) at a building synchrotron NSLS-II is presented [31], [32]. The simulations were done by Oleg Chubar[2].

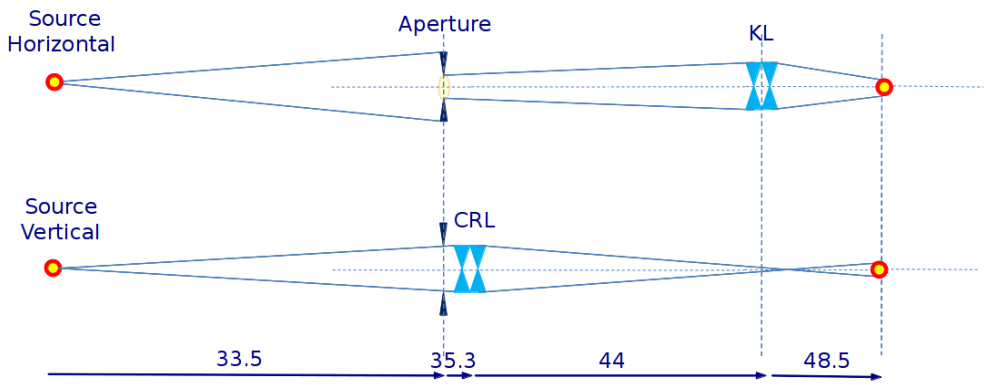

Figure 3.10: Setup of the current design of the CHX beamline: horizontal focusing is done with the help of a kinoform lens KL, whilst the vertical focusing is performed with a compound refractive lens CRL. Image is the courtesy of A. Fluerasu, L. Wiegart and K. Kaznatcheev.

[2]Although simulations of the CHX setup were also performed in McXtrace by the author, they are not illustrated in the discussion.

The beamline will be dedicated to studies of nanometre-scale dynamics in materials using X-ray photon correlation spectroscopy, and to other experimental methods enabled by bright and coherent X-ray beams. The optical elements are focusing the incoming X-ray beam in 2D carefully considering different degrees of coherence to match it to those required for particular experiments. For instance, a typical experiment in a SAXS geometry requires a beam spot, the FWHM size of which is 10 - 20 µrad, whilst for a WAXS geometry the spot has to be reduced to 2 µm. Schematic of the current design of the beamline targeted for experiments in SAXS geometry is illustrated in fig. 3.10.

The radiation from the undulator source with the electron beam size of 34 µm and 8 µm and angular divergence 18 × 9 µrad^2 in the horizontal and vertical directions respectively is calculated at the entry aperture, 33.5 m downstream the source (fig. 3.11). The photon energy used in the calculation is 10 keV. The graphical representation of the calculated data is done automatically in IgorPro, therefore the images are shown in the original format. The photon beam is dominant in the horizontal direction, therefore its horizontal cross-section is broader than the vertical.

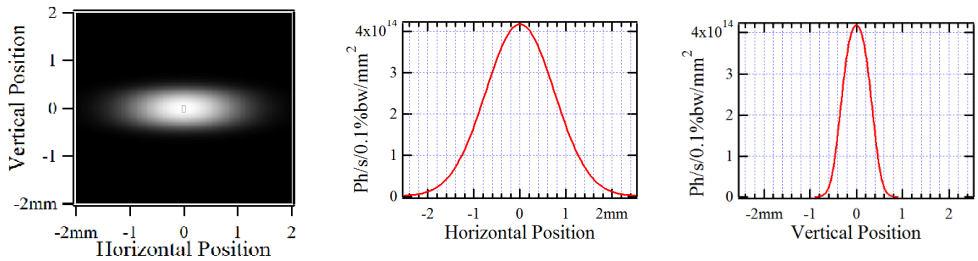

Figure 3.11: Synchrotron radiation distribution at the aperture, 33.5 m away from the source. Left: spatial distribution; middle and right: cross-sections of the spatial distribution along the horizontal and vertical axes.

The current example presents a model of the beamline with an aperture opening 44 × 100 µm^2 in the horizontal and vertical directions respectively. In fact, the vertical opening of the aperture varies according to the degree of coherence one wants to preserve for a particular experiment, the largest opening used in calculations was 1 mm. The spatial distribution of the photon beam before the next beamline component - one-dimensional cylindrical Beryllium CRL is illustrated in fig. 3.12, 35.3 m downstream the source.

The diffraction of the photon beam on the aperture edges is depicted in the spatial distribution image. As the entry aperture cuts off a significant portion of the radiation horizontally, the diffraction ripples are smaller in the respective direction, compared to the ones on the vertical section. The location of the CRL is only 1.8 m downstream the aperture, therefore the shape of the cut-off beam is rectangular, its size is comparable to the aperture.

The next optical component in the beamline is a horizontally focusing Silicon refractive lens with kinoform profiles; it is located at a distance of 44 m from the source, slightly before the CRL's focal waist. The spatial distribution of the beam before the element is presented in fig. 3.13. The beam at this position is already vertically focused, whilst horizontally it remains more or less unchanged

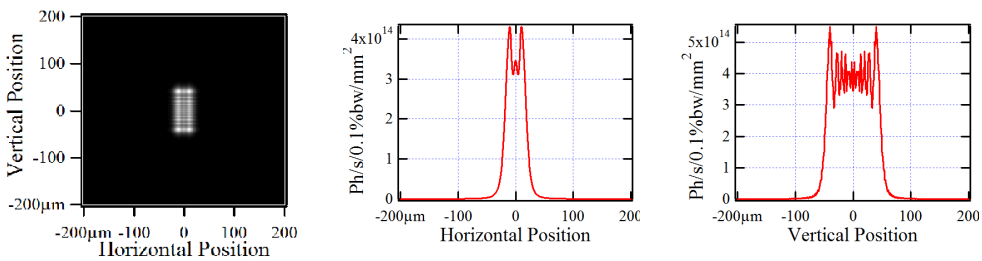

Figure 3.12: Radiation distribution before the CRL, 35.3 m downstream the centre of undulator. Left: spatial distribution; middle and right: respective cross-sections of the initial distribution.

(aside from its slight increase due to the natural divergence of the beam). The ripples from diffraction observed at the previous position are preserved through the beam's further propagation, but they are not as distinct as before.

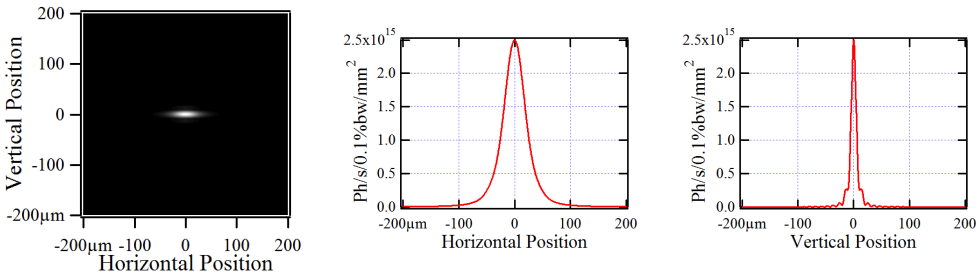

Figure 3.13: Radiation distribution before the KL, 44 m downstream the centre of undulator. Left: spatial distribution; middle and right: respective cross-sections of the initial distribution.

Finally, the photon beam's spatial distribution at the sample plane, 48.5 m away from the undulator is shown in fig. 3.14. High demagnification of the kinoform lens in combination with a nearly 3:1 focusing proportion of the CRL obtained a spot of 8 × 14 µm^2 in the horizontal and vertical directions respectively.

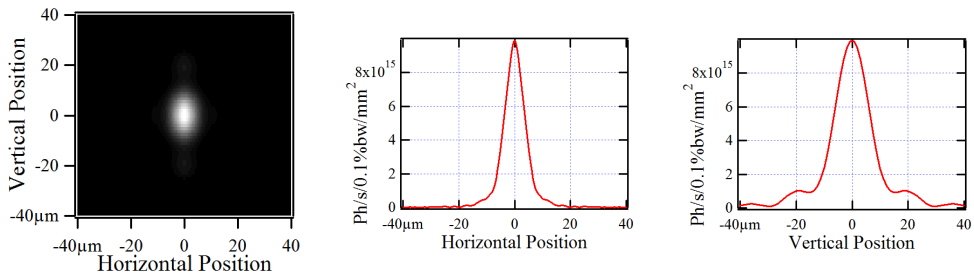

Figure 3.14: Dimensions of the focused spot at the sample position, 48.5 m downstream the centre of undulator. Left: spatial distribution; middle and right: respective cross-sections of the initial distribution.

3.4 Advantages and limitations of SRW

At present, the SRW code is one of the most reliable programmes for computation of synchrotron radiation: modelling results provided by the code are consistent and reproduce experimentally obtained values with high precision (chapter 5). Modelling of partially coherent radiation wavefronts is possible only with the SRW package.

However, the method implemented for the near field computation of synchrotron radiation has several limitations. Firstly, the input data should be consistent. For a correct calculation of synchrotron radiation (i.e. for a proper set up of the radiation sampling and an integration mode), the magnetic field should be defined as a function of the longitudinal position, whilst parameters of the electric field should allow explicit determination of an average trajectory. These two independent parameters must be mutually consistent, otherwise the SRW code can terminate the calculation with an error message.

Secondly, the optical components library is not diverse yet: there are a few actual components (lenses and mirrors), but some complex optics are modelled through a thin lens approximation.

Thirdly, SRW computation is rather time- and computer power-consuming relative to ray-tracing packages. However, it is one of the fastest codes among other physical optics packages (compared with PHASE, for instance). And finally, the current development of the code is far ahead of its documentation.

Chapter 4

Small angle X-ray scattering instrument: simulation versus experiment

The chapter describes an examination of the performance of a SAXS instrument installed at the Department of Life Science at the University of Copenhagen, which was assembled by a commercial company SAXSLAB ApS. A propagation of the X-ray beam was investigated through a number of images of the beam at different distances along the instrument's axis.

Firstly, the principle components of any SAXS instrument are introduced. Secondly, the setup is described in details, which is followed by characterisation of the experiment. The simulation model is then presented along with the preliminary results. First comparisons revealed significant discrepancies, which raised many questions about the correctness of the simulation model. A few suggestions were made about the possible origin of disagreements, therefore an adjusted simulation model was then proposed. Results obtained with the new model complied with those acquired experimentally very well. The chapter is finalised with a broad discussion on the subject of authenticity of the adjusted simulation model.

4.1 Principles about small-angle X-ray scattering technique

The idea behind the method of small angle X-ray scattering (SAXS) lies in the structural analysis of objects whose size is of the order of nanometers [33], [34]. The diffraction pattern after the interaction of the incoming beam with samples, whose inter-atomic distances are of the same order of magnitude as the radiation, lies in the small angle region, hence the origin of the name for the method. The diffraction properties of an object depend hugely on its degree of structural ordering: the less the object is ordered, the less informative its scattering is. That is why the SAXS method is commonly used for analysing the inner structure of disordered systems.

Typical objects investigated by this method are: biologically active substances - macromolecules and their complexes (proteins, viruses, membranes,

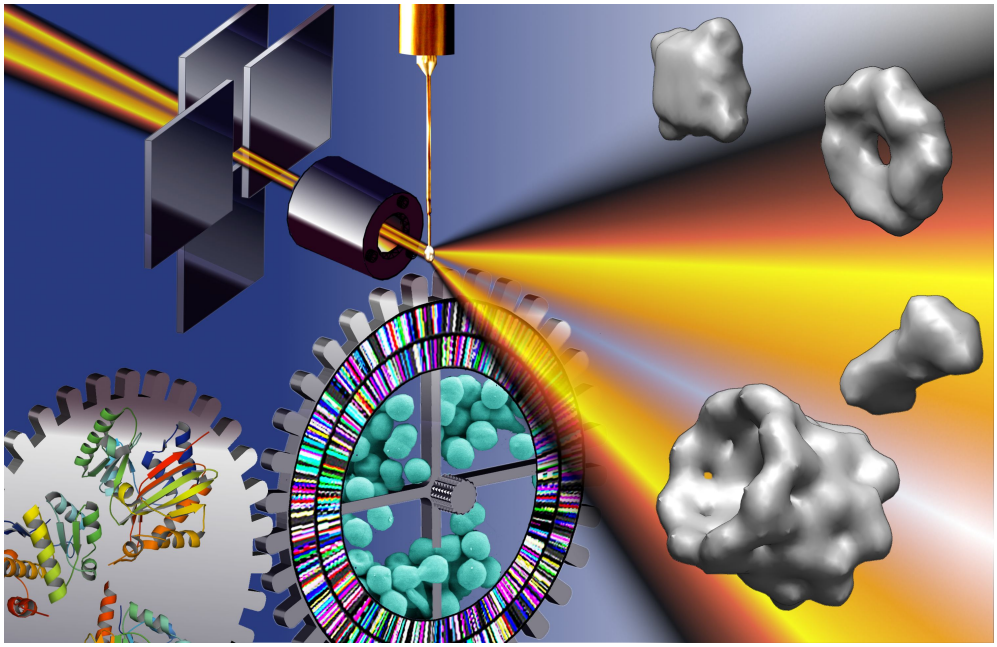

Figure 4.1: Examples of the samples investigated by the SAXS technique: proteins and membranes. The picture is taken from [35].

etc.); polymeric materials (natural and synthetic polymers); amorphous solids and liquids (the method allows to study the thermodynamic parameters and the cluster structure of liquids, fluctuations and phase decomposition); metals, alloys and powders (different features of structure).

The current section centres on the basic description of instrumentation for SAXS. A small-angle scattering instrument usually consists of three major parts, which will be discussed in detail below:

- A source of X-ray radiation.
- A beam collimation system.
- A detector of scattered radiation.

4.1.1 Radiation sources for SAXS

A source of radiation commonly used in a lab environment is an X-ray tube. A typical example is a sealed tube (fig. 4.2), which contains a filament and an anode in a vacuum housing. The filament is heated up by the electric current, which liberates electrons from its surface and subsequently they impinge on the anode. This interaction generates X-ray photons, whose spectrum has two distinct components, as illustrated in fig. 4.3. The continuous part is due to the electrons' deceleration and eventual stopping inside the anode. It is known as bremsstrahlung radiation and it has a maximum energy that corresponds to the high voltage applied to the tube. The second component of the spectrum include sharp lines, which appear from the following process. The electronic bombardment of the anode removes some of the atomic electrons from their

inner shells and creates vacancies. These vacancies are then filled by electrons from the outer shells. Such electronic transitions produce emission of X-ray photons with a characteristic energy equal to the differences between the two shells. It is known as fluorescent radiation. The monochromatic peaks are several orders of magnitude higher in intensity than the bremsstrahlung.

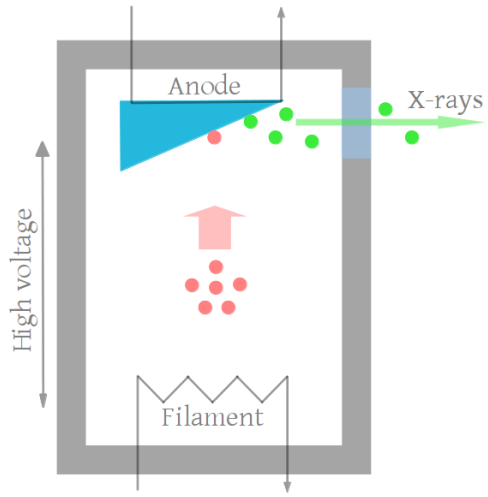

Figure 4.2: A basic design of a sealed X-ray tube.

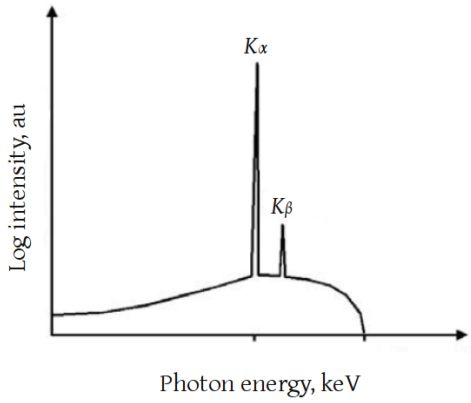

Figure 4.3: Typical spectrum produced by an X-ray tube with characteristic lines.

The tubes are produced with different metallic anodes because the wavelengths of characteristic radiation for diverse SAXS experiments usually vary within the range of 0.71 Å (Mo) to 2.3 Å (Cr). The longer wavelengths are normally not used, due to their high absorption. There are two types of X-ray tubes: one with a point focal spot and another with a linear focal spot, used for point and slit collimation systems respectively.

The constant localised electron bombardment of the anode by electrons wears out the X-ray tube, as the anode's material vaporises and becomes thinner. By spinning the anode the heat can be dissipated over a larger volume than in a standard tube, allowing the total power to increase and extend the anode's lifetime. The maintenance of rotating anode tubes is much higher than that of the sealed ones, as the vacuum in the former device is provided by running pumps, hence the system is less stable.

The power of an X-ray tube lies in the range of several watts to several kilowatts. The photon flux of a tube with a rotating anode can be up to ten times higher than that of a sealed one. Therefore, the most powerful X-ray tubes are those with rotating anodes.

4.1.2 Collimation systems

In terms of collimation systems, there are a variety of cameras, described in [33]. In a point collimation system, for instance, there is a set of circular diaphragms, arranged in such a way so the radiation from the source is collimated into a

narrow beam under an approximation of plane-wave conditions. A schematic is shown in fig. 4.4 (left). Only a small part of the investigated sample is illuminated, which results in a low scattering intensity. The resolution can be improved by an increased sample-to-detector distance, which results in an instrument of several meters long and reduces the intensity at the detector. The observed scattering pattern consists of concentric circles around the primary beam.

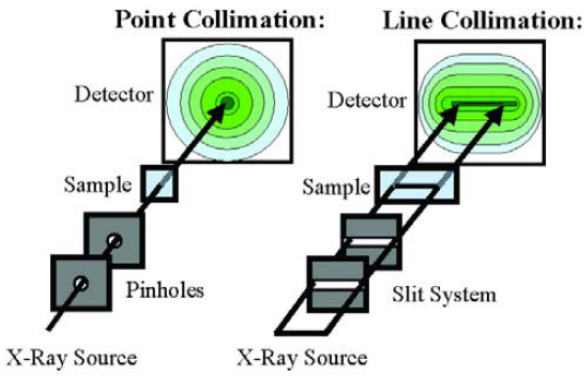

Figure 4.4: The two types of collimation systems. The picture is taken from [36].

Another example is a slit (or lines) collimation system [34], depicted in fig. 4.4 (right). Such a design allows much more light into the instrument (about 50 to 100 times higher than in the case of the point-collimation system), as it confines the beam only in one dimension, and the illuminated sample volume is larger. The beam profile is more narrow, so the sample-to-detector distance is short, which results in higher intensity at the detector. However, the large sample volume introduces significant broadening of the scattering pattern (due to slit smearing), which means that the beam profile has to be taken into consideration upon further data analysis.

4.1.3 Detectors for SAXS

The radiation detectors for small-angle instruments are targeted to the primary radiation in the soft X-ray region (from 5 to 20 keV). There are several types of detectors most commonly used: wire detectors, CCD detectors, imaging plates and solid state detectors.

Wire detectors have thin wires in the absorption chamber, which is filled with gas (Xe or Ar/Methane). When entering the chamber, the X-ray photon expels an electron from the gas molecules, which is accelerated towards the wire by the applied high voltage. When the electron hits the wire, an electrical pulse is induced inside the wire, which propagates towards both ends of the wire where its arrival is registered. The time difference between the two registries signifies the position at which the wire was hit. Many parallel wires can reproduce a 2D scattering picture. These detectors can be easily damaged and are expensive to maintain.

In CCD detectors the visible light, which is produced by a fluorescent screen, is detected. A glass fiber plate is mounted between the fluorescent screen and the video chip; it guides the light to the chip and maps the fluorescent pattern. A beryllium window filters out visible light allowing the weak fluorescent signal to be detected. The detector collects produced electrons in every pixel until the measurement is read out. Only the resulting charge is recorded and not the photon impact itself. Because of that the filtering of pulses to eliminate the dark-count rate is not possible. To keep the dark-count rate as low as possible, CCD cameras need cooling. The prices of the detectors are relatively high, as they are proportional to the chip quality.

Imaging plates are flexible sheets which are exposed as photographic films and are scanned by a separate device in a second step. They are made of a material that stores the X-ray energy by exciting electrons into so-called F-traps. The illumination with a laser beam brings back the electrons from these meta-stable energy states. After the registry the imaging plates are cleaned with a light pad before the next use. The plates have almost no maintenance cost and they are not easily damaged by overexposure. However, the necessity of being scanned by an external device makes the automated operation impossible.

Solid state detectors are Si-diodes which record the X-rays directly. When photons hit the semiconductor material, they produce ion pairs that are counted. Then an additional circuitry filters out only those pulses that are above a certain threshold. This way the dark count rate and also fluorescence of longer wavelengths are eliminated. Their radiation hardness is not unlimited and direct beam intensities applied for a long time can cause damage, resulting in permanently reduced quantum efficiency. The cost range of these detectors is comparable to that one for the CCD cameras.

4.2 Geometry of the SAXS instrument

The setup of the instrument used for the experiment is depicted in fig. 4.5. The machine consists of three major parts: the source block, the collimation system and the experimental chamber, which are indicated by blue/green, pale blue and grey colours respectively in fig. 4.5.

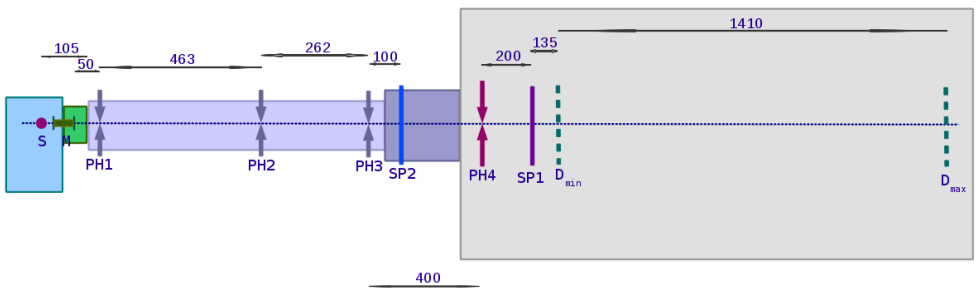

Figure 4.5: The geometrical layout of the instrument's components along with the distances between them in mm: X-ray source S, multilayer mirrors M, pinholes PH1-PH3, sample plates SP1-SP2 and a detector D.

4.2.1 The source block

The source block comprises of two smaller parts marked in light blue and green: the X-rays are produced by a rotating anode[1], which is depicted as a magenta spot in the light blue box. A magnified view of the elements inside the source block is shown in fig. 4.6.

The X-rays are generated in the source, S, pass through the entry aperture, A, and interact with the elliptic side-by-side Kirkpatrick-Baez multilayer mirrors, Ml. The centre of the Ml is placed 45 mm away from the source, the angle of incidence at the centre of the mirrors is 1.2°, therefore the inclination of the propagation axis[2] is approximately 1.7°.

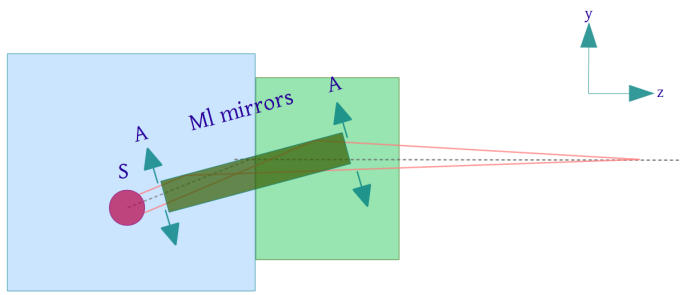

Figure 4.6: Magnified view of the source block with the X-ray source, S, entry and exit apertures, A, and multilayer mirrors, Ml.

Both the entry and exit apertures are square, and are adjacent to the mirrors; the entry aperture collimates the incident beam and the exit aperture shapes the outcoming beam. The aperture openings are identical, and are 1.5 mm. The focal distance of the multilayer mirrors is 900 mm. Each mirror has a length of 60 mm and a width of 20 mm. The side-by-side placement of the mirrors relative to one another is shown in fig. 4.7.

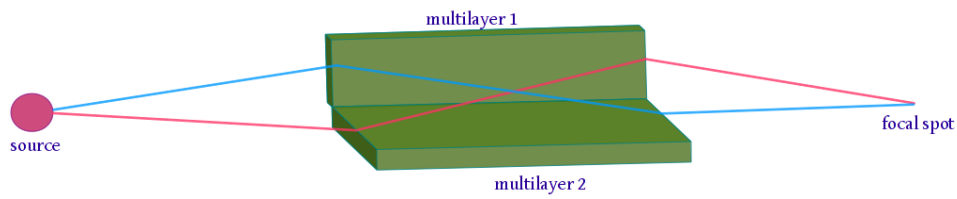

Figure 4.7: Geometry of the side-by-side Kirkpatrick-Baez multilayer mirrors.

The mirrors' construction is elliptically curved in 1D, which means that one mirror focuses the beam in the horizontal direction and the other - in the vertical direction, therefore there are two of them to focus the beam in both directions. Upon manufacturing when the two mirrors were put together and glued there remained a small gap in the centre[3], which was shuttered by a Si

[1]The anode material is copper, hence the primary radiation energy of the characteristic Cu K_α edge is 8.05 keV.

[2]The geometry is rather simple: $1.2 \cdot 2 \cdot \sqrt{2} \approx 1.7$.

[3]Due to the curvatures of individual mirrors.

plate. The multilayers consist of 60 tungsten (W) and boron carbine (B_4C) bilayers with a fraction of the bottom layer Γ=0.667. The d-spacing of the multilayer varies from 20 to 55 Å with roughly 40 Å in the centre.

4.2.2 The collimation and detection systems

The collimation system is coloured in pale blue: it consists of a hollow metal tube with three pin-hole plates mounted inside it, referred to as PH with consecutive numbers in fig. 4.5. The block ends with an extension accessible for experimentalists, which is depicted in darker blue colour, it hosts SP2 - a special plate for liquid samples.

The final part of the instrument is shown in another shade of grey in fig. 4.5, it is commonly referred to as a vacuum chamber. Inside it there is an additional pin-hole, PH4, followed by the main sample plate SP1. The X-ray detector used in the instrument, Pilatus 300K, is also mounted inside the chamber, its mobility along the propagation axis is shown with extreme positions Dmin and Dmax.

There are two modes of operation of the SAXS instrument that depend on a sample of investigation. In the first mode a solid sample is located at SP1, so the collimation of the beam occurs via PH1, PH3 and PH4. In the second mode, on the other hand, a liquid sample is placed at SP2 inside the so-called "sleeve", therefore PH1, PH2 and PH3 are used for collimation.

4.3 The experimental description

Since one of the main aims of the experiment was to follow the propagation of the X-ray beam along the instrument and to develop a model of it in McXtrace, a set of images was taken at different distances that was subsequently used to validate and compare the simulation results.

During the experiment the SAXS machine was disassembled: the metal tube (fig. 4.5) containing pin-holes was taken out leaving the source block and the vacuum chamber firmly mounted to the optical table. As the main goal was to measure the beam's development along the propagation axis, the Pilatus detector had to be taken out of the chamber and put in front of the source to be able to register the beam's passage through the "sleeve". Hence, there were two modes of data acquisition: the so-called "out of the chamber" mode and the "inside the chamber" mode.

The first mode is illustrated in fig. 4.8. The Pilatus detector was taken out of the chamber and placed exactly in front of the source block. The sensitive plate, P, was located inside the detector box, approximately 100 mm away from the front end, which was taken as a reference point of the detector movements. The closest distance at which the beam was measured was 160 mm downstream from the centre of the mirrors that served as a reference point from the source side. The step size was chosen to be 150 mm, so the detector box was manually moved by experimentalists to consecutive positions, i.e. 310 mm, 460 mm, etc. The furthest measurement of the outside of the chamber mode was at 1060 mm downstream the mirrors' centre, at which the detector box was hampered by

the wall of the vacuum chamber. A total of seven measurements were made in this mode.

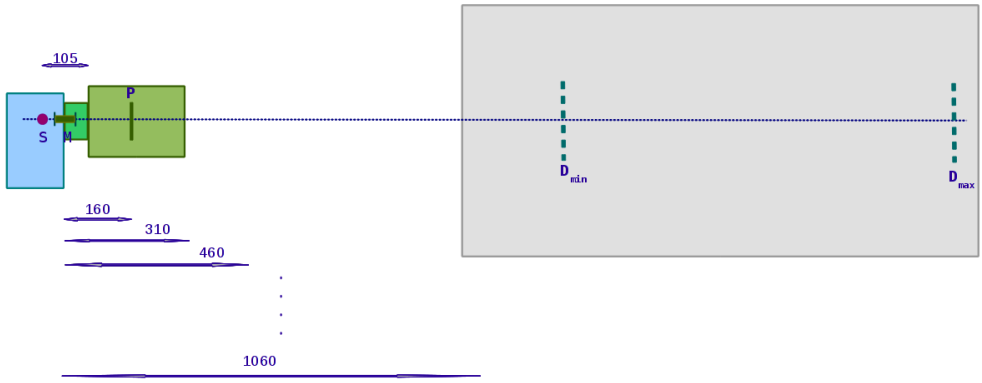

Figure 4.8: Measurement setup for the "outside of the chamber" mode.

After that the detector was relocated to its original position inside the chamber, and the "inside of the chamber" measurements were initiated. The Dmin position coincided with the front end of the detector box, hence the location of the sensitive plate, P, was 100 mm further away (fig. 4.9). Therefore the first measurement of the beam in this mode was performed at 1640 mm downstream the mirrors' centre. Then, again with a step size of 150 mm the detector was moved further away from the source, this time the movement was executed by a built-in mechanical motor. The total distance of the vacuum chamber allowed for eleven measurements in the "inside" mode.

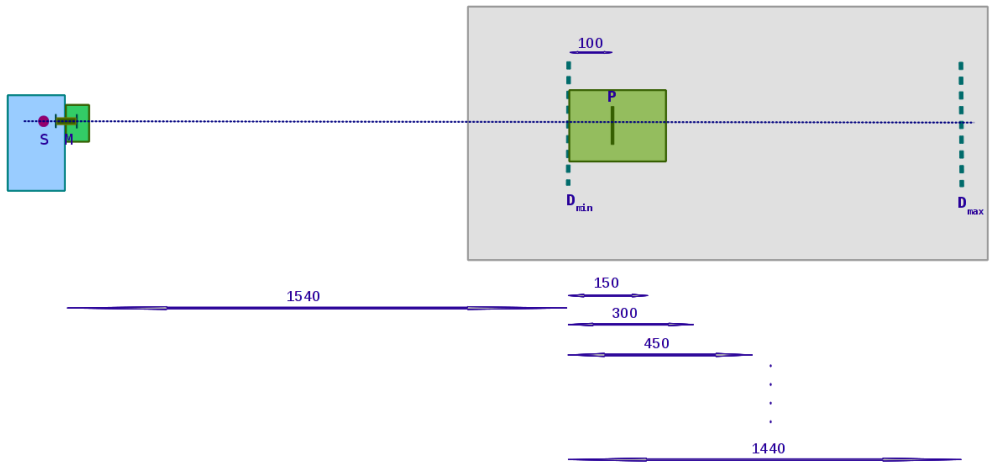

Figure 4.9: The second mode measurement, "inside the vacuum chamber".

The general settings of the system for the day of the experiment were the following: high voltage 42 kV, anode current 0.92 mA, filament voltage 6.2 V, magnetic lens voltage 653 V, magnetic lens current 0.27 mA, water temperature 22 °C and bias grid voltage 178 V.

Initially, when the experiment was being set up, it was discovered that even

the minimal X-ray exposure time, i.e. 1 ms, led to saturation of the detector. In order to prevent this eight layers of aluminium foil were used to shade the source to lessen the intensity.

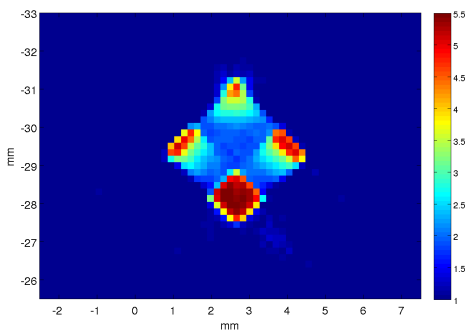

Figure 4.10: The first beam's image corresponding to detector's closest position to the source at 0.16 m.

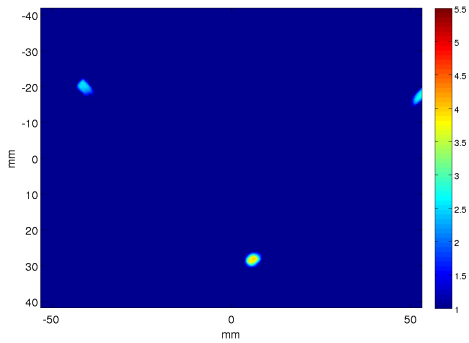

Figure 4.11: The last image corresponding to the detector's furthest from the source position at 3.05 m.

The results of the experiment are presented, discussed and compared thoroughly to those of the simulations later in the chapter, whilst for now the first and the last images are shown in fig. 4.10 and fig. 4.11.

The experimental images reveal four (fig. 4.10) and three (fig. 4.11) spots: a top spot due to the direct beam that disappears with distance (hence it is absent in fig. 4.11), two side spots due to single reflections from the mirror plates and the bottom spot due to the doubly reflected beam. During routine operation of the instrument only the bottom beam is used, whereas the remaining three spots are filtered out by the collimation system.

4.4 McXtrace modelling of the instrument

The experimental separation of data acquisition into two modes was dictated by the initial placement of the detector camera (inside the vacuum chamber), hence the impossibility of obtaining all data in one set. During modelling of the instrument, on the contrary, there was no necessity of introducing separate modes. The simulation setup is presented in fig. 4.12.

The rotating anode was approximated by a *Source_gaussian* component. It is characterised by a Gaussian intensity distribution in the transverse plane, the RMS of which was set to 10.6 µm (corresponding to the FWHM of 25 µm) both vertically and horizontally. The placement of the source component set an origin for the instrument. The X-rays were emitted from the source in a cone with a spatial angle of 4 mrad, which is the divergence of the beam. The distance to the first component after the source, the entry aperture, is 15 mm. The centre of the slit was placed relative to the origin. The next component of the instrument, the multilayer system, followed the entry aperture immediately. Its centre was half of the mirrors' length, i.e. 30 mm, away from the slit, which

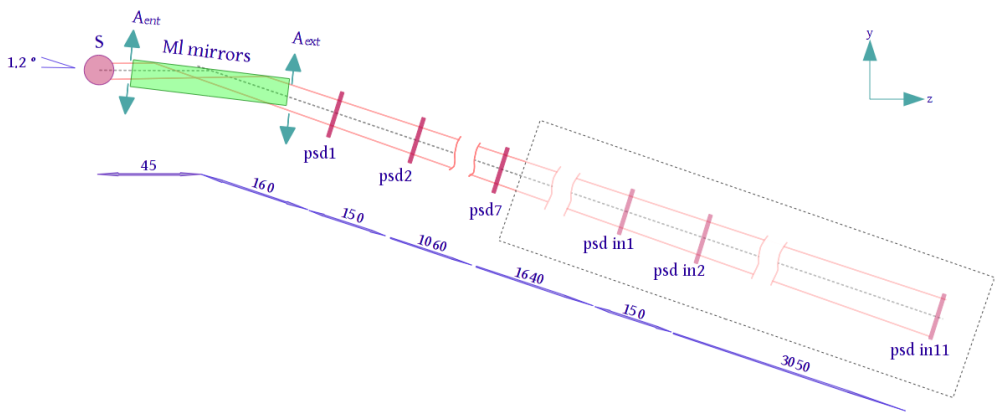

Figure 4.12: Schematic of the simulation layout: source S, entry and exit apertures A_{ent} and A_{ext} respectively, multilayer mirrors Ml and detectors psd. The distances are given in mm.

corresponded to 45 mm away from the source. The placement of the mirrors wasn't trivial, therefore auxiliary components, arms [37], were used to rotate the instrument's propagation axis around two other axes.

Fig. 4.13 illustrates the gradual rotations.

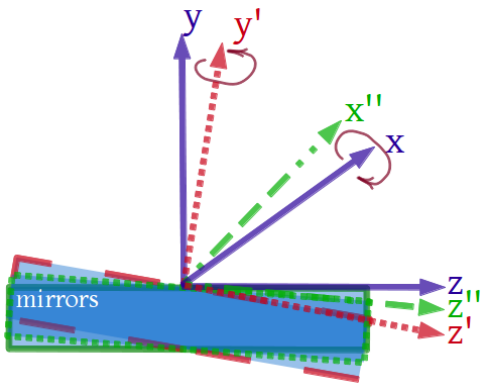

Figure 4.13: Illustration of the mirrors' rotation: (x, y, z) - initial axes, (x, y', z') - intermediate rotation and (x", y', z") - final rotations.

Firstly, one arm x, y, z marked in blue in fig. 4.13 designated the reference point, i.e. centre of the mirrors. Secondly, to lift the front side of the mirrors towards the source a new arm x', y', z' appeared after rotating the first arm around x axis by -1.2° (marked with red finely dashed pointers). Finally, to reconstruct the experimental angle of incidence a third arm was introduced into the model x", y", z" (shown in green colour with coarse dash arrows) by rotating the second arm around y axis by 1.2°.

Each individual multilayer consists of alternating bilayers, which are grown by depositing one material on top of another in a respective sequence as illustrated in fig. 4.14.

The multilayer mirrors are defined in one extended component *TwinKB_ML*. This component is based on the side-by-side geometry of the two mirrors, it calculates intersections of the photon rays with the surfaces, the number of bounces on the surfaces, reflecting and propagating the photons further. Placed perpendicularly to one another, the combination of two elliptical surfaces is focusing the beam at 900 mm from the centre of the system (the focal length parameter).

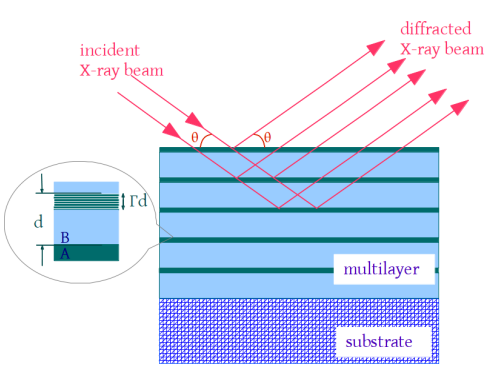

Figure 4.14: Schematic of the multilayer principles. The drawing is reproduced from the one in [38].

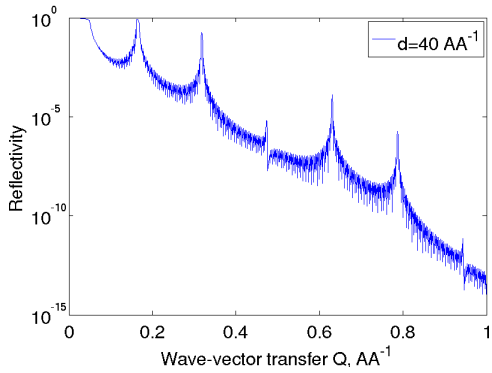

Figure 4.15: The reflectivity curve of the simulated multilayer with 40 Å d-spacing.

The reflectivity of the multilayers was calculated in Matlab and exported to McXtrace as a datafile. This calculation was done according to the algorithm implemented previously by Annette Vickery[4]. The kinematic approximation is considered, where multiple reflections and refractions are assumed to be small.

The multilayer consists of a number N of bilayers of thickness d (fig. 4.14). The electron densities of the materials that constitute the bilayer differ greatly. To calculate the reflectivity of the whole multilayer, it is convenient to decompose its structure into a sum of single bilayers. The reflectivity of a single bilayer is determined through

$$r_1(Q) = \frac{r_0 \rho_{AB}}{\sin\theta} \cdot \frac{\lambda}{i} \int_{-\Gamma d/2}^{\Gamma d/2} e^{iQz} \mathrm{d}z, \tag{4.1}$$

where r_0 is the scattering amplitude of an electron, i.e. Thomson scattering length, ρ_{AB} is the electron density contrast, θ is the angle of incidence, $1/i$ expresses the phase shift π of the scattered photon rays, Γ is the high density material fraction of the bilayer, $Q = 2k\sin\theta$ is the wave-vector transfer and e^{iQz} is the phase difference between rays reflected at different depths z in the bilayer.

[4] A thorough description of the physics of multilayers along with a reflectivity calculation is provided in [9].

Afterwards, the reflectivity of the entire multilayer was calculated according to

$$r_N(Q) = \sum_{\nu=0}^{N-1} r_1(Q) e^{iQ\nu d} e^{-\nu\beta}$$
$$= r_1(Q) \frac{1 - e^{iQNd} e^{-N\beta}}{1 - e^{iQd} e^{-\beta}}, \tag{4.2}$$

where $e^{iQ\nu d}$ is the phase difference and $e^{-\nu\beta}$ is the absorption. The weighted average of the absorption β is then

$$\beta = \frac{2d}{\sin\theta}(\mu_A \Gamma/2 + \mu_B(1-\Gamma)/2), \tag{4.3}$$

where the first factor is the total path length of the incident and reflected beam. The absorption coefficient μ refers to intensity, whilst the amplitude is $\mu/2$. The intensity reflectivity was calculated as the absolute square of the amplitude reflectivity. A reflectivity curve determined for the average d-spacing of 40 Å is shown in fig. 4.15.

The multilayer used in the SAXS instrument had a variation of bilayer thicknesses along z axis, as illustrated in fig. 4.16.

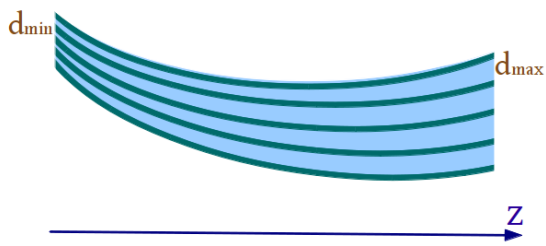

Figure 4.16: Schematic of the multilayer with alternating d-spacing.

The exact characteristics of the multilayer were unavailable, therefore a correlation between the bilayer thicknesses and lengthwise coordinates was calculated in Matlab according to set parameters (source - object S_1, object - image S_2 distances, d-spacing in the centre of the multilayer and the main photon energy E=8.048 keV) and ported to McXtrace as a separate datafile. Fig. 4.17 illustrates the range of d-spacings (from 24 Å to 50 Å), whereas fig. 4.18 shows the appropriate angles of incidence correlated with particular d-spacings to fulfill a monochromatisation of the incoming beam according to the Bragg law. A few reflectivity curves corresponding to the relevant bilayer thicknesses are shown in fig. 4.19.

The apertures surrounding the mirror system are square with a side length of 1.5 mm. According to the description of the instrument, the apertures were mounted to the mirrors.

Overall, there were seventeen monitors *psd_detector* in the setup, the distances between which are depicted in fig. 4.12. The size of one such monitor is 619 × 487 pixels (corresponding to 106 × 84 mm^2) in the horizontal and vertical directions respectively. The numbers above were taken from the technical specification provided by the detector's manufacturing company.

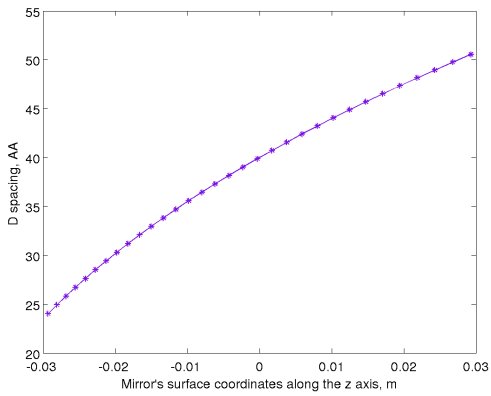

Figure 4.17: Correlation between the lengthwise coordinates of the multilayer surface and its d-spacings.

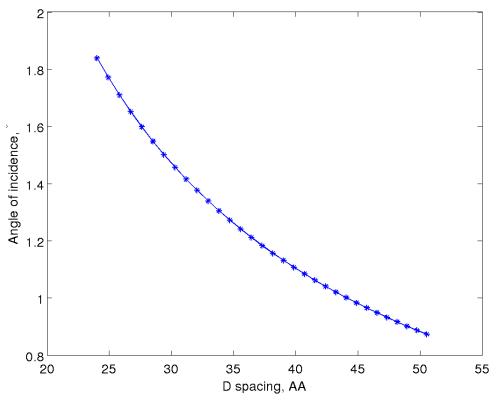

Figure 4.18: Calculated dependency of the angles of incidence and d-spacings to monochromatise the beam.

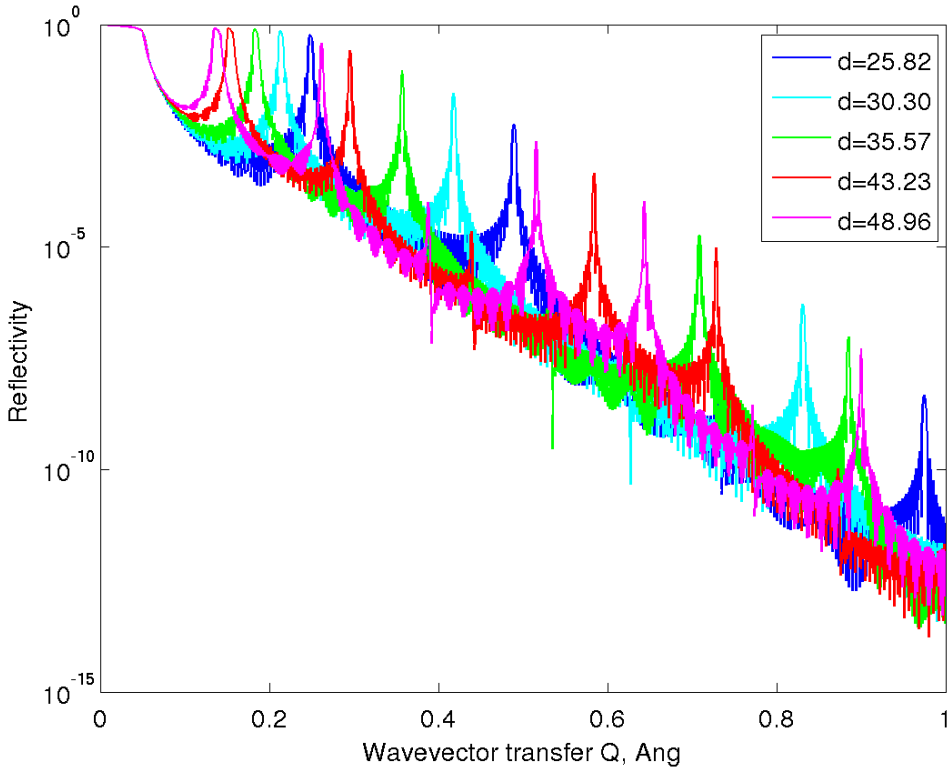

Figure 4.19: Reflectivity of the multilayer with various d-spacings.

4.5 Experimental versus simulated images

The initial X-ray beam, after its interaction with the mirrors system, produces four distinct spots corresponding to different mirror reflections and a fraction of the unchanged direct beam. This square pattern is illustrated in fig. 4.20: the

upper spot is the fraction of the direct beam, the two side spots are the singly reflected beams (those that hit either of the mirrors just once) and the most important lowest spot - the doubly reflected beam. It is the doubly reflected beam that is used experimentally, whilst the rest of the beams are filtered out by a set of collimating slits.

To compare the experimental images with the simulated ones the distance between the outer edges of the singly reflected beams is examined according to the white line shown in fig. 4.20. Both of the graphs are presented on their own absolute logarithmic scales.

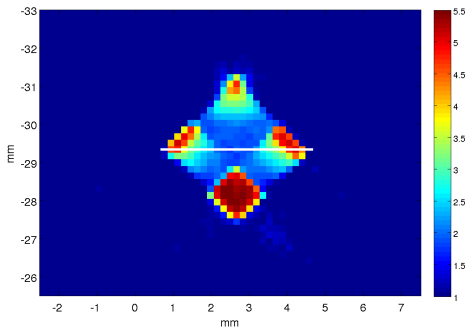

Figure 4.20: The experimental image at the first position of the detector, i.e. the closest to the source block.

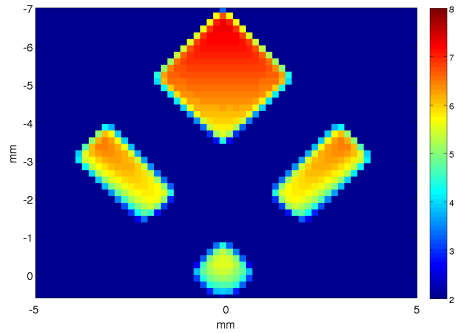

Figure 4.21: The simulated image corresponding to the first position of the detector nearest the source block.

Fig. 4.20 and 4.21 illustrate the first data set. The dimensions of the two images are the same, therefore the size of the square formed by all the beams is compared at once. The experimental data reveals 3.44 mm against 6.85 mm, which is the simulated distance. The shape and size of the doubly reflected (DR) beam, on the other hand, is identical on both images.

The next two images for analysis are presented in fig. 4.22 and 4.23. The fraction of the direct beam is much larger in the simulated image than that from the experiment. In fact, it seems as the direct beam entirely, rather than just a fraction of it; the singly reflected (SR) experimental beams of the drop-like shape are reproduced in simulation, though with more pronounced boundaries. The experimental DR beam has maximum intensity and its shape is similar to that of the simulated image. The main criterion for the comparison (the SR distance) continues to be significantly larger in case of the simulated image: 14.04 mm versus the experimental 8.43 mm.

The demonstrated above results are rather ambiguous. Even though the general tendency of the square pattern repeats well in simulation, the difference in dimensions (that is of the order of 50%) is not satisfactory. Instead of presenting the rest of the simulation images and noting the larger and larger deviations, the spaces between the two singular reflections are summerised in fig. 4.24. The difference between the spread of the two data sets is noticeable from the very beginning, and it continues growing throughout the setup, which

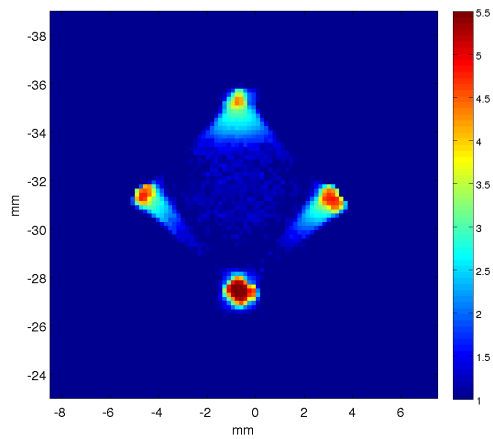

Figure 4.22: The experimental image at the second detector position, 30 cm.

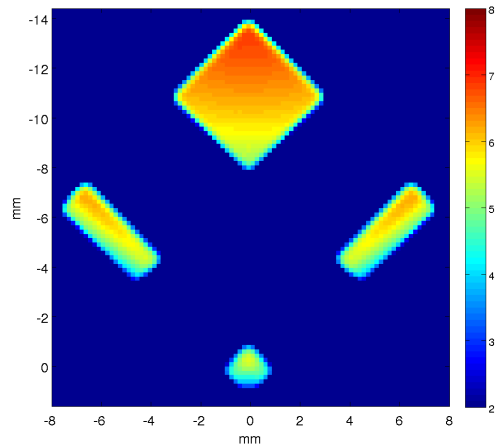

Figure 4.23: The simulated image at the second detector position, 30 cm.

clearly indicates that the simulation does not represent the experimental result correctly.

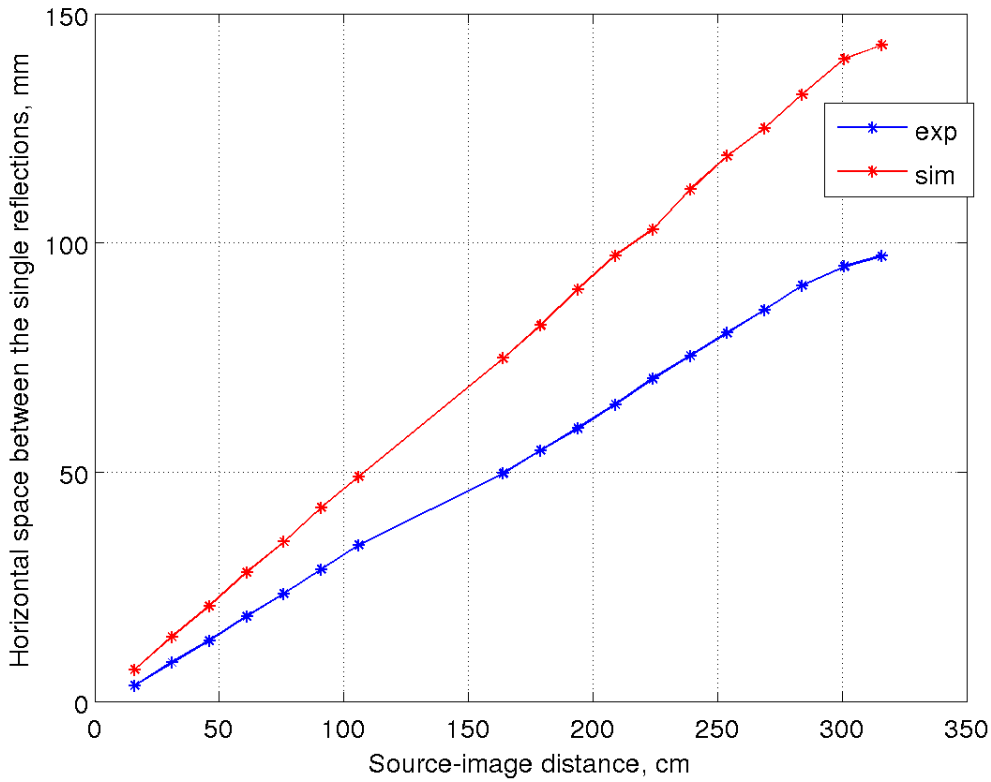

Figure 4.24: The comparisons of distances between the singular reflection spots of the experimental data versus those of the simulation.

There could possibly be two major explanations of the dissimilarity: firstly, the mathematical model (i.e. computer code) is faulty and secondly, the geometry of the setup as we know it could be incorrect. The correctness of some aspects of the geometrical setup is rather difficult to confirm, since the access to the machine is limited, moreover the particular area of interest (the geometry of the source block) is unavailable for unmounting and inspecting. The rightness of the mathematical model, on the contrary, is easy to test; the description of a setup for such a test and further conclusions are presented in the following section.

4.5.1 Test of the TwinKB_ML component

Therefore the photons incident at other angles will also be reflected, but their impact will be negligible.

A colleague of mine, Jesper Jensen, also working on the SAXS simulation spent a great deal of time checking the model mathematically by calculating every single step manually and then comparing the outcomes with those produced by the code. He found no errors, which led us to the assumption that the theory was represented well in the simulation.

Another way to test the correctness of the instrument model is to test its main component, the multilayer mirrors system, separately. Generally, at every step of development of new components for the McXtrace package there are numerous checks and tests, therefore the multilayer mirror component has been thoroughly tested before its release and further use inside other instruments. However, specifically for modelling of the SAXS experiment, two separate multilayer mirrors were extended into a single component, referred to as *TwinKB_ML*, which is a subject of the current test.

In the SAXS instrument the multilayer system has two functions: it focuses the beam due to the elliptic curvature, and it monochromatises the beam according to the Bragg law in the manner of a diffraction grating. Both of the functions can be tested at once to check how the *TwinKB_ML* mirrors represent its physical counterpart.

The schematic of the setup for the *TwinKB_ML* test is illustrated in fig. 4.25. The source parameters were different to those used for the initial simulation: a *Source_gaussian* with RMS 50 µm in both directions was used for this test, the beam's divergence was set to 10 mrad[5]. The mirrors were set at the exact same angle of incidence relative to the source as the one used for the main simulation, whereas the source - object S_1 and object - image S_2 distances were set to 10 m each to make it a 1:1 focusing scheme. Two additional monitors were set into the layout to follow the spatial dynamics of the beam: 2 m prior the focusing plane, det_1, and 2 m after it, det_2. Two energy monitors energy_bef and energy_aft were placed into the setup as well to check the monochromatisation.

The results of the test are presented in the same figure with the setup (fig. 4.25). det_0 monitor shows the initial beam right at the source plane, which is split into four spots after its interaction with the mirror system. The subsequent monitors in the focusing scheme are aligned to capture only the doubly reflected beam, therefore det_1 and det_2 reveal its divergence when

[5]Such a divergence is extraordinarily high, but it nonetheless was useful for the test.

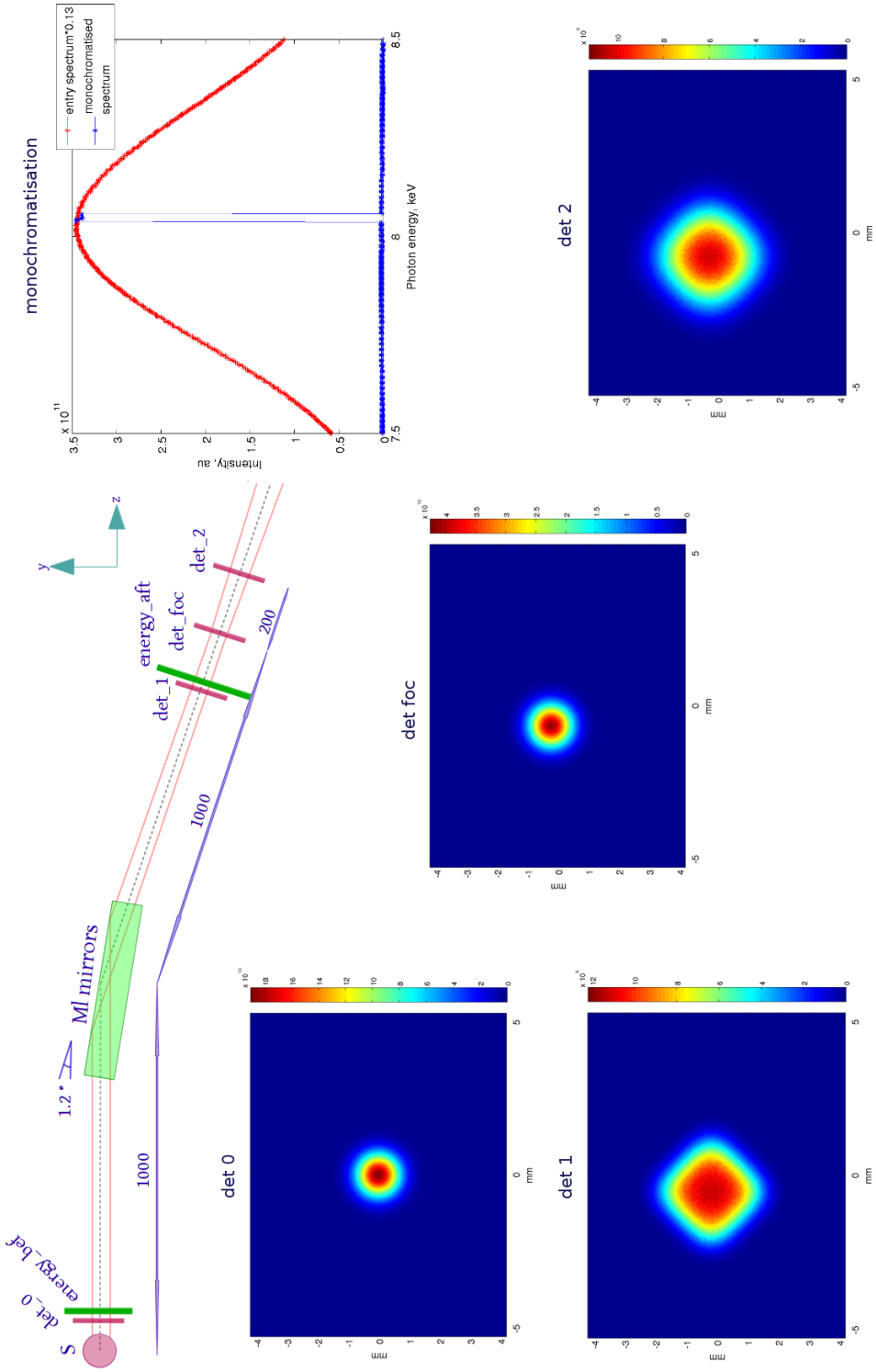

Figure 4.25: The setup for the *TwinKB_ML* test at 1:1 focusing geometry, distances are given in cm.

approaching and departing the focusing plane. det_foc shows the image of the doubly reflected beam at the focal plane: its shape and size are identical to those of the initial beam, which is a good indication of a correct focusing property of the multilayer system. The monochromatisation of the incoming beam is illustrated in the lower corner with a plot depicting an entry spectrum before the mirrors captured by an energy sensitive monitor energy_bef and the one after the multilayers, energy_aft. The latter monitor was positioned and sized in such a way, so it could monitor the energy of the doubly reflected beam only, therefore any influence of the remaining constituents of the beam (singly reflected beams and a direct one) was eliminated. On the graph, the Gaussian profile of the incoming spectrum was lowered in intensity in order to match the maximum value of the monochromatised one (the compliance coefficient is 0.13). Thereby it shows a very good monochromatisation of the initial beam, and proves the second multilayer function to work just as well.

4.5.2 Discussion of the possible discrepancy origin

A closer analysis of the simulated image reveals some interesting aspects: it looks as if the simulated image shows an extended version of the experimental result. Having connected all the reflections and the fraction of the direct beam with straight lines and transferring this square into the simulated image, the two images start resembling one another better than previously (fig. 4.26 and 4.27).

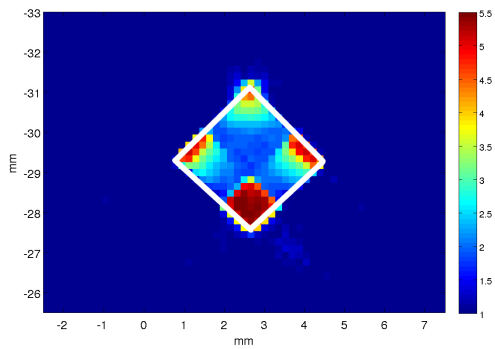

Figure 4.26: The square formed by the edges of four experimental beams.

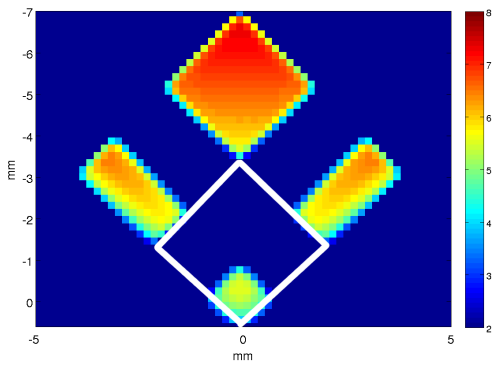

Figure 4.27: The experimental square transferred to the simulated image.

The DR beam is of the same size on both images and the horizontal dimensions of the SR beams are the same as well. This shows that the simulation does reproduce the experiment, but on a larger scale. In such a case, the dissimilarities between the two data sets could be explained by the lack of knowledge of the geometrical nuances in the setup. After all, the SAXS instrument is a commercial product, the technical specifications of which are proprietary, so there can always be a degree of uncertainty with respect to precise dimensions.

The previously mentioned facts sparked an idea to try running simulations with other parameters, slightly different to those stated in the description of

the instrument, namely, the entry and exit slit positions relative to the mirrors system. After all, slits collimate the size of the beam, therefore their placement must play an important role in the dimensions of the reflected beam. At first, when the exit slit was moved lower than its initial location, the DR beam stayed the same in size and intensity, whereas the SR one had longer tails and appeared closer to the DR; the direct beam was more scattered resembling more that of the experimental images. The lowering down of the exit slit continued until a moment when the beam was entirely gone, as the slit shaded all the reflections. Therefore the entry slit was moved upwards to let more flux onto the mirrors until all four reflections were placed as previously. Thereby an optimal location for both of the slits was configured. The new locations of the slits are depicted in fig. 4.28: the entry slit was shifted upwards by 0.6 mm, whilst the exit slit was moved downwards by 3.17 mm.

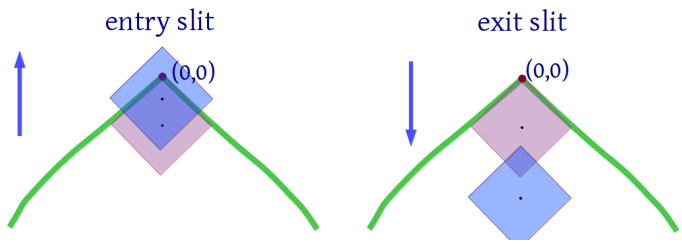

Figure 4.28: The tweaking of the entry and exit slits relative to the mirrors.

The liberty of adjusting the simulations according to the principle described above brought good results. Fig. 4.29 illustrates a much better correlation between the adjusted simulation (sim*) and experiment (exp). Since the goal of the SAXS project was to reproduce the experimental data as close as possible, the adjusted simulation was chosen for that purpose.

4.5.3 Results of the adjusted simulations: "outside of the vacuum chamber" mode

The images of the beam along the propagation axis are somewhat the same, therefore instead of presenting images from every step of the detector movement, two pictures from each mode were chosen. The first and the last detector positions of the "outside of the vacuum chamber" mode are illustrated in fig. 4.30. The experimental data was plotted on a logarithmic scale, which was consistent for all images; the simulation data was also plotted on a logarithmic scale, which varied throughout the images (the necessity of changing the scale was caused by a falling intensity of the reflected beams towards the end of the instrument).

A closer look at the images of the first position reveals that the distance between the SR beams is slightly longer in the simulation than that in the experiment (by 39%) - much better agreement than during the initial simulation. That is explained by the new positions of the slits, which brought all reflections closer to each other, hence diminished the compared distance. The down side of the new slits' positions is also noticeable - the simulated DR beam has

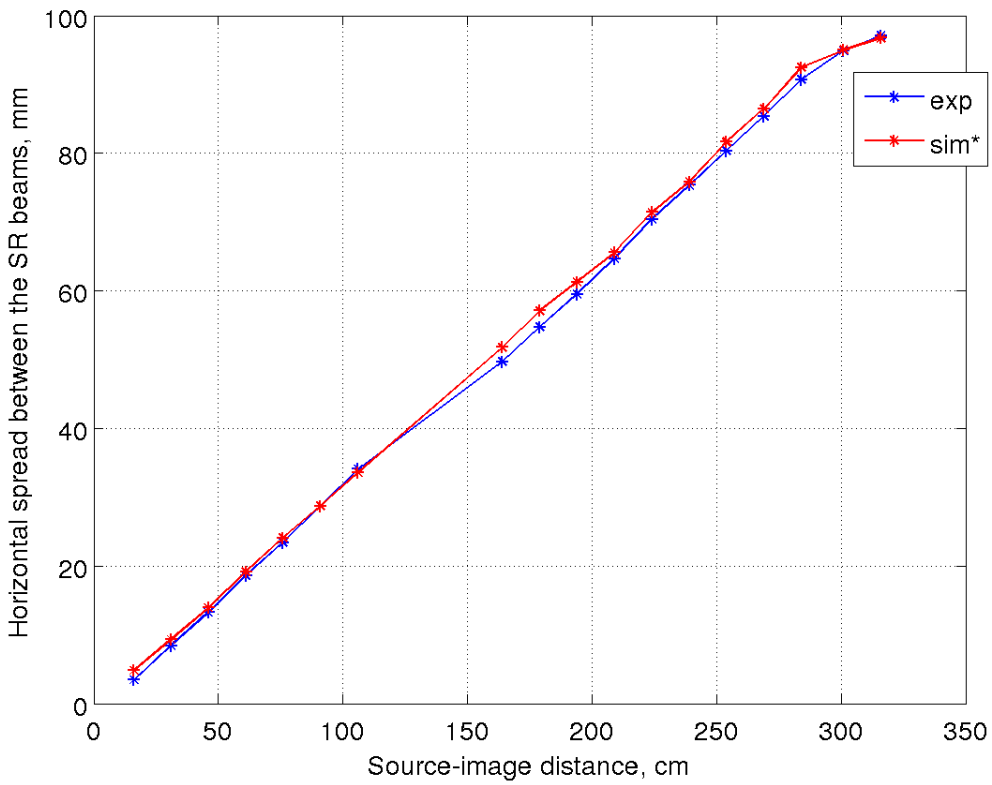

Figure 4.29: Comparison of the experimental and adjusted simulation results.

much smaller dimensions than the experimental and the previously simulated ones (fig4.21). The same effect appeared on the SR beams as well: horizontally elongated lines turned into rather round spots.

The seventh detector position (the last one before the chamber) reveals much better agreement between the experimental and simulated images - the distance between the SR spots is only 1% different. Since during the experiment the Pilatus detector was moved manually and it was primarily targeted for catching the DR beam, the fraction of the direct beam is absent in the experimental image, whilst it is still present in the simulated one. The simulated SR beams have grown into drops-like spots, whilst the experimental SR beams have turned into comets with significant tails. A possible explanation for this widening of the simulated SR beams whilst their experimental counterparts were getting longer, perhaps, still lies in the absence of additional scattering (which would be there, had the slits been turned back to their original placement).

The DR spots in both images have the same dimensions. The simulated DR is circular and symmetric, whereas the experimental DR beam is square with sharp elongated edges (caused by the SR tails).

4.5.4 "Inside the vacuum chamber" mode

This mode is presented by data from the sixth and eleventh detector positions inside the vacuum chamber: the sixth position corresponds to the detector's

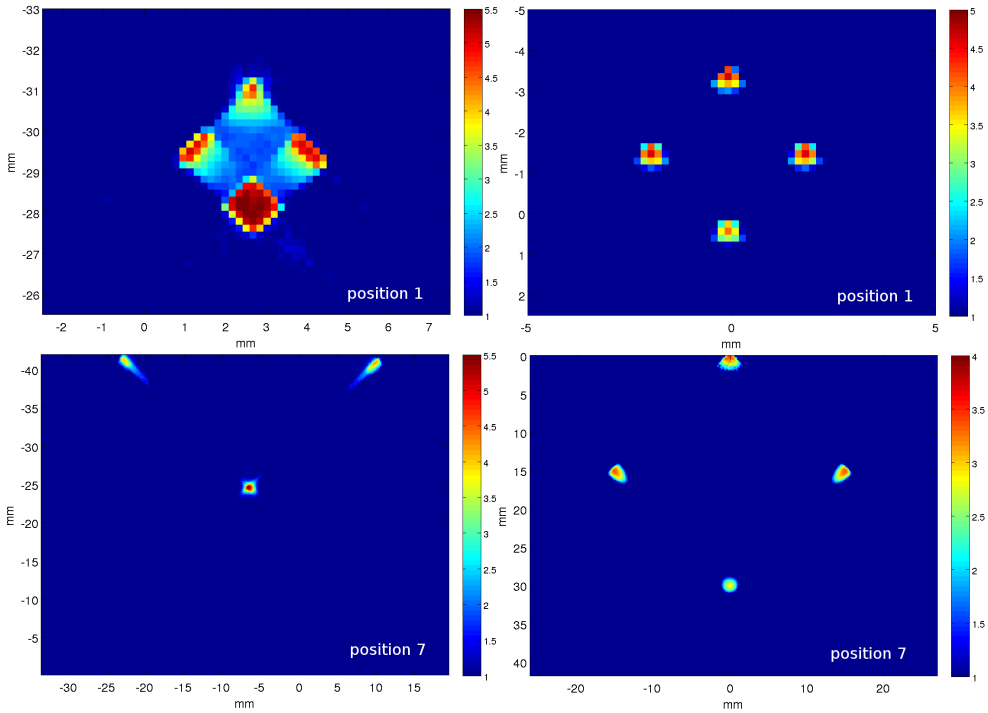

Figure 4.30: The comparison images of the experimental (left) and simulated (right) data at the first and seventh detector positions, 16 cm and 106 cm subsequently.

placement approximately in the middle of the chamber and the eleventh position is the detector's maximum distance away from the source.

As the Pilatus moved further away from the source, the shape of the SR beams became more asymmetric on the experimental data. It became particularly distinct in fig. 4.31 (top left): the comet-like tail of the right SR beam is longer than the left one. This could possibly be ascribed to the KB multilayers' slight misalignment on the day of the experiment. The asymmetry of the SR spots affected the shape of the DR beam: as the right SR spot is slightly larger than the left one, the DR beam appeared stretched out towards the right. The simulated image, on the other hand, shows good symmetry, hence the DR beam appears round.

The horizontal distances between the SR beams on both data sets correspond to one another, which is shown in numbers in fig. 4.29. The last detector's position reveals that the experimental SR beams remain thinner and even more asymmetric when compared to their simulated counterparts, which is not a new effect, but rather a continuous and consistent divergence of the SR spots.

Comparing the four beams' intensities at all detector positions, it becomes evident that in simulations the direct beam was always the most intensive one (when it was still visible in monitors), the SR spots had lower intensities and the DR beam was the least intensive one. The logic behind it is the following: the direct beam collimated by the entry slit passes through the mirrors system without any interaction with it, hence its intensity stays unchanged; the SR

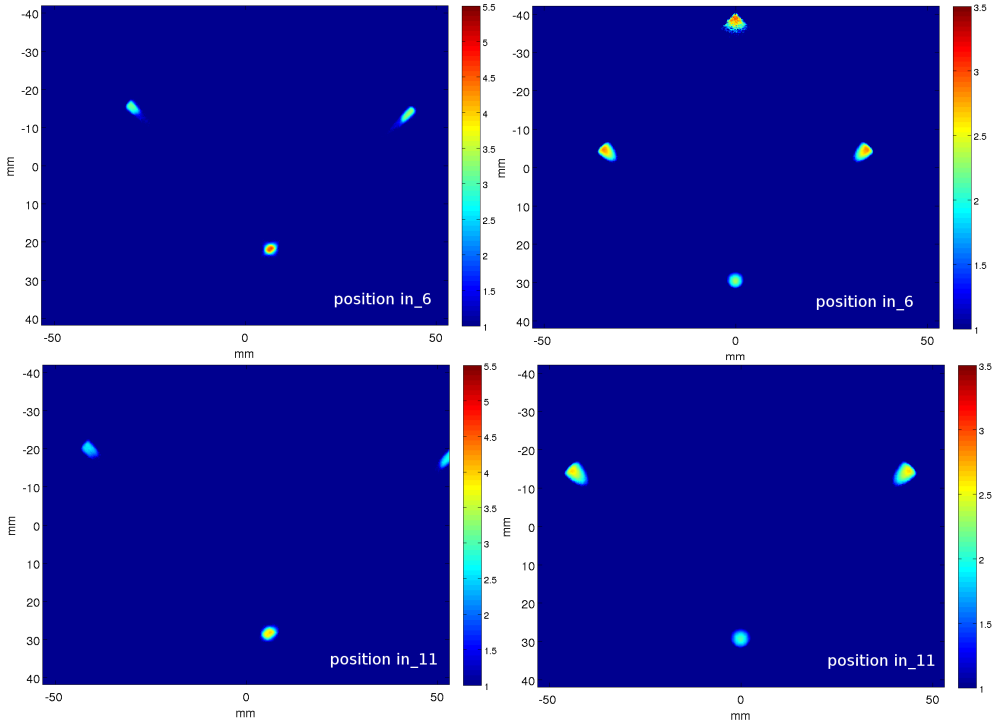

Figure 4.31: The comparison images of the experimental (left) and simulated (right) data at the sixth and eleventh detector positions inside the chamber, 239 cm and 316 cm away from the source respectively.

beams hit either of the mirrors once, their intensities are multiplied by the reflectivity factor only once and their resulting intensity falls; the DR beam is formed by the photons hitting the mirrors system twice, therefore their final intensity is multiplied by the reflectivity twice, therefore it appears the weakest. In the experimental data, on the other hand, the most intensity was always concentrated in the DR beam. A possible explanation for this lies in calibration of the KB mirrors before the experiment: the system is manually aligned in such a way to redistribute the maximum intensity towards the DR spot.

4.5.5 Comparison of the DR beam dimensions

As the DR beam is the main one for practical experiments, it is of interest to follow its progression along the propagation axis in both experimental and simulated data. The horizontal and vertical dimensions of it from both data sets are superimposed on one plot and illustrated in fig. 4.32 and 4.33.

Firstly, it should be mentioned, that the comparison plots present only approximate values for the DR dimensions and are shown only to illustrate the common tendencies of growth of the DR spots. As the spots were so small, the sizes were estimated by selected pixels. So the size estimates are prone to large uncertainties.

The initial DR sizes of the experimental and simulated beams were 36% and 43% different in the horizontal and vertical directions respectively. (Fig.

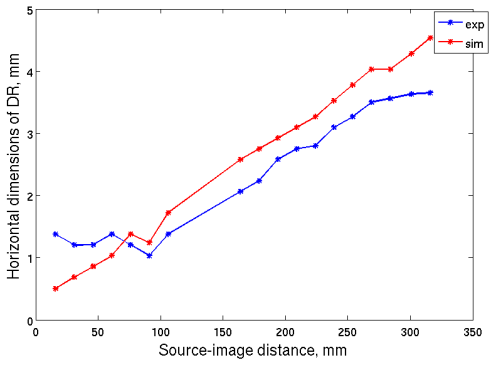

Figure 4.32: The comparison between the DR beam from the experimental and simulated data in the horizontal direction.

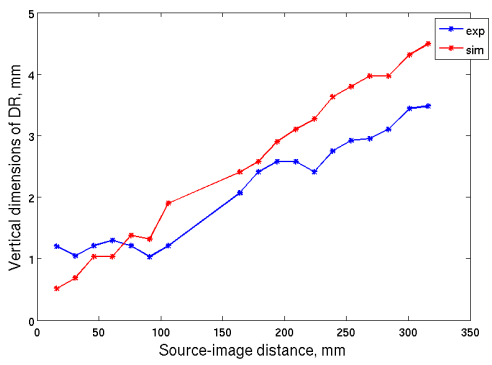

Figure 4.33: The comparison between the DR beam from the experimental and simulated data in the vertical direction.

4.30 illustrates the initial DR spots.) The cause for it was in the new positions of the collimating slits surrounding the mirrors. As the reflected DR beams propagated further along the axis, their sizes slowly converged towards one another at the focal plane, where they reached 12.6% and 20% difference in the respective directions (horizontal and vertical). Afterwards the two DR spots maintained their 13-16% difference towards the end of the instrument. The horizontal dimensions of the two DR beams are more monotonous, whilst the vertical sizes are more inconsistent. Fig. 4.34 illustrates the DR spots at the mirrors focal plane (corresponding to the detector's sixth position outside the vacuum chamber) and at the detector's maximum position.

The shape of the experimental DR spot (top left image) is square with stretched edges, the simulated DR spot is circular. The area of the most intensity in both spots has approximately the same dimensions. The shape of the experimental DR spot (bottom left image) towards the end of the instrument lost its square symmetry and is stretched out towards the right. The simulated spot, on the contrary, stayed symmetric.

4.6 Discussions and conclusions

The chapter described in full detail the simulation of the X-ray beam propagation inside the SAXS instrument. Firstly, a model of the apparatus was made in the McXtrace programme according to the technical description provided by SAXSLAB ApS that assembled and installed the instrument. The simulation results after the first runs of the model did show the general tendencies observed in the experimental images, however, they did not restore the same distances between the beams, which was an important comparison criterion. Besides, the discrepancies grew consistently, and started off already at 50% (fig. 4.24).

With a great help of Jesper B. Jensen the theoretical model used for the simulation was thoroughly checked by manual calculations with no evident er-

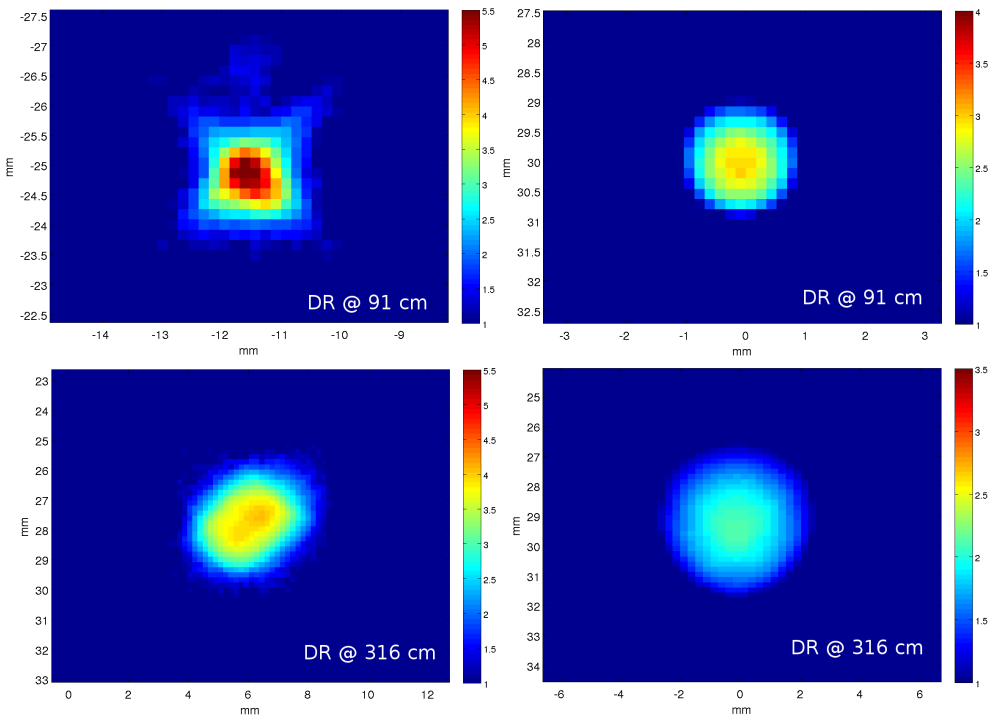

Figure 4.34: The comparison images of the experimental (left) and simulated (right) DR spots at the mirrors' focal plane and the detector's furthers positions inside the chamber, 91 cm and 316 cm away from the source respectively.

rors. Another test of the mirrors component was performed, which proved its adequate representation of the realistic mirrors. A possible explanation was found for the initial discrepancies that involved the location of the collimating slits surrounding the mirrors system, due to the lack of knowledge of the precise geometry of the source block of the apparatus, which contained the mirrors, as the instrument was a commercial product and the manufacturer of the source would not volunteer specifications.

As it turned out, with the use of slightly altered geometrical parameters (that are given in table 4.1) the simulation resulted in nearly the same pattern as the experiment.

Table 4.1: The initial (init) and adjusted (adj) position of the slits along the y axis in the simulation.

parameter	init	adj
entry slit	-1 mm	0.6 mm
exit slit	-1.12 mm	-3.17 mm

The aim of the SAXS project was to reconstruct the beam's propagation in McXtrace. This was fulfilled under the new conditions. The main criterion of comparison was the horizontal distance between the two single reflections. The values of the adjusted simulation matched those of the experiment much closer than the initial model. The comparison of the doubly reflected spots from

the experimental and simulated data showed less agreement than the main criterion. It could partly be explained by the tiny dimensions of those spots - of the order of several mm at its best - therefore any slight deviations would already introduce big discrepancies (of the order of 15%). It could as well be explained by contributions of the singly reflected beams to the shape of the doubly reflected ones: the asymmetric experimental spots provided the DR spot's slight stretching towards the right, whilst the simulated ones were symmetric, hence caused no effects on the DR beam.

Chapter 5

Modelling of a transfocator

This chapter describes the results of a collaborative work under the supervision of Dr. Oleg Chubar, an instrumentation scientist at Brookhaven National Laboratory, on simulations of a transfocator, an X-ray focusing device. The experiment was performed at the ID11 beamline at the European Synchrotron Radiation Facility (ESRF) and described in detail in [39]. Most of the essential parameters needed for simulations were taken from the corresponding article. The modelling of the experiment was done in a complementary fashion with the use of two techniques: ray-tracing (presented by McXtrace) and wave optical propagation (realised in the SRW code). Firstly, the McXtrace simulation was benchmarked with the data from SRW. Secondly, both results were compared to the experiment. The utilisation of the two techniques for solving the same problem brought new ideas in further development of McXtrace. The results of this work were presented on the SPIE Optics and Photonics conference in San Diego, USA in August 2011.

5.1 The transfocator device

The technological advances in X-ray optics allowed development of different types of X-ray lenses. They are relatively easy to align and operate (insert and retract) in the beamline and less sensitive to angular disturbances of the incoming beam than other focusing elements. As the refractive index depends on X-ray energy, the X-ray lenses are chromatic, which, in turn, reduces their applicability. Therefore there appeared a need for energy-tunable optical systems where the X-ray energy could be tuned without changing the beam's position or the sample.

A transfocator is an array of compound refractive lenses (CRL) aligned in parallel [40], [41]. It was designed and installed at the ID11 beamline at the ESRF. The initial concept of the device is presented in fig. 5.1: the aluminium CRLs are set in a geometric progression with a step of 2, allowing between 2 and 254 lenses. The number of lenses varies in accordance with a working energy. The individual lenses are made from polycrystalline aluminium by a pressing technique. The paraboloids are held and centred in a brass frame.

The successful use of the IAT at the beamline for nearly four years has led to further modifications and a new interpretation of its concept, as an "in-vacuum

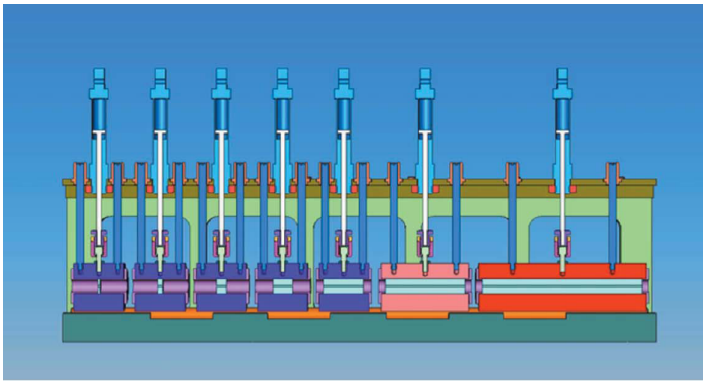

Figure 5.1: Schematic illustrating the concept of the IAT. The principle of the IVT is similar to that of the IAT, although the chamber is significantly larger due to more complex engineering decisions accounting for a vacuum translation of the cartridges and water cooling. The picture is taken from [39].

transfocator" or IVT. In this type of a transfocator the lenses are arranged in pneumatically activated cartridges containing between 1 to 63 beryllium and 32 to 96 aluminium lenses. The beryllium paraboloids are held and centred in a kovar frame. The design allows for permanent energy and focal length tunability. The IVT unlike the IAT is water-cooled, therefore it is allowed to use in a white beam.

The applications of an IVT are as follows: as a standalone focusing device in a monochromatic beam, as pre-focusing optics in conjunction with micro- and nanofocusing elements to obtain a huge flux gain and finally as a longitudinally dispersive monochromator. The latter was chosen for the modelling project in compliance with the experiment [39].

The beam of the undulator source at the ID11 beamline has a very broad energy spectrum. The X-rays of different energies are focused at different distances due to the dispersive nature of focusing. In order to obtain a degree of monochromaticity of the beam, a narrow slit is placed at a certain distance from the transfocator, which lets through primarily X-rays of the energy that is focused at that point. Approximately half of the photons of other energies constituting the beam are blocked by the slit. The partly monochromatic energy that is passed through the slit is varied not by adjusting the slit position, but by altering the relative proportions of beryllium and aluminium lenses in the transfocator. The study of the degree of monochromatisation as a function of the pinhole's width is the subject of the modelling experiment.

5.2 Geometrical setup of the simulated experiment

The geometric layout of the simulation model is illustrated in fig. 5.2[1].

[1]The experiment described in [39] focused on the use of the transfocator as a so-called low-tech monochromator, the idea of which is central for this simulation. The experimental method of focusing the white beam with an IVT is exploited in the simulations as well. The contents of the IVT are different for the two cases though: a total of 48 beryllium lenses were

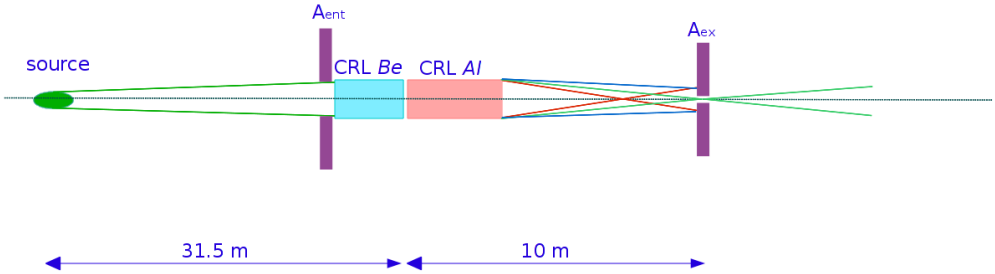

Figure 5.2: Schematic of the model of the longitudinally dispersive monochromator based on beryllium (blue) and aluminium (coral) CRLs.

Table 5.1: Parameters of the photon beam.

direction	RMS	divergence
horizontal	48.2 µmu	100 µrad
vertical	9.5 µm	4.3 µrad

The X-ray beam, parameters of which are given in table 5.1, was collimated by a circular entry aperture, A_{ent}, 1 mm in diameter. It was positioned approximately 31.5 m downstream of the source and preceded the main component of the setup, the transfocator, which had compound refractive lenses of two materials, beryllium and aluminium. The number of lenses in the transfocator was calculated according to

$$\frac{1}{S_1} + \frac{1}{S_2} = \frac{1.568 \cdot N_{Al} + N_{Be}}{0.296 \cdot E^2}, \tag{5.1}$$

where S_1 and S_2 are the object and image distances, respectively, N_{Al} and N_{Be} are the numbers of aluminium and beryllium lenses, respectively, and E is the photon energy [39]. Right after the aperture were 16 beryllium lenses followed by 21 aluminium lenses. This combination of lenses[2] focused the photons of 35.61 keV at 10 m.

The profiles of the CRLs were paraboloids of rotation (fig. 2.2) [42], hence focusing was achieved in two dimensions. The CRL's parameters were identical for both beryllium and aluminium lenses: the radius of curvature at the tip of the parabola was 0.2 mm, the lens' geometric aperture in both vertical

used experimentally, whilst in simulations a combination of 16 beryllium and 21 aluminium lenses was employed. In principle, it made almost no difference for the main purpose of the experiment - either way the white beam of specific energy was focused at a specific location. In practice, the combination of beryllium and aluminium lenses is used primarily to focus hard X-ray radiation (the photon energy from 70 keV and higher up to 140 keV) at 94 m distance. Focusing the X-rays of 35.61 keV was done at a 10 m distance, therefore there wasn't a necessity of utilising both beryllium and aluminium CRLs. During preparation of the simulations the exact number of lenses in the experiment was not available, so the setup was chosen to give the correct focal length for the primary energy.

[2]The insertion of S_1 and S_2 distances and the primary photon energy into eq. 5.1 resulted in $1.568 \cdot N_{Al} + N_{Be} = 49.43$. The number of beryllium lenses was chosen arbitrarily (as there were cartridges with 1, 2, 4, 8, 16 and 32 lenses), and it was set to 16. Therefore the number of aluminium lenses was calculated to be 21.

and horizontal directions was 1 mm, and the thickness between apices of the paraboloids were 50 µm for beryllium and 20 µm for aluminium lenses. The cutting-off pinhole, A_{ex}, was located 10 m away from the CRLs. During simulations there were three pinholes of 5, 10 and 20 µm used to determine the degree of monochromaticity.

5.2.1 Characteristics of the source radiation

When modelling any experiments performed at synchrotron radiation facilities, it becomes essential to obtain the most accurate representation of the initial photon beam. The various types of X-ray sources at synchrotrons have different characteristics, which determine their further interaction with the optical elements of the beamline.

The McXtrace code does not calculate a radiation source spectrum as this was beyond the scope of the development of the package. The synchrotron radiation workshop (SRW) code, on the other hand, consists of two parts: the first part is dedicated to calculation of a source spectrum, and the second is designed to propagate the calculated previously wavefront along a beamline that is being modelled. Therefore, the SRW code is used to calculate the precise characteristics of the undulator radiation of the ID11 beamline at ESRF.

Fig. 5.3 depicts the 3rd harmonic of the radiation from the U22 in-vacuum undulator. This harmonic is emitted off the electron beam axis; however, due to a finite electron beam emittance and a finite collection aperture, it is possible to obtain a considerable photon flux at this harmonic.

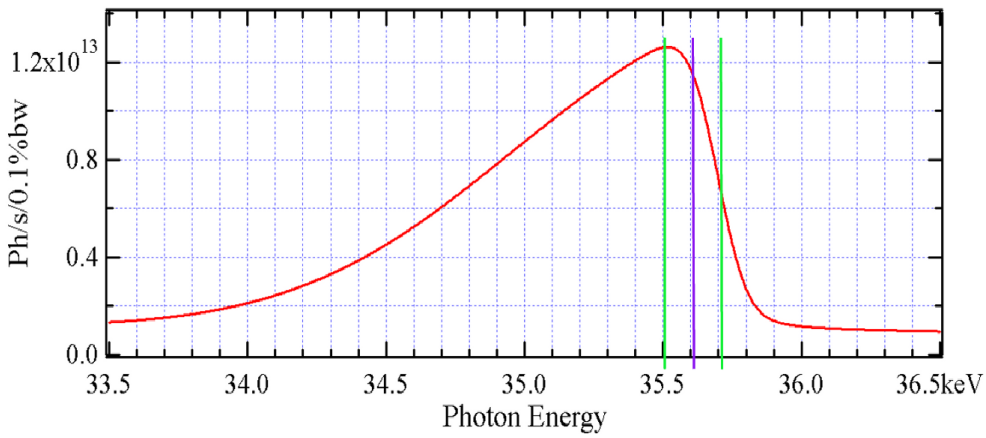

Figure 5.3: The calculated spectral flux at the entry aperture of the ID11 beamline at ESRF. The blue line shows the resonant energy 35.61 keV, green lines depict the two adjacent energies.

The primary energy for the virtual experiment was chosen to be 35.61 keV (in compliance with the experimental test of the transfocator), marked with a blue line in fig. 5.3; the maximum flux of the undulator spectrum was a little off the resonant energy, which is common in modelling of synchrotron radiation. Generally, depending on the choice of the photon energy within one harmonic,

the spectral flux collected by the fixed aperture varies, and the undulator radiation angular distributions corresponding to different photon energies may have slightly different profiles, particularly in the vertical direction, where the "averaging" effect of the electron beam emittance is smaller. Such profiles are reflected in fig. 5.4, with energies of 35.51 keV, 35.61 keV and 35.71 keV.

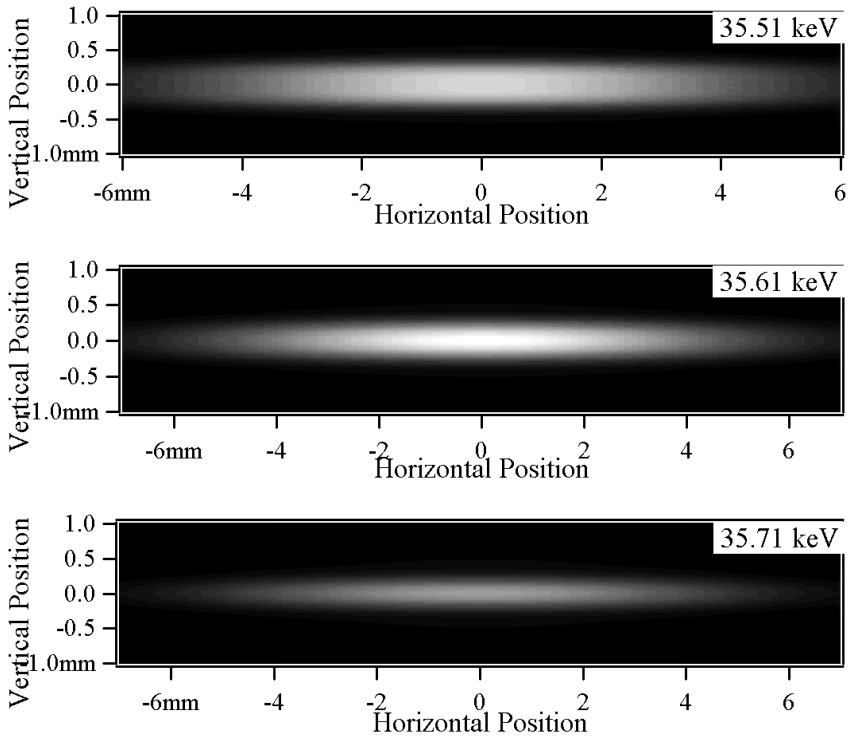

Figure 5.4: The spatial distribution of the beam's constituting energies. The primary energy 35.61 keV and two adjacent energies: 35.51 and 35.71 keV.

The experiment was modelled with a white beam, the bandwidth of which was chosen to be 1 keV, as this is the range of the undulator harmonic with the primary energy. The constituting energies of the interval, as some are shown in fig. 5.4, had various intensity distributions, therefore that had to be taken into consideration upon further analysis.

5.3 Numerical computation of the X-ray beam propagation through the IVT

The two techniques were used for the simulation of the experiment: McXtrace provided an input from the ray-tracing method and SRW completed the modelling with the wavefront propagation method[3] [43]. Ray-tracing offered high CPU efficiency, simplicity of simulation and provided good accuracy in cases of low X-ray coherence. The partially-coherent wavefront propagation method allowed an accurate description of X-ray beams at conditions of both low and high

[3]The McXtrace simulations and benchmarking between the data of the two packages were performed by the author of the present dissertation.

coherence, and enabled monitoring of the degree of coherence at the propagation through individual optical elements, at the expense of higher overall complexity and CPU-intensity of calculations. The combination of the ray-tracing simulation results of the device with partially-coherent wavefront propagation helped a wider understanding of a transfocator's functionality, thus it could open up possibilities for other beamlines to implement the device.

The virtual experiments were done in accordance with the setup illustrated in fig. 5.2 by McXtrace and SRW. The undulator spectrum was calculated by SRW and used later by both programmes. After completing the two separate simulations the results were primarily compared between each other and, to a minor extent, to the experimental result. The comparison analysis and subsequent conclusions were beneficial for further development of the McXtrace programme.

5.3.1 Ray-tracing

The source

In order to approximate the undulator radiation of the ID11 beamline, the *Source_gaussian* component was used, the algorithm of which contained two steps. Firstly, the photon beam was given a Gaussian distribution in the transverse plane[4]. The width of this Gaussian, σ_{eff}, depends on the widths of both the electron and photon beam widths, σ_{el} and σ_{ph} respectively, via $\sigma_{\text{eff}} = \sqrt{\sigma_{\text{el}}^2 + \sigma_{\text{ph}}^2}$. These RMS sizes in the horizontal and vertical directions were taken from previous simulations of the ID11 source by the SRW code, 48.2 µm × 9.5 µm respectively. The beam's divergences were also taken from previous SRW simulations, 100 µrad x 4.3 µrad in the respective directions. Secondly, the spectrum of the undulator was also calculated by SRW and stored as a datafile. The intensity distribution and the spectrum together provided the complete description of the source applicable for the ray-tracing method. The primary energy for the virtual experiment was 35.61 keV to match the resonant energy, which was a little offset from the peak flux of the ID11 beamline (fig. 5.3). The full width at half maximum of the corresponding harmonic is 1 keV, so the energy bandwidth, ΔE, of the simulation was also set 1 keV.

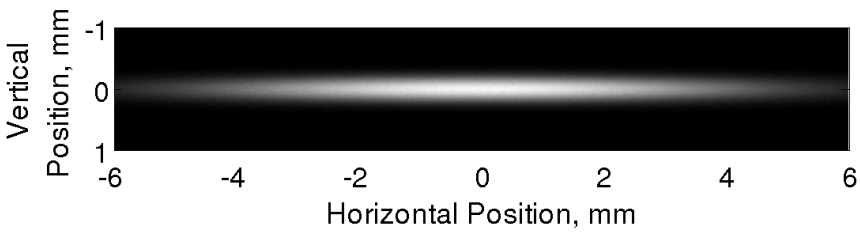

Figure 5.5: The spatial distribution of the undulator source radiation, modelled by the McXtrace code. It is modelled to consistently have such a profile regardless of the energy of the photon beam.

[4]In accordance with the electron beam's distribution, which is considered to be Gaussian.

The spatial distribution of the photon beam in fig. 5.5 always has a Gaussian profile. In reality, the profiles of the beam's distributions are correlated with the energy and are modelled by SRW most accurately (fig. 5.4).

The instrument's components

Generally, the geometric aperture of the CRLs could act as an entry slit as well. However, to simplify the simulations and also to reduce numeric noise, the aperture was chosen to be a separate component. High horizontal divergence of the source led to the large horizontal dimension of the beam at the first optical element (fig. 5.2). The 1 mm entry circular aperture admits the entire beam vertically but excludes a large portion of it in the horizontal direction.

The structure of the CRL component code requires only the specification of the material that the lenses are made from, beryllium and aluminium in case of present experiment, without any additional knowledge of the X-ray constants. Such important characteristics as refraction index decrement and attenuation coefficient are provided by the McXtrace system. The parameters of the lenses and their number are given in section 5.2.

The horizontal cutting-off aperture opening did not have a big influence on monochromatisation, so it was constantly 200 µm to provide high intensity. The size of the exit aperture in the vertical direction, on the contrary, affected the degree of monochromatisation, hence it varied: the largest opening was 20 µm, the smallest opening was set to 5 µm and the medium opening was 10 µm. The various degrees of monochromatisation through the slits were detected with an energy monitor, which captures the photon beam's intensity as a function of its energy.

The running time of one simulation in McXtrace depends on the level of complexity of an instrument or a beamline, the number of photon events generated and the number of cores used for a simulation. There were 10^8 photon events, and it took about 1.8 hours to obtain each curve from fig. 5.6, running on one core.

5.3.2 Wavefronts propagation method

SRW simulations of the instrument

A detailed explanation of the underlying theory for the SRW code is given in previous publications [43] and is explained in detail in chapter 3. It exploits the laws of physical optics [44], where the transverse electric field is calculated beforehand and the radiation wavefront is constantly transformed upon its propagation through optical elements of a beamline. Partial coherence is taken into account by the summation of the intensities of the propagated electric fields of the synchrotron radiation, emitted by different electrons. The electron distribution in 6D phase space is assumed to be Gaussian, whereas the resulting photon distribution can strongly deviate from Gaussian.

The spatial distribution of the photon beam along with the spectral flux of the U22 undulator were calculated before the first optical element that acted as an acceptance aperture (fig. 5.3). The further propagation of the radiation was

simulated by an application of a sequence of the propagators corresponding to the CRLs and a number of drift spaces.

The current version of the SRW code is essentially oriented on propagating the monochromatic radiation. Since the underlying idea of the virtual experiment was in using the white beam, the following convention was used to model it: the entire energy bandwidth ΔE was split in quasi-monochromatic regions (a total of 20 of such bands) that were propagated through the beamline separately, then the results were integrated over ΔE.

The propagation of one wavefront for one photon energy in SRW takes many hours when running on one core. There were many parallel SRW simulations (for each energy from the spectral harmonic), so it took about one day in total.

5.4 The analysis of the modelling results

Fig. 5.6 shows the vertical cross-sections of the spatial distributions of the photon beam at the focal plane, which are calculated for the photons of the primary energy 35.61 keV. The neighbouring energies, due to different degrees of focusing at this plane, have different intensities.

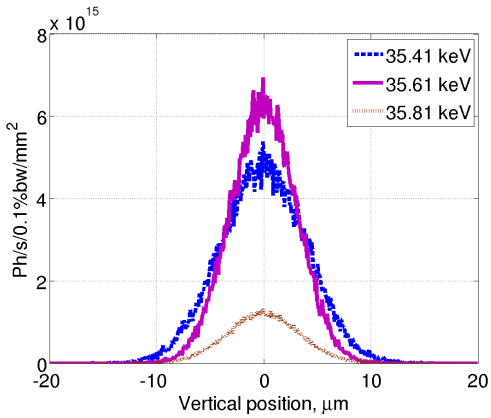

Figure 5.6: McXtrace results of the intensity distribution in the transverse plane of different photon energies at the geometric focus of 10 m.

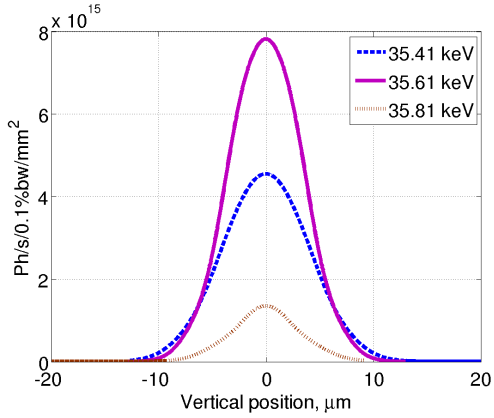

Figure 5.7: SRW results of the intensity distribution in the transverse plane of different photon energies at the geometric focus of 10 m.

The beam of 35.61 keV is at its geometrical waist and has the maximum intensity, which is in good agreement with theory. The beams of 35.41 keV and 35.81 keV are off their geometrical waists, hence their intensities are lower. Despite the symmetrical location of the two surrounding energies with respect to the primary one, their intensities at the focal plane are different nevertheless. This is explained by the asymmetrical profile of the undulator spectrum (fig. 5.3).

Fig. 5.7 depicts the vertical cuts of the spatial distributions obtained with the SRW simulation. The similarities between the results from both methods are evident. The intensity of the 35.41 keV curve achieved with McXtrace is 6%

higher than that of the SRW code, while the intensities of the other two curves with corresponding energies of 35.61 and 35.81 keV from McXtrace simulations show lower intensities than those of SRW by 23% and 7% respectively.

The spatial distribution of the beam, integrated over the entire 1 keV bandwidth ΔE, obtained by the SRW code and the equivalent distribution from the McXtrace programme are shown in fig. 5.8 and 5.9.

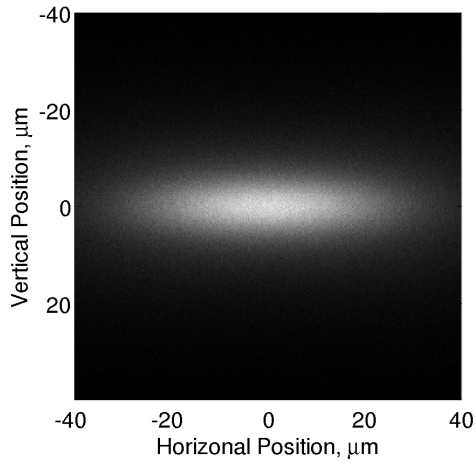

Figure 5.8: McXtrace spatial distribution of the white photon beam at geometric focus of 10 m for the primary energy.

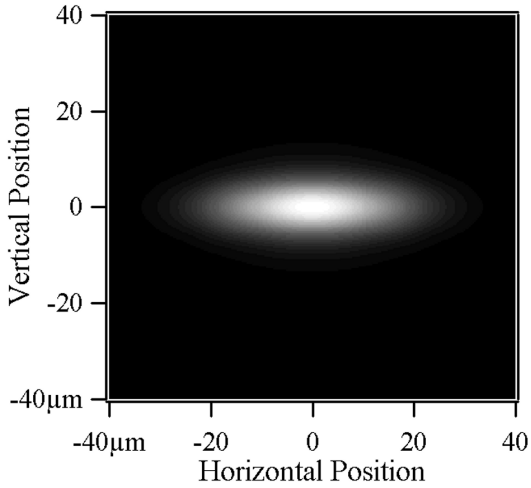

Figure 5.9: An integrated over ΔE spatial distribution of the white photon beam resulted from the SRW simulation.

The spatial distribution of the propagated photon beam (fig. 5.8) obtained from the McXtrace simulation is slightly larger than that generated by the SRW (fig. 5.9). The FWHM sections of both graphs show 43×11 µm^2 versus 30×9 µm^2 in the horizontal and vertical directions respectively. Such a discrepancy is partly caused by peculiarities of the wavefront propagation method (each wavefront has significantly more statistical data, so averaging over all propagated wavefronts leads to smoothing of the focused spot). Another impact leading to achieving a smaller focused spot was introduced by the peculiarities of the undulator radiation itself. Some photon energies were either not focused or focused poorly by the transfocator, hence the CRLs acted as a dispersive element more for those energies close to resonance. This explains also the discrepancies in fig. 5.6 and 5.7. All energies from the spectrum, in case of the ray-tracing method regardless of their intensities, had an equal impact on focusing, hence they were focused to a larger spot.

To show the monochromatisation by the slit of the propagated radiation, the photon beam's spatial distribution was integrated over the slit's dimensions. The output spectra obtained for different slit widths are presented in figures 5.10 and 5.11. The undulator entry spectrum is superimposed on both graphs in fig. 5.10 and 5.11, scaled by a factor of 0.127.

The main results of the virtual experiment simulated by the two methods, as expected for the cases of low X-ray coherence, are comparable, but not

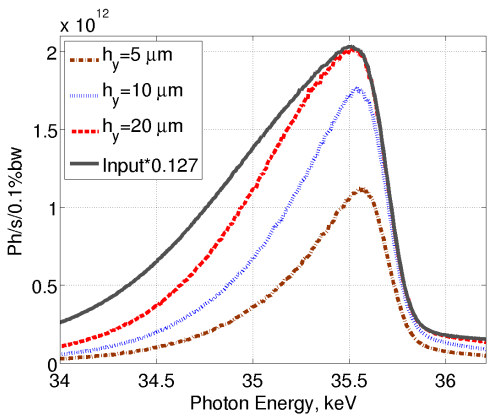

Figure 5.10: Monochromatisation of the entry spectral bandwidth: ray-tracing results.

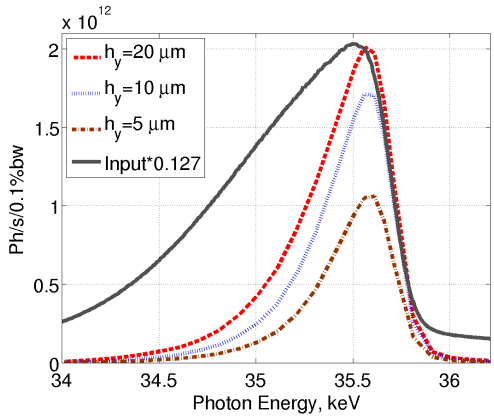

Figure 5.11: Monochromatisation of the entry spectral bandwidth: wave-front propagation results.

entirely the same. The FWHM sizes of the spectral curves from the matching slit dimensions are given in the table 5.2.

Table 5.2: The comparison of the widths of the quasi-monochromatic spectral curves, obtained from both McXtrace and SRW simulations.

Slit size h_y	McXtrace	SRW
5 µm	530 eV	387 eV
10 µm	620 eV	406 eV
20 µm	780 eV	455 eV

As can be seen from fig. 5.10 and 5.11, the monochromatisation of the entry spectrum obtained by the McXtrace programme is broader than that provided by the SRW code. This is due to the chosen approximations for modelling the source radiation in McXtrace. The intensity distribution was assumed to have a Gaussian profile. In reality, the undulator synchrotron radiation beam has different profiles that depend on photon energy (fig. 5.4). When such a beam is propagated in SRW, the spatial distributions of off-resonance photon energies have broader profiles and lower peak intensities, which increases the monochromatisation effect, thus resulting in narrower spectral curves. The ratio of the monochromatic widths from the two packages is presented in fig. 5.12, which shows that the discrepancies between SRW and McXtrace increase with the source size, therefore it is at least partially attributed to the spatial distribution of the source.

The empirical test at ID11 showed monochromatisation of the undulator harmonic to 337 eV with a 10 × 10 µm slit. The monochromatisation obtained by the SRW simulation provided the closest to the experimental result of 406 eV for the same slit size in the vertical direction. Possibly, if the horizontal size

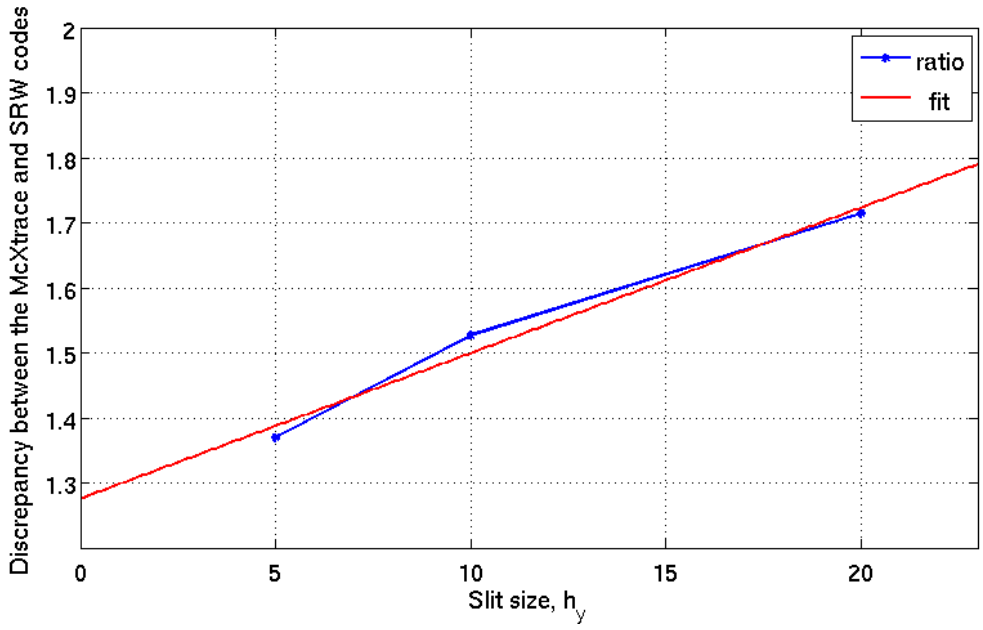

Figure 5.12: The ratio of the McXtrace and SRW degrees of monochromatisation.

of the slit opening was reduced to 10 µm, the simulation results would match the data more precisely, although the horizontal opening of 200 µm during simulation allowed significantly higher flux.

5.5 Conclusions

The detailed simulation of the synchrotron radiation propagation through a transfocator is introduced. The wavefront propagation and the ray-tracing methods were exploited for this purpose. Focusing properties of the monochromatic X-ray radiation modelled by ray-tracing, represented by the McXtrace package, were different of those modelled by physical optics, represented by the SRW code. The primary photon energy of 35.61 keV was 23% better focused (i.e. had more intensity) in case of the physical optics approach. Better focusing of the entire 1 keV energy bandwidth was also achieved with the physical optics approach, with a 43% and 27% (in horizontal and vertical directions respectively) smaller spot size than that obtained with ray-tracing. The monochromatisation effects from the pinholes of different sizes were again more significant in the case of physical optics simulations. The undulator harmonic of 1 keV bandwidth was most monochromatised with a slit of 200 × 5 µm, by 62% by the SRW code and by 47% by the McXtrace programme. The differences in the simulated monochromatisation results in particular and in other results are explained by the differences in modelling of the initial undulator radiation.

The SRW simulated results were more comparable with those obtained from the experimental test at ID-11, yet were not entirely the same. The absolute agreement with empirical results could be achieved with more knowledge about

the test's details, the structure of the beamline and nuances of the undulator parameters during the test.

Chapter 6

Simulations of several focusing experiments

This chapter is dedicated to a characterisation of the results of the beamtime experiments [45] at the Advanced Photon Source (APS) at Argonne National Laboratory, Illinois, USA. The experiments involved testing of the focusing properties of 1D beryllium lenses and 1D kinoform lens, which were set at different positions. The measurements were carried out at the ID32 beamline, typically used for imaging purposes. The simulation models were created in McXtrace, and the results of the modelling were then benchmarked with the empirical data.

6.1 Experimental setup at the ID32 beamline

The beamline had three hutches (A, B and C) with B and C being accessible by experimentalists. Hutches B and C, named alphabetically in accordance with their placement away from the straight section of the undulator, housed the tested optical components. The geometrical layout of the parts of the beamline containing optical elements in the hutches is presented in fig. 6.1. All distances were measured with respect to the straight section of the undulator, which excluded ambiguities upon further modelling.

A set of horizontal and vertical slits, tagged as *slits1* in fig. 6.1, were the first components after the vacuum tube in hutch B, preceding the 1D beryllium lenses by 250 cm. The lenses, stacked together and forming a CRL, were positioned at 36.25 m. The location of the CRL stayed constant through the entire experiment. Further along, the optical axis was surrounded by another vacuum tube in hutch B, which is omitted from the drawing. Another set of collimating horizontal and vertical slits, marked as *slits2*, was placed at 70.93 m; it was mounted after an ionisation chamber, which terminated a vacuum tube in hutch C. The second optical component being tested, a kinoform lens (KL) (section 6.4), had two positions designated *pos1* and *pos2* in the drawing; *pos1* was set at 71.13 m, whereas KL in *pos2* was moved downstream by 17 cm. The CCD area detector, marked *detector*, was put perpendicular to the optical axis; it was positioned relative to a Yag crystal, whose placement defined the total length of the beamline as 74.98 m.

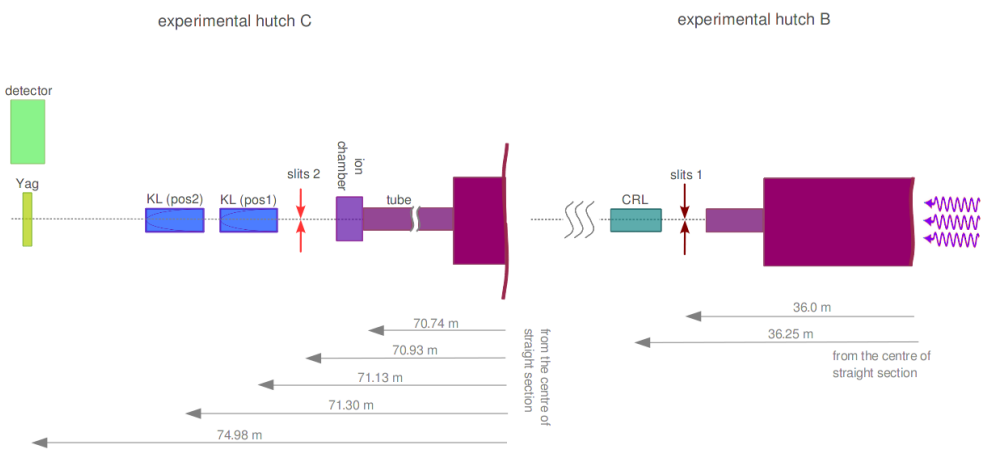

Figure 6.1: The experimental setup of ID32 at APS. The components are described in the text.

The electron beam parameters were taken from the APS website for the day of the experiment and were the following: RMS sizes in the horizontal and vertical directions σ_x=118.5 µm and σ_y=14.5 µm respectively; divergences in respective directions σ'_x=21.7 µrad and σ'_y=2.9 µrad. The radius of curvature at the tip of the parabola of the 1D lens was 0.5 mm, its geometric aperture - 1 mm, the lens's material was beryllium. The kinoform lens, on the other hand, was made of silicon, its horizontal aperture was 0.53 mm, vertical height - 80 µm and the length along the propagation axis was 2.03 mm. The detector effective area was 1280 × 1024 pixels, which corresponded to an actual size of 1715 × 1312 µm^2 in the horizontal and vertical directions respectively. The photon energy varied depending on particular tests and will be specified during the tests' descriptions.

6.1.1 Simulation model of the experiment: general features

The synchrotron radiation of ID32 was modelled by the geometric approximation used in the *Source_gaussian* component in McXtrace. The angular-spectral distribution of the undulator radiation was considered to have the a Gaussian distribution.

Since the approximation employed in the source component fully relied on the laws of geometric optics, it was of crucial importance to determine the true parameters of the beam. The effective size of the synchrotron radiation beam, σ_{eff}, depended on the widths of both the electron and photon beams, σ_{el} and σ_{ph} respectively, via quadratic summation. The electron beam parameters were available on the facility's website (stated in the above section), however, the parameters of the photon beam were unknown, therefore the effective beam size was recovered from the experimental data.

The algorithm for the reconstruction of the effective source size is the following. After passing through three lenses, the beam was vertically focused to $\Delta y'' \approx 24$ µm at the photon energy 8.83 keV (fig. 6.2). Employing the thin lens

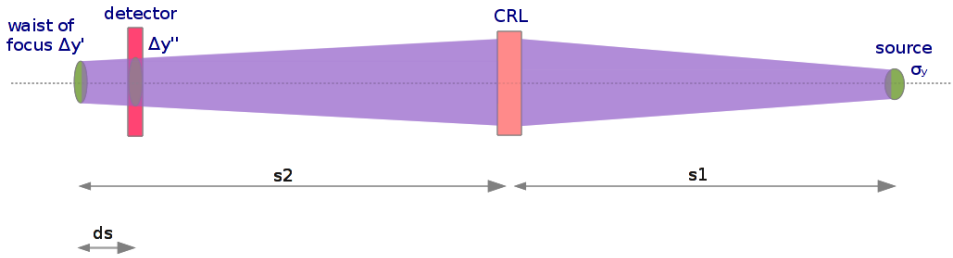

Figure 6.2: Drawing explaining the beam effective size retrieval: the vertical RMS of the effective source size σ_y, the source - object distance S_1, the object - image distance S_2, the shift of the detector plane with respect to the waist of focus ds, the vertical size of the beam at the detector plane $\Delta y''$ and the vertical size of the focused beam at its waist $\Delta y'$.

approximation, the location of the waist of the focused beam at this energy, S_2, was found to be 40.15 m downstream of the lenses. The position of the CCD camera relative to the CRL was 38.73 m, which implied that the waist was shifted by ds, equal to 1.42 m. The size of the focused beam off the waist position $\Delta y''$ depended on: the width of the focused beam at the waist, $\Delta y'$; the shift, ds, and the beam's divergence in the respective direction, namely, σ'_y, via $\Delta y'' = \sqrt{\Delta y'^2 + ds^2 \cdot \sigma'_y}$. On the other hand, $\Delta y'$ was correlated with the source size σ_y through a demagnification factor: $\Delta y' = (S_1/S_2) \cdot \sigma_y$.

Generally, the reconstruction algorithm implied an ideal situation, where the lenses had neither aberrations nor defects. Such a method, handling the data from focusing in just the vertical direction, provided an approximation to the effective source vertical value 20 µm. The data from other tests of 2D focusing (sections 6.3 and 6.5) had to be disentangled and treated separately, yet according to the same principles of the method; it revealed a vertical value of approximately 14.3 µm. Thereby the true effective source size must lie within the boundaries set by these two values, and after a numerous trials of different numbers within the defined region the most appropriate source size in the vertical direction was estimated to be 18 µm.

Recovery of the source effective area in the horizontal direction required data from the solely horizontal focusing by the kinoform lens (section 6.4), which was applied to the described above algorithm. The average value of such a retrieval was 129 µm, which did not account for any effects caused by the wave properties of the optic. The simulations with such a source size led to larger spot sizes than obtained experimentally, hence the real value was estimated to be 120 µm after various trials of tweaking the number within the range.

Depending on a specific test, the focusing optic was either a CRL consisting of different number of singular lenses, a kinoform lens or a combination of the two. The parameters of the CRL and the kinoform lens in the simulations were identical to those of the physical lenses (section 6.1). The positions of the active optical elements inside the beamline are individual for each test and will be referred to further in the text during the tests' descriptions. A new feature in

the *Lens_parab_Cyl* component was implemented during the simulations of the APS experiments, which allowed accounting for surface roughness effects. The roughness parameters of the physical lenses were not known, therefore during simulations they were tuned in such a way that the simulation results would resemble experimental.

A *PSD_monitor* stores the number of counts of photon events per single sampling bin per minute. To equate the data from the monitor with the data from a CCD detector of the beamline, the simulated values should be multiplied by the exposure time, which varied from test to test.

6.2 Test 1: focusing in the vertical direction with 1D lenses

Firstly, the vertical focusing of a CRL containing three beryllium lenses was measured. The position of the CRL was kept stationary (fig. 6.1), therefore the experimental finding of the waist location was performed through energy adjustments. The energy was scanned through values between 8.55 and 9.20 keV in variable steps of 0.01, 0.02 and 0.04 keV.

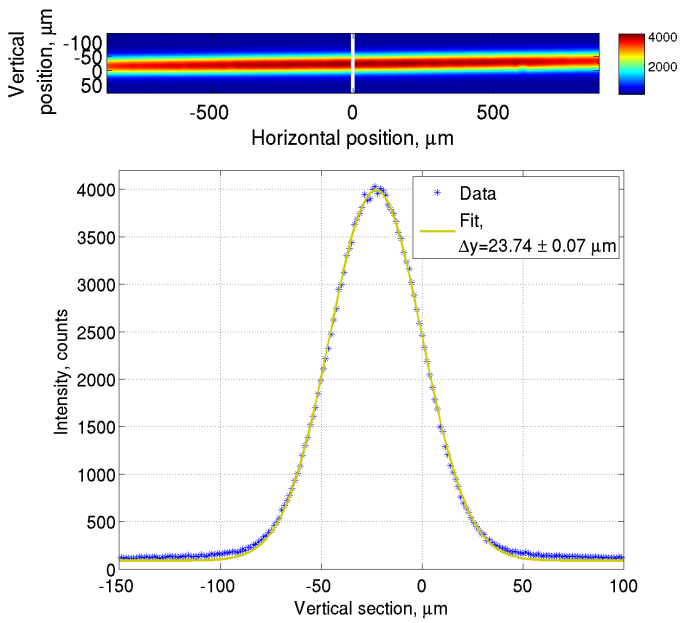

Figure 6.3: The beam focused vertically by three lenses. Top figure (a): the 2D image of the focused line. Bottom figure (b): the vertical cross-section of the previous 2D image.

A short batch of 10 images with 0.2 s exposure accompanied every energy scanning step. The width of the focused line - the so-called "width of focus" - within the images of the batch varied up to 13% (fig. 6.5). In order to model the test correctly afterwards, the width of the focused line corresponding to the energy 8.83 keV (the energy, at which the focused beam's spot was minimal)

was taken as an average value within the batch, i.e. $\Delta y = (24.03 \pm 1.05)$ µm[1].

The statistical treatment of such 2D images (fig. 6.3) involved cutting them horizontally and/or vertically (depending on focusing in either one or two directions) at pixels matching the most intensities, and their subsequent fitting with a Gaussian distribution function, which resulted in determining the RMS sizes of the peaks, or the widths of the focused beam, as well as the confidence intervals.

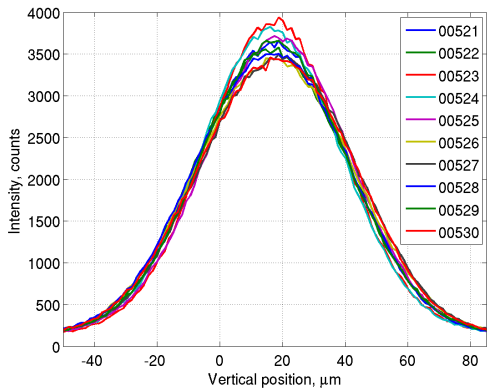

Figure 6.4: The vertical cross-sections of the individual images within the batch versus intensity.

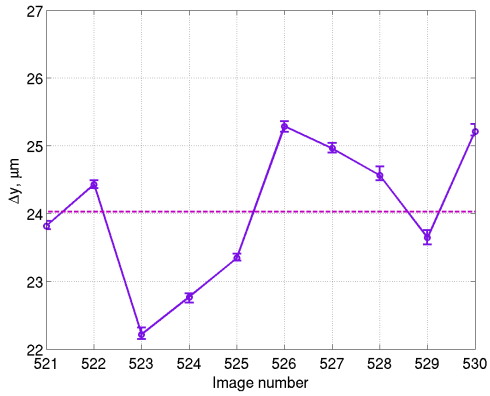

Figure 6.5: The statistical analysis of the batch images. The width of focus within the batch.

According to fig. 6.5, image number 521 had the nearest to the average value of the focused beam, hence it was chosen for further comparisons with the results of the modelling. The focused line from image nr. 521 is presented in fig. 6.3a; its vertical cross-section is illustrated in fig. 6.3b, in which the intensity of the focused beam (given in counts) is plotted against the vertical position (specified in microns); the fitting of the peak presented its RMS size $\Delta y = (23.74 \pm 0.07)$ µm.

6.2.1 The simulation of test 1.1 and its further comparison with the experiment

The simulations of the first series of tests were according to the model illustrated in fig. 6.6: the radiation from the source passing through a fully open slit (hence absent in the simulation's setup) is focused by a one-dimensional CRL (consisting of three individual lenses in test 1.1 and four in the case of test 1.2) to a detector plane, where it forms a thick horizontal line. The purpose of test 1.1 was to compare the widths of the horizontal focus between the experimental and simulated images. The intensity of the simulated focused line is scaled by the exposure time to match the experimental one.

[1]Generally, the RMS of a Gaussian distribution of any curve would have a σ notation, but in the current chapter it is referred to as Δ to exclude any ambiguities or any misinterpretations with the effective source sizes σ_x and σ_y.

, i.e.

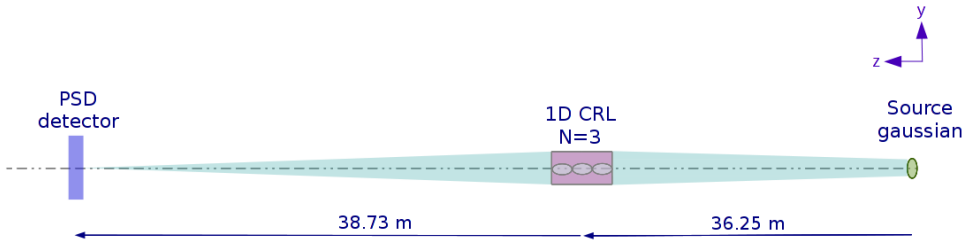

Figure 6.6: The McXtrace scheme that was implemented for the simulation of test 1.1.

The result of the simulation of test 1.1 is illustrated in fig. 6.7. The *PSD_detector* was aligned perfectly with respect to the beam propagation, hence the image of the focused beam is strictly parallel to the horizontal axis, as opposed to the slightly misaligned experimental one.

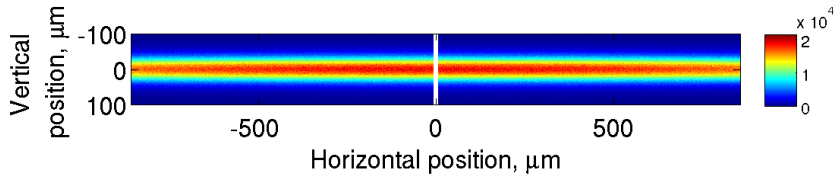

Figure 6.7: The simulated image of the beam focused by three lenses.

The cross-section of the image was made along the white line. The detailed comparison of the simulated peak with that obtained during the beamtime is presented in fig. 6.8.

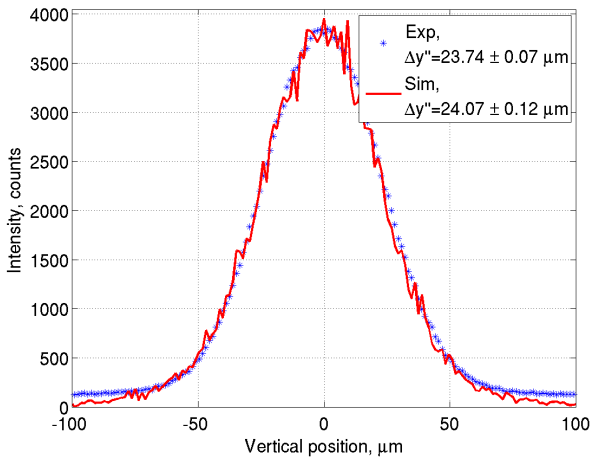

Figure 6.8: The experimental and simulated results: the red line represents the simulation, whilst the blue stars depict the experimental data.

The image of the focused beam elongated horizontally was divided into three parts. The middle part of it was chosen for comparison; the part of the image containing the peak itself was magnified. Both the simulated and experimental results were fitted with Gaussian distributions (equivalent to that in fig. 6.3b). The experimental data had some minimal background, that was absent in simulations, which is the only difference between the two data sets. The width of the simulated curve was (24.07 ± 0.12) µm, which aligned perfectly with the average width for the batch.

6.2.2 Collateral measurement of vertical focusing with four lenses - test 1.2: its simulation and comparison

The second part of the first series, test 1.2, was a brief measurement of the vertical focusing with a CRL comprising of four lenses. This measurement did not follow the previous one chronologically, nor was there an energy scan. It was performed in between the focusing measurements of the kinoform lens set at different positions. The energy suitable for the kinoform lens was 9.9 keV, therefore it was maintained at this value during further CRL focusing.

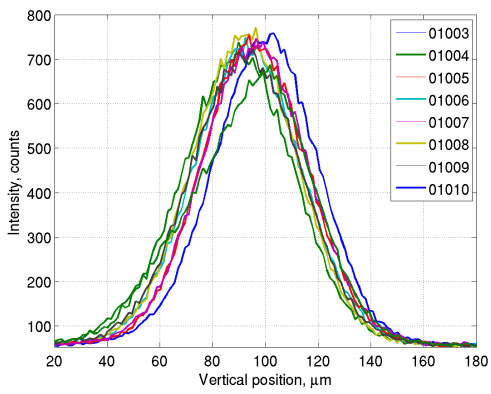

Figure 6.9: The vertical cross-sections of the images within the batch.

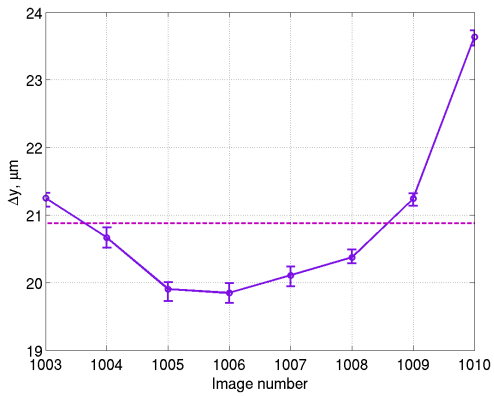

Figure 6.10: The width of focus within the batch.

A series of seven images (index numbers 1003-1010) was taken with a 0.01 s exposure time. Such a short exposure time resulted in a low count-rate on the detector. The vertical cross-sections presented in fig. 6.9 are shifted relative to one another, i.e. the centre of image 1006 is at approximately 90 µm (turquoise colour), whilst the centre of image 1010 is clearly falling to 100 µm (bright blue). This demonstrates the beam's vertical instability.

Similarly to test 1.1, the width of focus of individual images varied throughout the batch (fig. 6.10), hence the averaging resulted in a mean value (20.87 ± 1.24) µm. Image 1004 was chosen for further comparisons (fig. 6.11): it is tilted exactly as in the previous test (fig. 6.3a).

As follows from fig. 6.12, the simulated curve is identical to that obtained experimentally. The final tuning of the simulation curve was done through

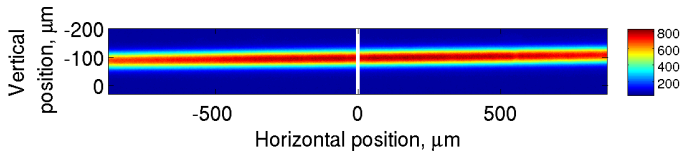

Figure 6.11: The 2D image of the focused by four lenses beam: the white line represents the cutting plane.

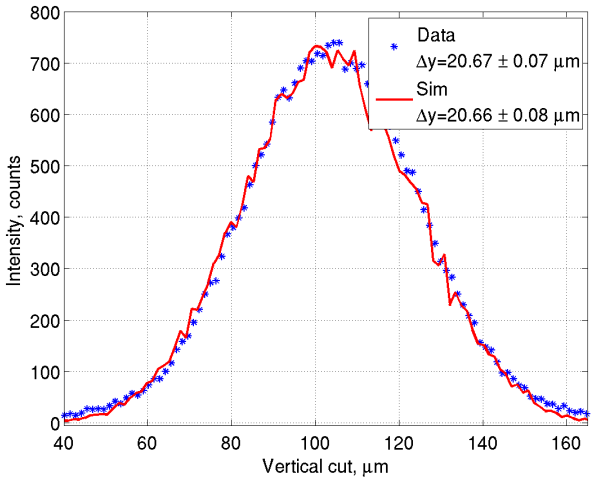

Figure 6.12: The comparison between the vertical cross-sections of the experimental and simulated data of test 1.2.

intensity scaling by the exposure time, which provided a perfect agreement of the two data sets.

6.3 Test 2: focusing in the horizontal and vertical direction solely with a CRL

The second test involved focusing in both directions with just 1D parabolic lenses: the CRL composed of 3 vertically and 3 horizontally oriented lenses, placed as before in hutch B (fig. 6.1). A set of 500 images of the focused beam was taken with a quick exposure time of 0.1 s at a photon energy of 8.82 keV.

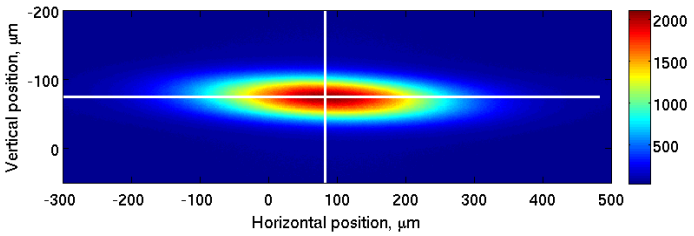

Figure 6.13: Experimentally obtained focused spot, the 2D image; the white lines show the vertical and horizontal sections.

The image in fig. 6.13 represents the focused area, with white lines showing the directions of the horizontal and vertical cross-sections. The horizontal widths of the focused spots, Δx, from all images within the batch are depicted on one plot (fig. 6.14). The mean value is (117.89 ± 0.36) µm; it is shown with pink dashed lines on both plots in fig. 6.14 and 6.15. However, averaging over a hundred of images from the middle of the batch illustrated in fig. 6.15 (an interval of the beam's stability) revealed (118.18 ± 0.10) µm, which is slightly higher than the mean value of the entire batch, but still falls into its confidence interval.

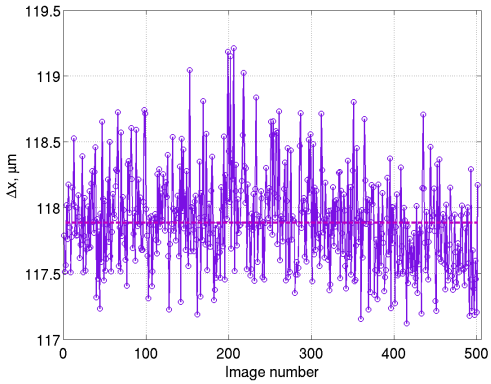

Figure 6.14: The horizontal sizes of the focused spot of all images in the batch; the pink dashed line shows the average value.

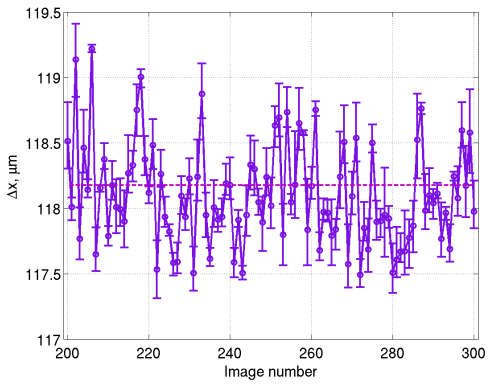

Figure 6.15: The horizontal sizes of the focused spot of only 100 images inside the batch; the pink dashed line shows the average value.

The statistical treatment of the vertical dimensions of the focused spot taken from the images of the entire batch, Δy, brought about (20.24 ± 1.17) µm (fig. 6.16). The averaging over a hundred images showed (20.87 ± 0.42) µm. The two mean values are in closer agreement than their horizontal counterparts.

6.3.1 Simulation and comparison of the test 2 results

The modelling of test 2 followed the procedure of the previous simulations (fig. 6.18). The radiation from the Gaussian source first passed through three vertically oriented lenses that were immediately followed by three horizontally oriented lenses. After passing through the lenses the beam was focused in two directions.

The 2D image of the simulated focus spot (fig. 6.19) is centered around the origin of the optical axis, the maximum counts on the *PSD_detector* are of the order of 10^4. To compare this intensity with that from the experiment, the simulated number is multiplied by the exposure time of 0.1 s.

As mentioned and shown previously, the focused beam was vertically unstable, hence it wasn't important which image to pick for further comparison as long as its dimensions were within the average range. Fig. 6.20 and 6.21 depict the comparisons of the vertical and horizontal dimensions of the focused

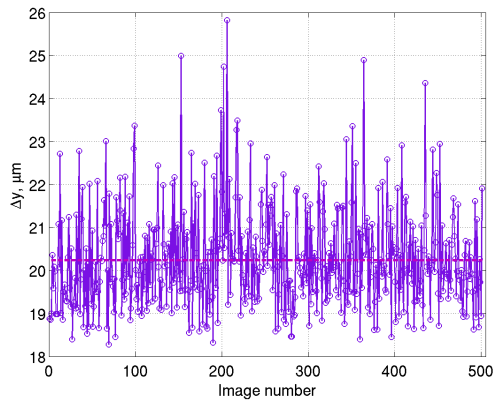

Figure 6.16: The vertical sizes of the focused spot of all images in the batch; the pink dashed line shows the average value.

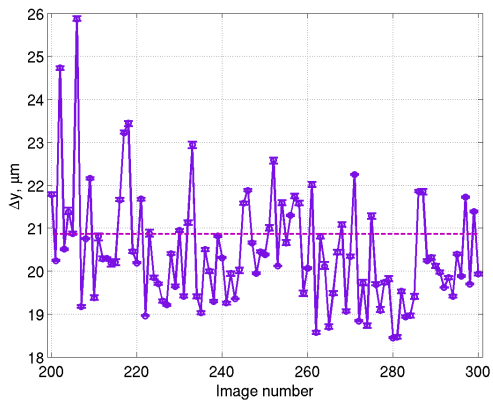

Figure 6.17: The vertical sizes of the focused spot of only 100 images inside the batch; the pink dashed line shows the average value.

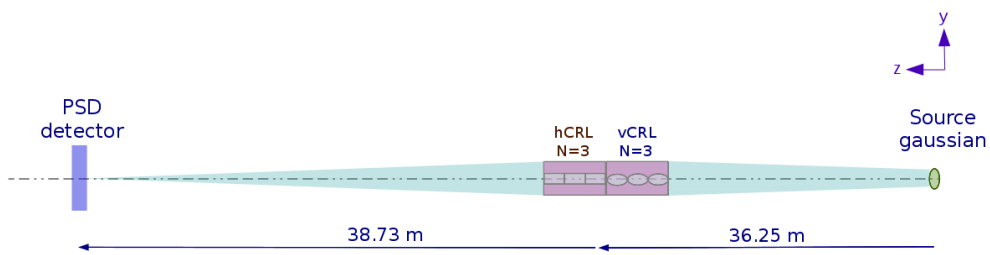

Figure 6.18: The McXtrace scheme of test 2: hCRL are the three horizontally oriented lenses and vCRL are the three vertically oriented lenses.

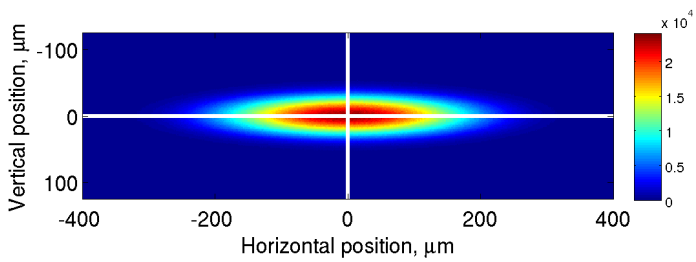

Figure 6.19: The simulated 2D image of the focused area in test 2; the white lines follow the horizontal and vertical sections.

area taken from image 200 and its simulated counterpart. The maxima of the experimental data were off-centre in both horizontal and vertical directions (fig. 6.13), hence the simulated curves were shifted accordingly to coincide with the experimental ones.

The dimensions of the experimental and simulated peaks agree well: the horizontal simulated curve is 4% broader than the experimental one, while the

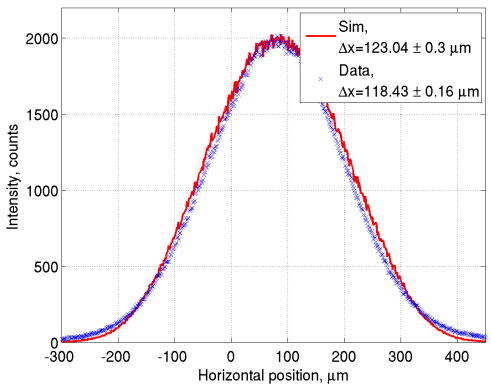

Figure 6.20: The horizontal width of focus of both simulated and experimental focused spot.

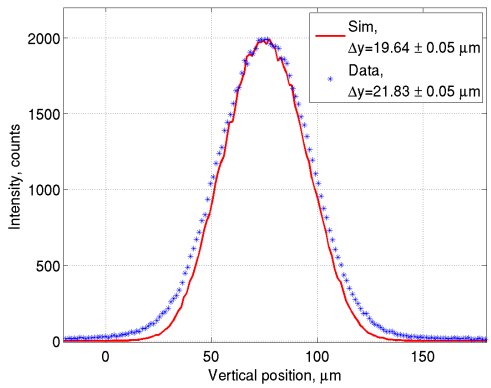

Figure 6.21: The vertical width of focus of the simulated and experimental focused spot.

vertical simulated curve is nearly 10% narrower than its experimental match. Generally speaking, the experimentally obtained peak is smaller than that expected by theoretical calculations. The positioning of the CRL with respect to the source and the detector (fig. 6.18) combined with the operating energy of 8.82 keV yields a demagnification factor of 1.107. This implies that the sizes of the beam at the waist of focus are larger than those at the source by a factor of 1.107. Hence, even if the source's effective size was equal to the electron beam size 118.5 µm × 14.5 µm (in reality, it is larger than that) the horizontal dimension of the focused spot would still be larger than 118.5 µm. So, perhaps, the unexpectedly small focused spot was the effect of the beam's intertwining on its propagation along the optical axis.

6.4 Test 3: focusing in the horizontal direction with a kinoform lens

The measurements of the third series were centered on the kinoform lens's (KL) performance[2] - a novel device developed at Brookhaven National Laboratory [46] and illustrated in fig. 6.22. It is a refractive lens with an elliptic profile. The outer surface of the lens is etched out in steps proportional to the ratio of the operating wavelength λ and the refractive index decrement δ. Such a design significantly reduces absorption, as the redundant material is removed. An image of a KL is shown in fig. 6.23. The focusing properties are equivalent to those of a standard refractive lens.

[2]In both tests of the third series the kinoform lenses were located in hutch C, relatively close to the detector.

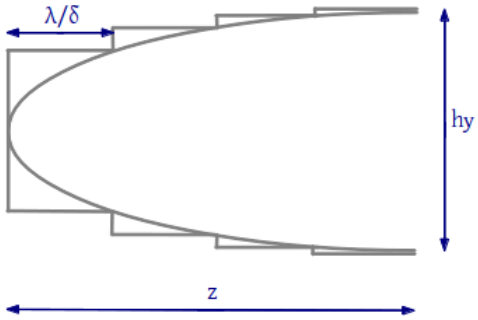

Figure 6.22: Schematic of a traditional kinoform lens.

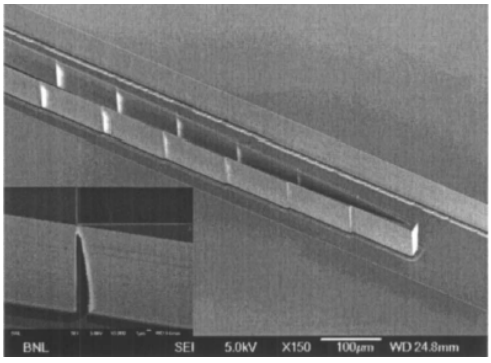

Figure 6.23: Scanning electron microscope image of a kinoform lens [46].

6.4.1 Test 3.1 - the kinoform lens at position 1

Firstly, the KL was put at position 1 (fig. 6.1), 71.13 m away from the straight section of the undulator. The KL was vertically fully covered by the beam, so the preceding slits' opening did not collimate it. The usual working energy-finding routine was performed in the interval between 9.0 and 10.65 keV with various steps. The rough scan (fig. 6.24) revealed a broad interval of interest, which then was scanned again with finer steps (fig. 6.25). Both of the scans helped configuring the optimal energy for obtaining a minimal focused spot. As can be seen in fig. 6.25, the working energy for test 3.1 was 10.45 keV.

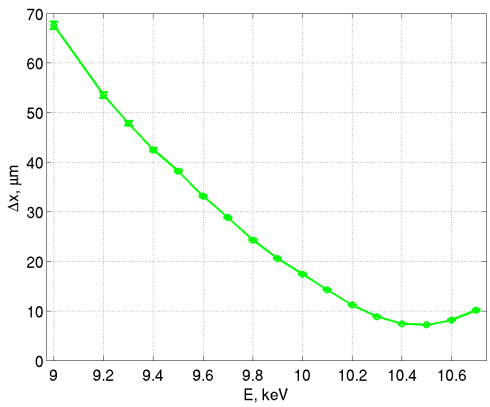

Figure 6.24: The rough scan configuring a working energy at which the focused spot is minimal: the width of focus Δx versus increasing energy.

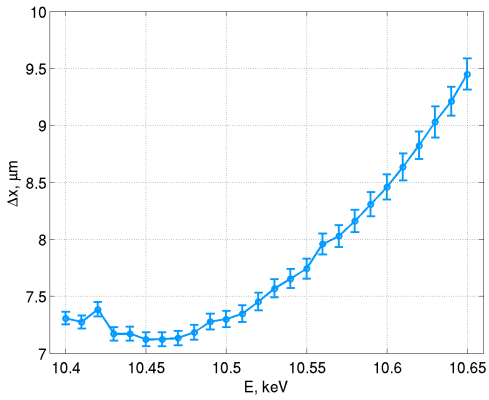

Figure 6.25: The fine scan with smaller steps configuring a working energy: the width of focus Δx is plotted against increasing energy.

A batch of ten images accompanied every scanning step, with the exposure time set to 0.05 s. The series corresponding to the defined working energy is present in fig. 6.26, in which the widths of focus of individual images are plotted

against time (displayed as the image number progression).

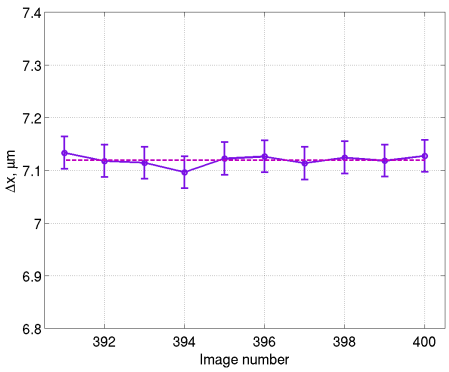

Figure 6.26: The width of focus of the individual images within the batch.

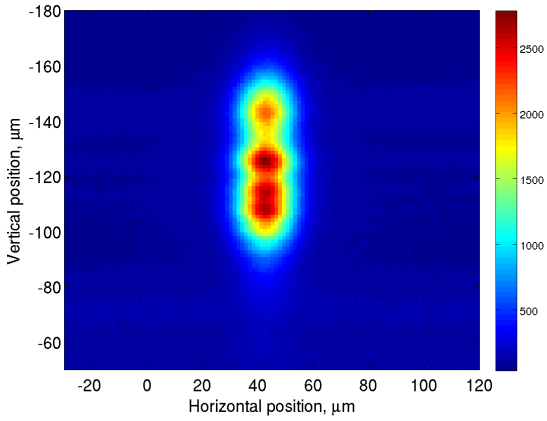

Figure 6.27: The 2D image 398 of the spot focused by the KL.

The beam was much more stable this time, hence the spread in the widths was not as large as with the CRL. The average horizontal width of focus was measured to be (7.12 ± 0.01) µm. The image most suitable for further comparison is nr. 398 (fig. 6.27). There appeared three distinct circles of the maximum intensity within the overall area of the focused spot instead of the almost homogeneous intensity spread observed with CRLs, perhaps, due to the specifics of the kinoform lens.

6.4.2 Simulation of the KL tests

The simulations of the tests of the third series were set according to the scheme illustrated in fig. 6.28: the radiation was focused horizontally by the kinoform lens, whose location varied in each test. *pos*1 was its placement in test 3.1 and *pos*2 was the position of the KL in test 3.2.

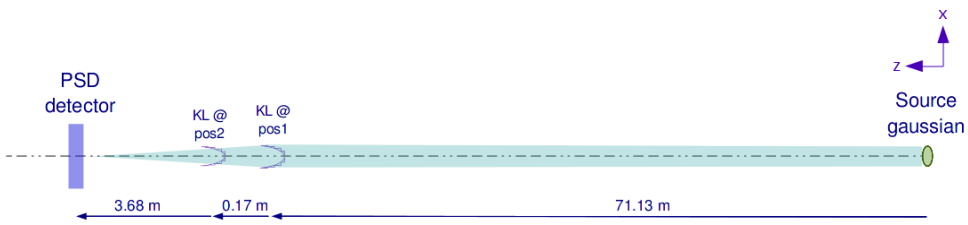

Figure 6.28: The simulation model implemented in McXtrace for the third series tests.

A new component was implemented specifically for the simulations of these tests: a kinoform lens. The concept of the component was not very different from the one used in the code for the parabolic refractive lens[3], although the

[3]It is described in detail in chapter 2.3.1.

dimensions of the inner elliptic profile were taken from a datafile provided by the fabricator, therefore the component represented a particular KL and cannot be used for an arbitrary kinoform lens. The transmission was calculated differently. Because of its zone-plate-like shape (parts of the material of the KL were etched out with a phase-dependent step size), there was very little material left, hence almost no losses for transmission.

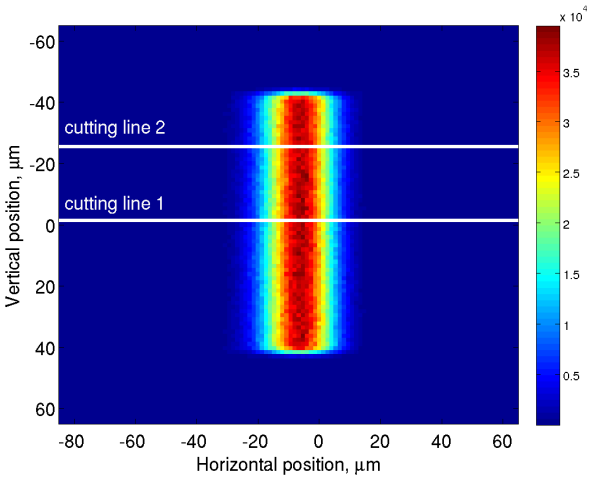

Figure 6.29: The simulated 2D image of the focused area in test 3.1; the white lines follow the horizontal cross-sections.

The outcome of the modelling is shown in fig. 6.29. The horizontal edges of the focused spot on the simulated image are sharp, in contrast to the experimental smooth ones. The intensity is spread out uniformly on the spot, as opposed to the three distinct experimental peaks. Therefore there are significant discrepancies between the simulation and experimental intensities presented in fig. 6.30 and 6.31.

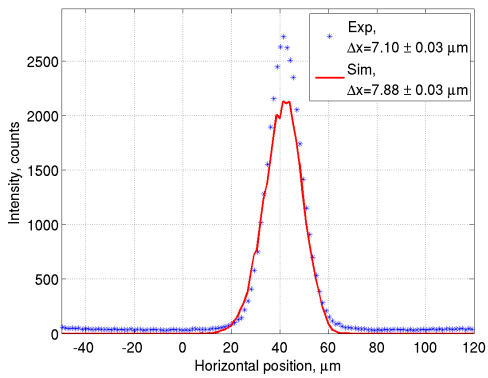

Figure 6.30: The comparison results of test 3.1 along the cutting line 1.

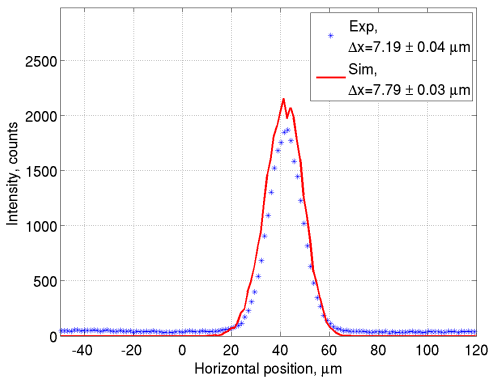

Figure 6.31: The comparison results of test 3.1 along the cutting line 2.

The simulated spot shows constant intensity, whilst the intensity of the

experimental peak falls down by 30% in the second cross-section. Those are the consequences of the previously mentioned separate circles of the experimentally focused beam. In terms of the widths of the spots, the simulation revealed wider sizes by 10% and 8% accordingly.

6.4.3 Test 3.2 - the kinoform lens at position 2

The KL was moved 17 cm closer to the detector, 71.30 m away from the straight section of the undulator (*pos*2 in fig. 6.28). Such a position corresponded better to the specifications of the lens - the lens was designed for the photon energy 10 keV, so the placement of the KL at *pos*2 allowed to alter the photon energy relative to the previous test. The energy scan spanned the interval between 9.8 and 10.30 keV.

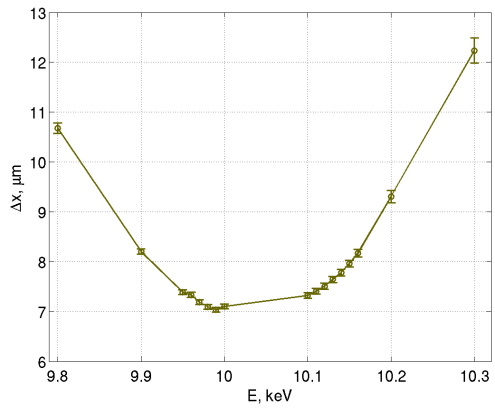

Figure 6.32: The configuration of the working energy in test 3.2

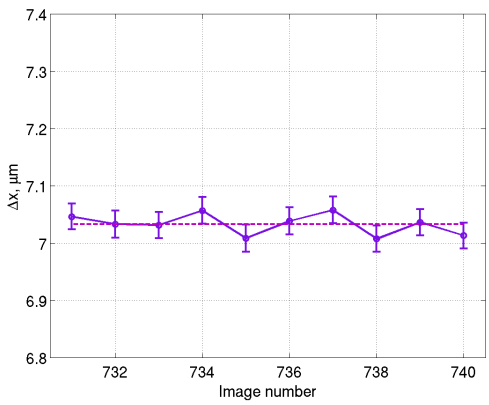

Figure 6.33: The widths of focus from individual images of the batch.

The working energy for test 3.2 was thus set to be 9.99 keV (fig. 6.32). Its corresponding batch is shown in fig. 6.33. The horizontal widths of focus did not differ quite much within the batch, with the averaging provided a mean value (7.03 ± 0.02) µm, and further analysis and comparison was done with image 732.

Similarly to the previous test with the kinoform lens, the experimentally obtained focused beam was not uniform and appeared in three almost separate areas of different intensity (fig. 6.34), while the simulated focused spot (fig. 6.35) was again homogeneously spread with sharp vertical edges. Therefore the comparison of the two spots was done at two locations - along the cutting plane 1 and plane 2. Even though the exposure time was identical to the one in test 3.1 (0.05 s), the maximum intensity of the middle focused area in test 3.2 nonetheless was higher (fig. 6.30 and fig. 6.36), which is explained by far more transmission of the KL at *pos*2.

The two lines in fig. 6.34 cut the experimental focused spot at areas corresponding to the local maxima. Since the simulated focused spot is uniformly spread, the vertical distance between the two cutting lines is a little longer than the one for the experimental spot (fig. 6.35). Despite the discrepancy of

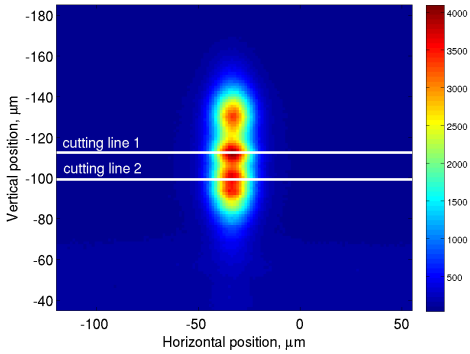

Figure 6.34: The experimental 2D image of the focused beam.

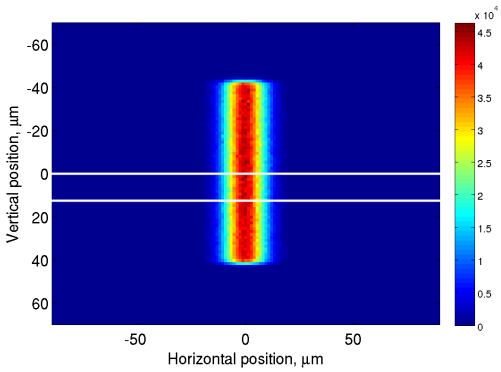

Figure 6.35: The simulated 2D image of the focused beam.

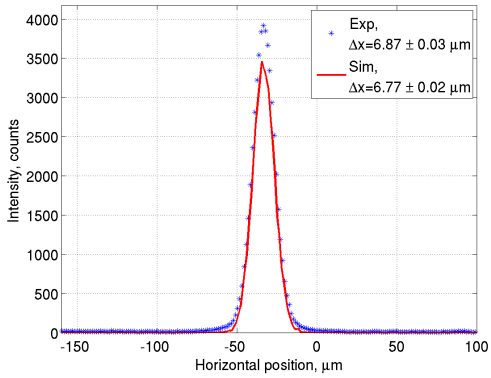

Figure 6.36: The comparison results of the two curves along the cutting line 1.

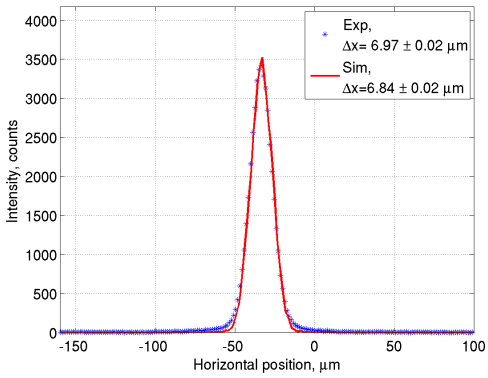

Figure 6.37: The comparison results of the two data along the cutting line 2.

intensities, independent on the simulation method, the widths of the focused spots coincide rather well: the experimental width is only 1.5% wider than the simulated one along the cutting line 1 (fig. 6.36) and 1.9% wider in the case of line 2 (fig. 6.37).

6.5 Test 4: horizontal focusing with KL and vertical focusing with CRL

The final and most important part of the beamtime was the test of the beam's manipulation in both directions with different optics: the CRL (consisting of four individual lenses), located at its permanent position in hutch B (36.25 m away from the straight section of the undulator, fig. 6.1), focused the beam vertically, whilst the KL, remaining at its last position in hutch C, i.e. 71.30 m away from the undulator, focused the beam in the horizontal direction. The

energy scan spanned the interval between 9.74 and 10.20 keV with a 0.02 keV step.

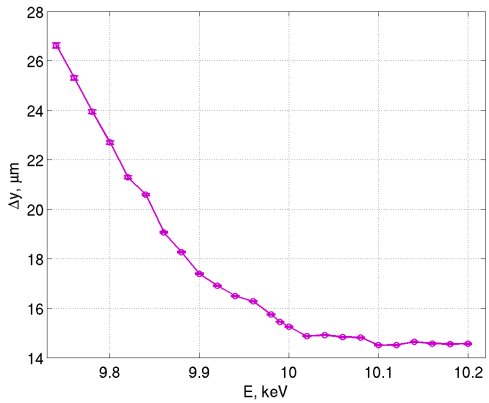

Figure 6.38: The energy scan of the vertically focusing CRL.

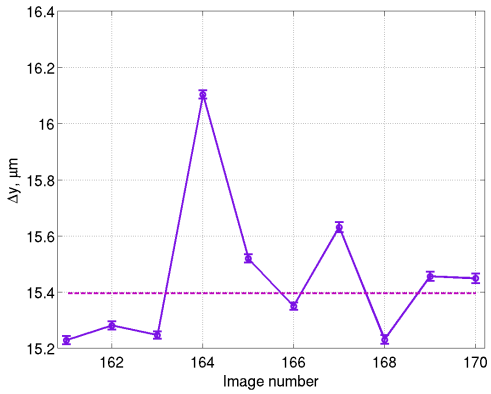

Figure 6.39: The width of focus of individual images within the batch.

During one of the previous tests of the beam's focusing solely by the CRL consisting of four lenses at the operating energy 9.9 keV (section 6.2.2) the average vertical width of focus was measured to be 20.87 µm (fig. 6.10). This time, since there were two focusing elements in the beamline, the energy had to be chosen to satisfy both of them. The energy was set to 9.99 keV, which implied the optimal energy for the horizontal KL focusing. Fig. 6.38 illustrates the dependence of the vertical width of focus with increasing energy, and it clearly shows that Δy is approximately constant above 10 keV. Fig. 6.41 shows averaging of the batch of ten images. The mean vertical size is then (15.40 ± 0.11) µm.

It is though noticeable, that the vertical width of focus in test 4 at the photon energy 9.9 keV, according to fig. 6.38, is 17.4 µm, which is 20% narrower than the vertical size of the focused beam in test 1.2. Following the consideration of the location and the number of individual lenses in the CRLs in both cases, the sizes of their resulting focusing should agree better. Perhaps, shrinking of the beam vertically in test 4 is the beam's crossing effect.

The evolution of the horizontal dimension of the focused beam with the energy variation is depicted in fig. 6.40, in which the curve repeats the tendency shown earlier in fig. 6.32 from the previous single KL focusing test 3.2. The average horizontal width during this test is (6.83 ± 0.02) µm, which is 3% narrower than the result obtained while testing the horizontal focusing of the KL on its own.

When being focused in both directions, exactly as in test 2, the beam was vertically unstable, hence its sizes in respective directions were not consistent. To analyse an image from the batch of the working energy and to further compare it with a simulated one, it had to be as close to the mean value as possible both horizontally and vertically. Therefore image 163 was chosen (fig. 6.39 and fig. 6.41).

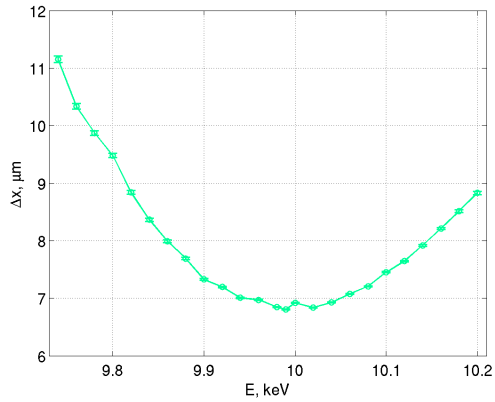

Figure 6.40: The energy scan of the horizontally focusing KL.

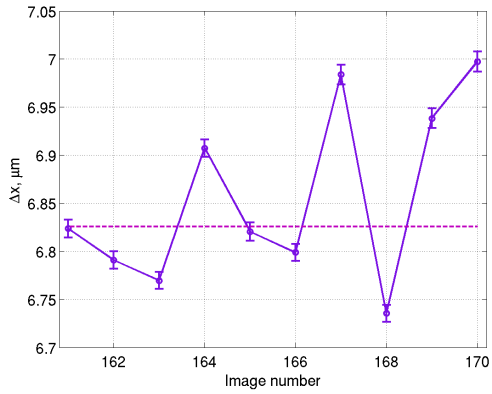

Figure 6.41: The width of focus of individual images within the batch.

6.5.1 Simulation and comparison of the results of test 4

The model of test 4 in the language of the McXtrace package is presented in fig. 6.42.

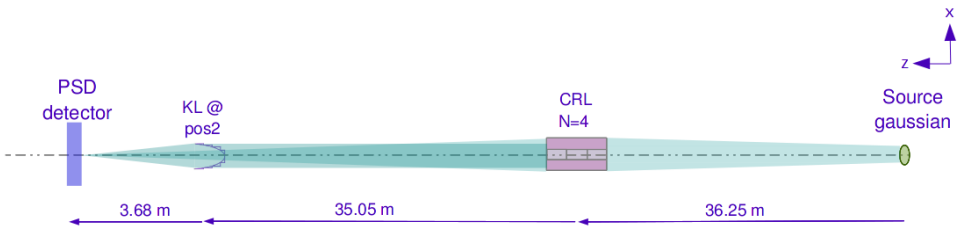

Figure 6.42: The model implemented for test 4.

The photon beam from the source was at first vertically focused by the CRL placed at its permanent position, and secondly it was horizontally focused by the KL located only 3.68 m away from the detector. All components used for the simulation of this test were described previously. The outcome of the modelling along with its experimental counterpart image 163 are illustrated in fig. 6.43 and 6.44.

The white lines follow the horizontal and vertical cutting planes, which sections are presented below in fig. 6.45 and 6.46. The simulation repeats the geometrical shape of the experimental spot in a straightforward fashion, i.e. perfectly aligned ellipse. The experimental spot, on the other hand, is deformed from an ideal shape. It is slightly bent towards the left, hence the cutting planes had to be bent as well to reproduce the actual size of the spot.

The comparisons of the curves are presented in fig. 6.45 and 6.46: the horizontal dimensions of both experimental and simulated peaks agree very well: the latter is only 5% wider. The vertical sizes of the two data sets diverge slightly more: the experimental curve is 20% narrower than its modelled counterpart.

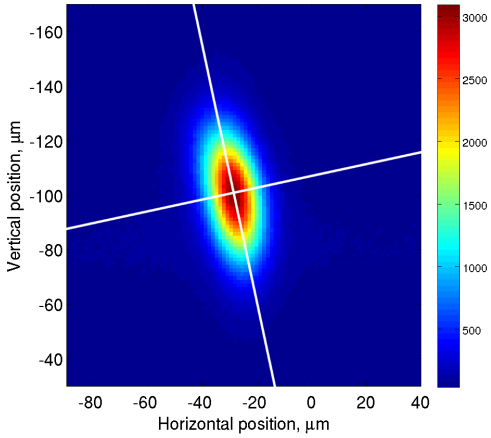

Figure 6.43: The experimental image 163 with the white lines showing the sections.

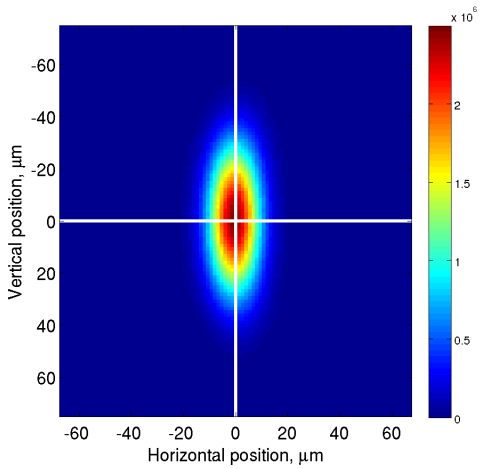

Figure 6.44: The 2D simulated image of the beam focused vertically by the CRL and horizontally by the KL.

6.6 Discussions and conclusions

This section is dedicated to an overview and a discussions of the beamtime experiments: its objectives, results and conclusions. The summary of the paragraph is split into several parts: the verification of the source size, simulations and the results from all the tests. The latter are discussed in groups according to their characteristics: tests 1 and 3 centered on one-dimensional focusing, while tests 2 and 4 investigated the two-dimensional focusing.

6.6.1 Rectification of the effective source size

From an analysis of the focused spots the effective size of the beam coming from the straight section of the undulator was different to that suggested by the accelerator's department for the day of the experiment (σ_x=118.5 µm and σ_y=14.5 µm). The algorithm described in section 6.1.1 suggested a better estimate of the dimensions of the beam size: σ_x=129 µm and σ_y=21 µm. The use of these parameters in the simulations in McXtrace resulted in much larger spots than observed experimentally. Therefore the true values of the source size for the simulations of the experiment were chosen inside the intervals drawn by the two numbers above: the horizontal width σ_x=120 µm and the vertical height σ_y=18 µm, which allowed obtaining better similarity with the experimental curves. The values of the beam divergences declared on the website for the day of the experiment were used for the simulations without any alterations.

6.6.2 Review of the 1D focusing experiments and simulation

The sequence of tests 1 focused the beam vertically with the help of beryllium CRL, and the set of tests 3 did so horizontally using a silicon kinoform lens. The numbers supporting the comparison results of the sequence of tests 1 are

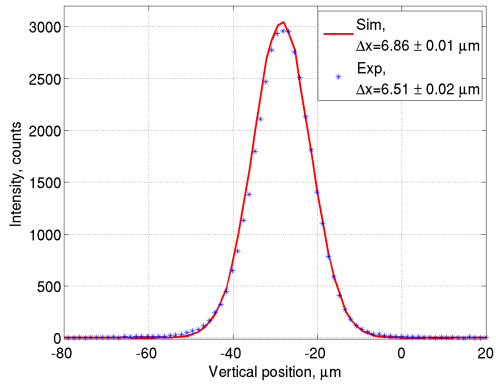

Figure 6.45: The comparison of the horizontal sizes of the focused spot.

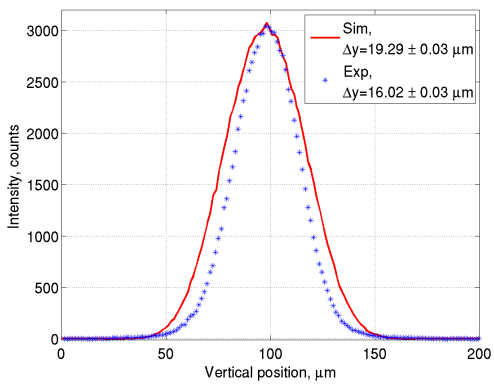

Figure 6.46: The comparison of the vertical dimensions of the focused spot.

provided in tables 6.1 and 6.2, they prove an excellent agreement between the data.

Table 6.1: The results of the vertical focusing in test 1.1.

batch average Δy	24.03 ± 1.05 µm
experimental Δy	23.74 ± 0.07 µm
simulated Δy	24.07 ± 0.12 µm
difference	0.1%

Table 6.2: The results of the vertical focusing in test 1.2.

batch average Δy	20.87 ± 1.24 µm
experimental Δy	20.67 ± 0.07 µm
simulated Δy	20.66 ± 0.08 µm
difference	1%

The shape of the experimentally focused beam, which in the tests of the first series was just a horizontal thick line, was reproduced perfectly by the simulations. The minimal background noise from a parasitic scattering during experiments is absent in simulations, which put in a tiny discrepancy upon comparison of the intensities.

The simulation of the horizontal focusing in the series of test 3 (tables 6.3 and 6.4) also showed a good correlation.

Table 6.3: The results of the horizontal focusing in test 3.1.

batch average Δx	7.12 ± 0.01 µm
experimental Δx	7.10 ± 0.03 µm
simulated Δx	7.88 ± 0.03 µm
difference	10%

Table 6.4: The results of the horizontal focusing in test 3.2.

batch average Δx	7.03 ± 0.02 µm
experimental Δx	6.87 ± 0.03 µm
simulated Δx	6.77 ± 0.02 µm
difference	4%

It is, perhaps, because the kinoform lens according to its nature moulds the phase-space of the incoming beam, that the result of its focusing turned out non-uniform: the intensity inside the focused area is divided into minor circular regions, as seen in fig. 6.27 and 6.34. The intensities of the minor regions are then variable. The simulated focused spot, on the contrary, is of a cylindrical

shape with a homogeneous intensity spread and sharp vertical edges. Therefore the comparison of the two data curves is done at two different locations corresponding to the experimental maxima, which introduced the discrepancies of intensities.

6.6.3 Overview of the two-dimensional focusing experiments

Both test 2 and 4 aimed at focusing the beam in two directions. Both of them used the CRL for vertical focusing, while they differed in their means for horizontal focusing. In the case of test 2 another CRL with three 1D lenses was used, whilst in the case of test 4 it was the kinoform lens. As it follows from tables 6.5 and 6.6 the test 2 simulation corresponds well to the original. The experimentally focused spot was a little tilted, whilst the simulated focused area was aligned correctly. The beam's horizontal inclination was always present throughout the entire beamtime experiment and is probably caused by alignment problems due to the monochromator.

Table 6.5: The results of the horizontal part of focusing in test 2.

Horizontal batch average Δx	117.89 ± 0.36 µm
mean over a hundred images Δx	118.18 ± 0.10 µm
experimental Δx	118.43 ± 0.16 µm
simulated Δx	123.04 ± 0.3 µm
difference	4%

Table 6.6: The results of the vertical part of focusing in test 2.

Vertical batch average Δy	20.24 ± 1.17 µm
mean over a hundred images Δy	20.87 ± 0.42 µm
experimental Δy	21.83 ± 0.05 µm
simulated Δy	19.64 ± 0.05 µm
difference	6%

The focused spot's inclination is most visible and noticeable in test 4, where the KL focused the beam horizontally and the CRL did so vertically. The CRL focused the beam into an unexpectedly small area, the size of which in simulations was dictated by theory. The 20% discrepancy in that particular parameter stands out from the rest of the results, however it is still considered as good agreement in general simulations. This can perhaps be ascribed to the previously mentioned alignment problem. Tab. 6.7 shows the results of the horizontal focusing with a good agreement in the case of the KL focusing.

Table 6.7: The results of the horizontal part of focusing in test 4.

Horizontal batch average Δx	6.83 ± 0.02 µm
experimental Δx	6.78 ± 0.02 µm
simulated Δx	6.86 ± 0.01 µm
difference	4%

Table 6.8: The results of the vertical part of focusing in test 4.

Vertical batch average Δy	15.40 ± 0.11 µm
experimental Δy	15.36 ± 0.03 µm
simulated Δy	19.29 ± 0.03 µm
difference	20%

The presented above tables of the comparison results for all tests showed how well they were reproduced by the McXtrace simulations.

Chapter 7

Summary conclusions and outlook

The scientific aim of the present PhD work was focused around development and further validation of the McXtrace package, therefore the demonstrated results of the present dissertation are evaluated from the relevant point of view.

The McXtrace project was initiated in the beginning of 2009. The paperwork associated with it was settled within half a year, and the active development of the package started in summer. I joined the development team in the beginning of August of that year.

In the beginning, a great amount of work was dedicated to establishing a solid components library. Some of the components were directly transferred from McStas (for instance, slits and monitors), some had to be written from scratch. I was particularly involved in coding optical components, creating a variety of models for X-ray lenses.

Once the package was sufficiently developed, the first beamline simulations were performed, the results of which are reflected in the present dissertation. The official release of the first version of the software occurred in October 2011.

7.1 Simulations overview

In the first simulation project, the SAXS instrument model was created in McXtrace. The validation of the model was performed through comparison of the virtual photon beam propagation with the empirical one, the propagation of which was obtained experimentally. The initial model was set up according to the parameters provided by the instrument responsible and did not confirm the experimental data accurately, therefore some adjustments had to be made to the model. The simulations obtained with the new model matched the experimental data with good precision. While the goal of the simulation project was fulfilled, i.e. the model reproduced the experiment, a question remained as to how accurate the geometry used in the simulation actually was, as it was not possible to confirm the ambiguous geometrical nuances inside the SAXS machine.

The second simulation project was dedicated not only to benchmarking the

software against reality, but also to validating McXtrace against another modelling code. The two programmes are built on intrinsically different techniques, shedding light on the particle nature of X-rays in one case and emphasising their wave properties in the other. Usually, to compare results obtained by two different packages, it is a necessary condition that they share common principles, i.e. ray-tracing results from one code should be compared to ray-tracing results from another, since otherwise the comparison wouldn't be equivalent. However, some modelling cases[1] could be represented equally well by the seemingly incompatible software. Such a project is the simulation of the transfocator's performance as an elementary and low cost monochromator. Its operation with both mono- and polychromatic radiation was simulated. The comparative analysis of the results provided by the packages revealed that the focusing properties (the ability to focus radiation of neighbouring energies differently - the dispersion) of the modelled device are directly influenced by the way the initial radiation is depicted. There is a diversity of spatial profiles of the source radiation, which was summarised into a single distribution by McXtrace, whereas the SRW code maintained the entire collection of profiles. Therefore the outcome achieved by McXtrace turned out worse than that shown by SRW. Thereby this project showed new perspectives for further improvement of McXtrace.

Modelling of another focusing experiment was the last simulation project. A number of single parabolic lenses and a kinoform lens were experimentally tested. Different configurations of the focusing setup were investigated, which are going to be implemented in one of the beamlines of a new synchrotron. The McXtrace modelling of all the setups is presented. The overall agreement between the simulated and experimental results is very good. Yet, the comparison of one particular test (chapter 6.5) showed a high discrepancy. The analysis of the origin of the dissimilarity suggested problems in the experimental configuration, which was simulated in a symmetric geometry. In other words, the experimentally obtained image was tilted, whereas the simulated spot was perfectly straight. The empirical tilt, supposedly, was effectively caused by the imperfection of the X-ray beam during data acquisition.

7.2 Outlook

At its current level of development the McXtrace package is a reliable, flexible and powerful tool for modelling X-ray scattering instrumentation, as the numerous examples, not only those presented, have shown. Based on the benchmarking of McXtrace performed in this dissertation, the following recommendations are given for future development of the code.

Firstly, to increase the credibility of the package, a more realistic model of a synchrotron radiation source must be implemented. The current version of the source requires an additional file describing the spectral distribution of the

[1] For instance, such simulations where the wave-nature phenomena of the X-ray radiation is of low importance or the radiation is considered at specific conditions where the effects caused by the interfering waves are negligible.

radiation. Even though calculation of synchrotron radiation spectra is not in the scope of the McXtrace package, it could be convenient to realise a reliable communication between a third-party software that generates such spectra, which could be automatically ported into McXtrace upon necessity.

Moreover, another modification to the source model could be implemented, which would take into consideration the effects of the photon beam's spatial distribution. At present, the spatial profile of the photon beam always has a Gaussian shape, which isn't the case for off-resonance energies of the spectrum. Most often the energy used in experiments, hence the energy in simulations, is monochromatic. Therefore there is no effect from the neighbouring energies and a simulation is in perfect agreement with experiment. Yet in those experiments utilising polychromatic radiation, like the one shown in chapter 5.4, these effects start playing a big role, which worsens the simulation results.

The present situation in the world of the experimental X-ray physics, especially in the light of the full power operation of the Free Electron Laser facilities [47], demands the appearance of a fundamentally novel simulation tool. Therefore a new insight into this problem is crucial. A unification of the two most popular methods for modelling X-ray radiation, wavefronts propagation with ray-tracing, could be one of the solutions. An example is illustrated in fig. 7.1.

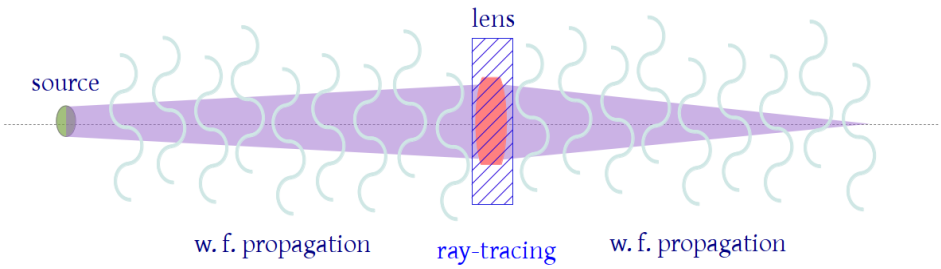

Figure 7.1: An elementary setup to portray a novel modelling approach based on the combination of two simulation methods.

The propagation of X-ray radiation in free space, i.e. between optical components of a beamline, could be presented by the wavefronts propagation technique, whereas interaction of X-rays with the matter of optical components, i.e. refraction/reflection/absorption phenomena, could be well calculated within the frame of ray-tracing. Such a complete depiction would allow accounting for the wave characteristics of the radiation, hence quantify the interference effects, along with the time-efficient calculation of the radiation transition through optical elements, expediting the overall simulation time. Such a hybrid wavefront-ray-tracing code is perhaps the optimal long-term goal for McXtrace project.

Appendix A

Determination of the bilayer thickness at the intersection point

Fig. A.1 illustrates a multilayer mirror placed inside an ellipse. A thorough explanation of defining the mirror's surface via the parameters of an ellipse such as source-object distance p, object-image distance q and incidence angle θ is given in [48].

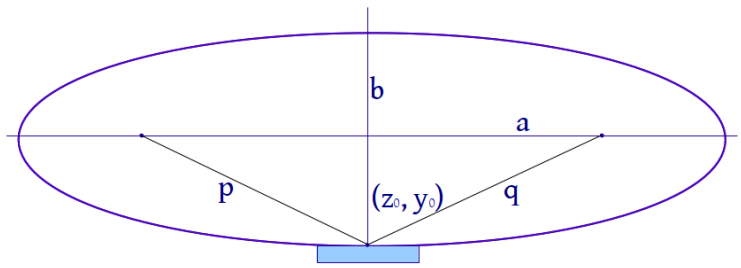

Figure A.1: Elliptically curved mirror.

The centre of the mirror z_0 is correlated with the elliptic parameters via

$$z_0 = a \cdot cost_0, \tag{A.1}$$

where $cost_0$ is an auxiliary parameter connecting the mirror's position on the ellipse and the angle of incidence

$$cost_0 = \frac{1 - M}{\sqrt{1 - 2 \cdot M + M^2 + 4 \cdot M \cdot \cos\theta}}. \tag{A.2}$$

The mirror's position on the ellipse with respect to the object and image distances is commonly referred to as a demagnification factor M, $M = q/p$.

The multilayer is designed with various bilayer thicknesses d, as illustrated in fig. A.2. Its reflectivity is directly proportional to d-spacings. The incoming photons intersect the surface of the multilayer at different locations, therefore a correlation between the intersection points coordinates and the relevant thickness d is essential for an adequate modelling of the multilayer's reflectivity.

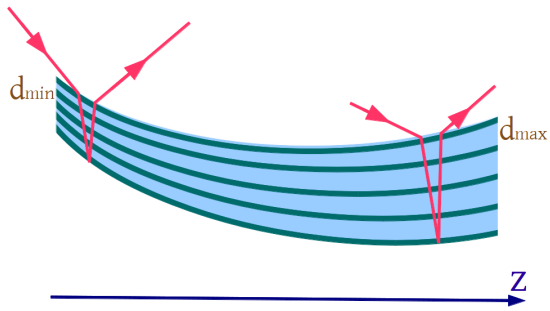

Figure A.2: Schematic of the multilayer with various d-spacing.

The derived expression is rather long, hence two subsidiary terms T_1 and T_2 are introduced:

$$T_1 = z + z_0, \tag{A.3}$$

$$T_2 = \frac{-(b^2 \cdot a^2 + b^2 \cdot (z + z_0)^2)}{a^2} \tag{A.4}$$

where a and b are the elliptic parameters of the multilayer, z_0 is the z-coordinate of the origin of the multilayer (fig. A.1). Then the correlation for $d(z)$ yields

$$d = 0.5 \cdot \lambda / \left(\cos \left[\operatorname{acos} \left(\frac{\sqrt{T_2}}{\sqrt{T_2} + c^2 + 2 \cdot c \cdot T_1 + {T_1}^2} \right) - \operatorname{atan} \left(\frac{T_1 \cdot b^2}{\sqrt{T_2} \cdot a^2} \right) \right] \right) \tag{A.5}$$

where λ is the radiation wavelength and c is the last elliptic parameter.

Appendix B

Components source codes

```
/*****************************************************************
*  McXtrace, X-ray tracing package
*          Copyright, All rights reserved
*          Risoe National Laboratory, Roskilde, Denmark
*          Institut Laue Langevin, Grenoble, France
*          University of Copenhagen, Copenhagen, Denmark
*
* Component: Lens_parab_Cyl_rough
*
* Written by: Jana Baltser and Erik Knudsen
*
* Date: April 2011
* Version: 1.0
* Release: McXtrace 0.1
* Origin: NBI
*
* A simple X-ray compound refractive lens (CRL) with a parabolic cylinder profile, it focuses in 1D.
*
* Input parameters:
* r - raduis of curvature (circular approximation at the tip of the profile) [mm];
* yheight [mm]
* xwidth [mm]
* d - distance between two surfaces of the lens along the propagation axis;
* N - amount of single lenses in a stack.
* deltaN- auxiliary parameter = delta*Number of lenses, valuable in cases when applying thin lens approximation to thick lens properties.
* rough_xy [rms] - waviness along x and y
* rough_z [rms] -waviness along z
*
* attenuation coefficient mu is taken from the NIST database and
* Be.txt
*
*****************************************************************/

DEFINE COMPONENT Lens_parab_Cyl_rough
DEFINITION PARAMETERS (string material_datafile="Be.txt")
SETTING PARAMETERS (r=.5e-3,yheight=1.2e-3,xwidth=1.2e-3,d=.1e-3,T=.99,N=1,deltaN=0,rough_z=0, rough_xy=0)
OUTPUT PARAMETERS (prms,parab)
```

```


SHARE
%{
  %include "read_table-lib"
  struct datastruct{
    int Z;
    double Ar, rho;
    double *E, *mu, *f;
  };
  typedef struct {
  double coord[3];
  double k[3];
  } data;
  typedef struct {
  double constants[8];
  } param;

  // intersect_Parab_Cyl function calculates the intersection point
       on a surface of a parabolic cylinder with the photon's
      trajectory, estimates two points of intersection (if only) and
       chooses the one that lies within the interval (-yheight/2<=y
      =<yheight/2 && -xwidth/2<=x=<xwidth/2) and returns it.

  data intersect_Parab_Cyl(data a, param b){
    data result={a.coord[0],a.coord[1],a.coord[2],a.k[0],a.k[1],a.k
        [2]};
    int i;
    double A,B,C,D,r;
    double t[2],p[3],knorm[3],k[3],Knorm,p_tmp[3],p1_tmp[3];
    double Sign,d,M;

    double N[3],Nx,Ny,Nz,Nnorm;
    double Arg,s,q,alpha,beta;
    double k_new[3];
    double cos_theta,cos_theta1;
    double yheight,xwidth;
    double rough_xy,rough_z;

    for(i=0;i<=2;i++){
      k[i]=a.k[i];
      p[i]=a.coord[i];
    }

    Knorm=sqrt(k[0]*k[0]+k[1]*k[1]+k[2]*k[2]);
    knorm[0]=k[0]/Knorm;
    knorm[1]=k[1]/Knorm;
    knorm[2]=k[2]/Knorm;

    r=b.constants[0];
    yheight=b.constants[1];
    xwidth=b.constants[2];
    d=b.constants[3];
    M=b.constants[4];
    Sign=b.constants[5];

    rough_xy=b.constants[6];
    rough_z=b.constants[7];

```

```
92      A=knorm[1]*knorm[1];
93      B=2*(p[1]*knorm[1]-Sign*r*knorm[2]);
94      C=p[1]*p[1]-Sign*2*r*p[2]+Sign*d*2*r;
95      D=B*B-4.0*A*C;
96
97      if (D<0) {
98          // ray does not intersect the parabola
99          fprintf(stderr,"line 89: D<0 %s\n",NAME_CURRENT_COMP);
100         return result;
101       }
102     if (A==0){
103       // incident k-vector is parallel (exactly) to the z-axis.
              Thus, the eq. becomes linear
104       if (B==0){ fprintf(stderr, "line 92: Division by zero in %s\n
              ",NAME_CURRENT_COMP); return;}
105       t[0]=-C/B;
106       for (i=0;i<=2;i++){
107         result.coord[i]=p[i]+t[0]*knorm[i];
108       }
109     } else {
110       double qq;
111       if (B<0){
112         qq=-0.5*(B-sqrt(D));
113         }else{
114           qq=-0.5*(B+sqrt(D));
115         }
116         t[0]=qq/A;
117         t[1]=C/qq;
118
119       for(i=0;i<=2;i++){
120         p_tmp[i]=p[i]+t[0]*knorm[i];
121         p1_tmp[i]=p[i]+t[1]*knorm[i];
122       }
123
124       if ( fabs(p_tmp[1])<=fabs(yheight/2) && fabs(p_tmp[0])<=fabs(
              xwidth/2) ){
125         for(i=0;i<=2;i++){
126           result.coord[i]=p_tmp[i];
127         }
128       } else if ( fabs(p1_tmp[1])<=fabs(yheight/2) && fabs(p1_tmp
              [0])<=fabs(xwidth/2) ){
129         for(i=0;i<=2;i++){
130           result.coord[i]=p1_tmp[i];
131         }
132       } else return result;
133       }
134
135     // introducing waviness into the code
136     double d_xy, d_z;
137
138     d_xy=rough_xy*randnorm();
139     d_z=rough_z*randnorm();
140
141     Nx=0;
142     if (result.coord[1]==0){              Ny=1;    Nz=0;
143     } else if (result.coord[1]!=0) {      Ny=Sign*r/result.coord[1];
            Nz=1;
144     }
145     if (rough_xy) {
```

```
146             Ny+=d_xy;
147         }
148         if (rough_z) {
149             Nz+=d_z;
150         }
151
152         Nnorm=sqrt(Nx*Nx+Ny*Ny+Nz*Nz);
153         N[0]=Nx/Nnorm;
154         N[1]=Ny/Nnorm;
155         N[2]=Nz/Nnorm;
156
157         cos_theta=N[0]*knorm[0]+N[1]*knorm[1]+N[2]*knorm[2];
158         cos_theta1=M*cos_theta;    // Snell's law
159
160         // new k vector
161         if ((1.0-cos_theta*cos_theta)==0) {
162            fprintf(stderr,"line 134: Division by zero\n"); return; }
163
164         Arg=(1.0-cos_theta1*cos_theta1)/(1.0-cos_theta*cos_theta);
165         s=(1/M)*sqrt(Arg);
166         q=(Knorm/Nnorm)*((1/M)*cos_theta1-s*cos_theta);
167
168         k_new[0]=q*Nx+s*k[0];
169         k_new[1]=q*Ny+s*k[1];
170         k_new[2]=q*Nz+s*k[2];
171
172         for(i=0;i<3;i++) {
173           result.k[i]=k_new[i];
174         }
175
176       return result;
177     }
178     const double Re=2.8179402894e-5;      // Thomson Scattering length
            [Angstrom]
179     const double Na=6.02214179e23;        // Avogadro's number [atoms
            per gram-mole]
180   %}
181
182   DECLARE
183   %{
184     struct datastruct *prms;
185   %}
186
187   INITIALIZE
188   %{
189         int status=0;
190     t_Table T;
191     if ( (status=Table_Read(&T,material_datafile,0))==-1){
192         fprintf(stderr,"Error: Could not parse file \"%s\" in COMP %s\n
            ",material_datafile,NAME_CURRENT_COMP);
193         exit(-1);
194     }
195     char **header_parsed;
196     header_parsed=Table_ParseHeader(T.header,"Z","A[r]","rho",NULL);
197     prms=calloc(1,sizeof(struct datastruct));
198     if (!prms->Z) prms->Z=strtol(header_parsed[0],NULL,10);
199     if (!prms->Ar) prms->Ar=strtod(header_parsed[1],NULL);
200     if (!prms->rho) prms->rho=strtod(header_parsed[2],NULL);
201     prms->E=malloc(sizeof(double)*(T.rows+1));
```

```
  prms->f=malloc(sizeof(double)*(T.rows+1));
  prms->mu=malloc(sizeof(double)*(T.rows+1));
  int i;
  for(i=0;i<T.rows;i++){
      prms->E[i]=T.data[i*T.columns];
      prms->mu[i]=T.data[5+i*T.columns]*prms->rho*1e2;      // mu is now in SI, [m^-1]
      prms->f[i]=T.data[1+i*T.columns];
  }
  Table_Free(&T);

%}

TRACE
%{
   // calculation of the parabolic parameters
  param parab_Cyl;
  data incid,refr,outg;

  int i=0,nr;
  double w;
  double E,mu,f,rhoel,dl,e,k,delta,beta,Refractive_Index_Re,Refractive_Index_Im;

  w=(yheight*yheight)/(8.0*r); //calculation of the "depth" of the profile

  if ((yheight/2)<r){
    fprintf(stderr,"Error: the aperture must be greater than radius of curvature in the %s\n",NAME_CURRENT_COMP);
    exit(-1);
  }

  parab_Cyl.constants[0]=r;
  parab_Cyl.constants[1]=yheight;
  parab_Cyl.constants[2]=xwidth;

  parab_Cyl.constants[6]=rough_xy;
  parab_Cyl.constants[7]=rough_z;

  k=sqrt(kx*kx+ky*ky+kz*kz);
  e=K2E*k;  // Energy in KeV, same unit as datafile

  // Interpolation of Table Values

  while (e>prms->E[i]){
    i++;
    if (prms->E[i]==-1){
      fprintf(stderr,"Photon energy (%g keV) is outside of the lens' material data\n",k); ABSORB;
    }
  }
  E=(e-prms->E[i-1])/(prms->E[i]-prms->E[i-1]);
  mu=(1-E)*prms->mu[i-1]+E*prms->mu[i];
  //mu= 1e-10*mu;  // factor conversion from m^-1 to A^-1
  f=(1-E)*prms->f[i-1]+E*prms->f[i];

  // Calculation of Refractive Index

```

```
rhoel= f*Na*(prms->rho*1e-24)/prms->Ar;     // Material's Number Density of Electrons [e/A^3] incl f' scattering length correction
if (deltaN==0) {
    delta= 2.0*M_PI*Re*rhoel/(k*k);
} else delta=deltaN;
//beta=mu/(2.0*k);            // mu and k in  A^-1
//delta=3.40754082e-6; Oleg's value for Be at 10 keV

Refractive_Index_Re = 1.0-delta;
// Refractive_Index_Im = beta;

incid.k[0]=kx;
incid.k[1]=ky;
incid.k[2]=kz;

incid.coord[0]=x;
incid.coord[1]=y;
incid.coord[2]=z;

for (nr=0;nr<=(N-1);nr++){
  parab_Cyl.constants[3]=nr*d+nr*2*w; // d constant
  parab_Cyl.constants[4]=1.0/Refractive_Index_Re; // M constant
  parab_Cyl.constants[5]=-1.0; // Sign constant

  refr=intersect_Parab_Cyl(incid,parab_Cyl);

  if(refr.k[0]==0 && refr.k[1]==0 && refr.k[2]==0) continue;

  dl=sqrt( (refr.coord[0]-x)*(refr.coord[0]-x) + (refr.coord[1]-y)*(refr.coord[1]-y) + (refr.coord[2]-z)*(refr.coord[2]-z) );
  PROP_DL(dl);
  SCATTER;

  kx=refr.k[0];
  ky=refr.k[1];
  kz=refr.k[2];
  // alter parabolic input to match second parabola

  parab_Cyl.constants[3]=(nr+1)*d+nr*2*w;
  parab_Cyl.constants[4]=Refractive_Index_Re;
  parab_Cyl.constants[5]=1.0;

  outg=intersect_Parab_Cyl(refr,parab_Cyl);

  dl=sqrt( (outg.coord[0]-x)*(outg.coord[0]-x) + (outg.coord[1]-y)*(outg.coord[1]-y) + (outg.coord[2]-z)*(outg.coord[2]-z) );
  PROP_DL(dl);
  SCATTER;

  kx=outg.k[0]; ky=outg.k[1]; kz=outg.k[2];
  incid=outg;
 }

  // transmission calculation
  double mu_rho, ap;

  mu_rho=mu/(prms->rho*1e2); // mass absorption coefficient [cm2]

```

```
      ap=mu_rho*((parab_Cyl.constants[0]*N*delta*prms->Ar*k*k)/(M_PI*
          Na*Re*1e-10*(prms->Z+f)))*1e16; //1e16 -dimension
          coefficient
      // ap - effective aperture

     if (T==0)
        ABSORB;
     else
     T=exp(-mu*N*d)*(1/(2*ap))*(1-exp(-2*ap));

     p*=T;

%}

MCDISPLAY
%{
   magnify("xy");
   double z_c,zdepth,w;
   w=(yheight*yheight)/(8*r);
   zdepth=N*(2*w+d);
   z_c=(zdepth/2.0)-w;
   box(0,0,z_c,yheight/2,yheight/2,zdepth);
%}

END
```

```
/*******************************************************
*
* McXtrace, X-ray tracing package
*         Copyright, All rights reserved
*         Risoe National Laboratory, Roskilde, Denmark
*         Institut Laue Langevin, Grenoble, France
*         University of Copenhagen, Copenhagen, Denmark
*
* Component: Lens_parab_rough
*
* Written by: Jana Baltser and Erik Knudsen
*
* Date: August 2010, modified July 2011
* Version: 1.0
* Release: McXtrace 0.1
* Origin: NBI
*
* A simple X-ray compound refractive lens (CRL) with a profile of the parabola in rotation simulates the photons' movement on passing through it. The CRL focuses in 2D
*
* Input parameters:
* r - raduis of curvature (circular approximation at the tip of the profile) [mm];
* yheight - the CRL's dimensions along Y, aka aperture[mm];
* xwidth - the CRL's dimensions along X [mm];
* d - distance between two surfaces of the lens along the propagation axis;
* N - amount of single lenses in a stack.
* T - transmission of the lens
* rough_xy [rms] - waviness along x and y
* rough_z [rms] -waviness along z
* deltaN- auxiliary parameter = delta*Number of lenses, valuable in cases when applying thin lens approximation to thick lens properties.
*
* attenuation coefficient mu is taken from the NIST database and
* Be.txt
*
*******************************************************/


DEFINE COMPONENT Lens_parab_rough
DEFINITION PARAMETERS (string material_datafile="Be.txt")
SETTING PARAMETERS (r=0.5e-3,yheight=1.4e-3,xwidth=1.4e-3,d=.1e-3,T=.99,N=1,deltaN=0,rough_z=0,rough_xy=0)
OUTPUT PARAMETERS (prms,parab)
STATE PARAMETERS (x,y,z,kx,ky,kz,phi,t,Ex,Ey,Ez,p)

SHARE
%{
  %include "read_table-lib"
  struct datastruct{
    int Z;
    double Ar, rho;
    double *E, *mu, *f;
  };
  typedef struct {
```

```
  double coord[3];
  double k[3];
  } incom;
typedef struct {
  double constants[8];
} lens;

  incom intersection(incom a,lens b){
    incom result={a.coord[0],a.coord[1],a.coord[2],a.k[0],a.k[1],a.k[2]};
    int i;
    double A,B,C,D,r;
    double t[2],p[3],knorm[3],k[3],pos1_tmp[3],pos_tmp[3];

    double nxn,nyn,nzn,Nx,Ny,Nz,NORM,Knorm;
    double cos_theta,cos_theta1,Arg,Arg1,s,q;
    double k_new[3],k_new1[3],M,Sign,d;
    double yheight,xwidth;

    double tx,ty,tz,tnorm,txn,tyn,tzn;
    double v,w;
    double rough_xy,rough_z;

    for(i=0;i<=2;i++){
      k[i]=a.k[i];
      p[i]=a.coord[i];
    }

    Knorm=sqrt(k[0]*k[0]+k[1]*k[1]+k[2]*k[2]);
    knorm[0]=k[0]/Knorm;
    knorm[1]=k[1]/Knorm;
    knorm[2]=k[2]/Knorm;

    r=b.constants[0];
    yheight=b.constants[1];
    xwidth=b.constants[2];
    d=b.constants[3];
    M=b.constants[4];
    Sign=b.constants[5];

    rough_xy=b.constants[6];
    rough_z=b.constants[7];

    A=knorm[0]*knorm[0]+knorm[1]*knorm[1];
    B= 2.0*(p[0]*knorm[0]+p[1]*knorm[1] - Sign*r*knorm[2]);
    C=p[0]*p[0]+p[1]*p[1] - Sign*2*r*p[2] + Sign*r*2*d;
    D=B*B-4.0*A*C;

    if (D<0) { //ray does not intersect the parabola
        fprintf(stderr,"line 96: D<0 %s\n",NAME_CURRENT_COMP);
        return result;
    }
    if (A==0){ //incident k-vector is parallel (exactly) to the z-axis. Thus, the eq. becomes linear
      if(B==0){
        fprintf(stderr, "Division by zero in %s\n",NAME_CURRENT_COMP);
        return;
      }
```

```
      t[0]=-C/B;
      for(i=0; i<=2; i++){
        result.coord[i]=p[i]+t[0]*knorm[i];
      }
    } else {
      double qq;
        if (B<0){
          qq=-0.5*(B-sqrt(D));
        }else{
          qq=-0.5*(B+sqrt(D));
        }
        t[0]=qq/A;
        t[1]=C/qq;

        for(i=0;i<=2;i++){
          pos_tmp[i]=p[i]+t[0]*knorm[i];
          pos1_tmp[i]=p[i]+t[1]*knorm[i];
        }
        if ( fabs(pos_tmp[1])<=fabs(yheight/2) && fabs(pos_tmp[0])
            <=fabs(xwidth/2) ){
          for(i=0;i<=2;i++){
          result.coord[i]=pos_tmp[i];
          }
        } else if ( fabs(pos1_tmp[1])<=fabs(yheight/2) && fabs(
            pos1_tmp[0])<=fabs(xwidth/2) ){
                for(i=0;i<=2;i++){
                    result.coord[i]=pos1_tmp[i];
                }
          }
        else return result;
      }

    // introducing waviness into the code
    double d_xy, d_z;

    d_xy=rough_xy*randnorm();
    d_z=rough_z*randnorm();

        // Calculating tangential vector

    if (result.coord[0]==0 && result.coord[1]==0){ // incoming ray
        is along the axis, so it does not refract
        k_new[0]=k[0];
        k_new[1]=k[1];
        k_new[2]=k[2];
         for(i=0;i<3;i++) {
         result.k[i]=k_new[i];
         }
      return result;
    }
    else if (result.coord[0]!=0 && result.coord[1]!=0){
           Nx=-Sign*(result.coord[0]/r);  // surface normal
           Ny=-Sign*(result.coord[1]/r);
           Nz=1;

               if (rough_xy) {
                 Nx+=d_xy;
                 Ny+=d_xy;
               }
```

```
164                 if (rough_z) {
165                     Nz+=d_z;
166                 }
167
168
169             NORM=sqrt(Nx*Nx+Ny*Ny+Nz*Nz);
170             nxn=Nx/NORM;
171             nyn=Ny/NORM;
172             nzn=Nz/NORM;
173
174             double cos_chi;
175             cos_chi=knorm[0]*nxn+knorm[1]*nyn+knorm[2]*nzn;
176             w=1/(sqrt(1-cos_chi*cos_chi)); // tangential vector
177             v=-w*cos_chi;
178
179             tx=v*nxn+w*knorm[0];
180             ty=v*nyn+w*knorm[1];
181             tz=v*nzn+w*knorm[2];
182
183     }
184     else if (result.coord[0]==0){
185             tx=0;
186             ty=Sign*(r/result.coord[1]);
187             tz=1;
188     }
189     else if (result.coord[1]==0){
190             tx=Sign*(r/result.coord[0]);
191             ty=0;
192             tz=1;
193     }
194
195     tnorm=sqrt(tx*tx+ty*ty+tz*tz);
196     txn=tx/tnorm;
197     tyn=ty/tnorm;
198     tzn=tz/tnorm;
199
200     cos_theta=txn*knorm[0]+tyn*knorm[1]+tzn*knorm[2];
201     cos_theta1=M*cos_theta; // Snell's law
202
203     // new k vector
204     if ((1.0-cos_theta*cos_theta)==0) {
205        fprintf(stderr,"line 134: Division by zero\n");
206        return;
207     }
208
209     Arg=(1.0-cos_theta1*cos_theta1)/(1.0-cos_theta*cos_theta);
210     s=(1/M)*sqrt(Arg);
211     q=(Knorm/tnorm)*((1/M)*cos_theta1-s*cos_theta);
212
213     k_new[0]=q*tx+s*k[0];
214     k_new[1]=q*ty+s*k[1];
215     k_new[2]=q*tz+s*k[2];
216
217     for(i=0;i<3;i++) {
218       result.k[i]=k_new[i];
219     }
220     return result;
221   }
222
```

```
  const double Re=2.8179402894e-5;      // Thomson Scattering length [Angstrom]
  const double Na=6.02214179e23;        // Avogadro's number [atoms per gram-mole]
%}

DECLARE
%{
  struct datastruct *prms;
%}

INITIALIZE
%{
  int status=0;
  t_Table T;
  if ( (status=Table_Read(&T,material_datafile,0))==-1){
    fprintf(stderr,"Error: Could not parse file \"%s\" in COMP %s\n",material_datafile,NAME_CURRENT_COMP);
    exit(-1);
  }
  char **header_parsed;
  header_parsed=Table_ParseHeader(T.header,"Z","A[r]","rho",NULL);
  prms=calloc(1,sizeof(struct datastruct));
  if (!prms->Z) prms->Z=strtol(header_parsed[0],NULL,10);
  if (!prms->Ar) prms->Ar=strtod(header_parsed[1],NULL);
  if (!prms->rho) prms->rho=strtod(header_parsed[2],NULL);
  prms->E=malloc(sizeof(double)*(T.rows+1));
  prms->f=malloc(sizeof(double)*(T.rows+1));
  prms->mu=malloc(sizeof(double)*(T.rows+1));
  int i;
  for(i=0;i<T.rows;i++){
      prms->E[i]=T.data[i*T.columns];
      prms->mu[i]=T.data[5+i*T.columns]*prms->rho*1e2;      //mu is now in SI, [m^-1]
      prms->f[i]=T.data[1+i*T.columns];
  }
  Table_Free(&T);
%}




TRACE
%{
  incom incid,refr,outg;
  lens parab;

  double E,mu,f,rhoel,dl,e,k,delta,beta,Refractive_Index_Re,Refractive_Index_Im,w;

  int i=0,nr;

  parab.constants[0]=r;
  parab.constants[1]=yheight;
  parab.constants[2]=xwidth;

  parab.constants[6]=rough_xy;
  parab.constants[7]=rough_z;

```

```
  w=(yheight*yheight)/(8.0*r);
  k=sqrt(kx*kx+ky*ky+kz*kz);
  e=K2E*k;  //Energy in KeV, same unit as datafile

//Interpolation of Table Values

  while (e>prms->E[i]){
    i++;
    if (prms->E[i]==-1){
      fprintf(stderr,"Photon energy (%g keV) is outside of the lens ' material data\n",e); ABSORB;
    }
  }
  E=(e-prms->E[i-1])/(prms->E[i]-prms->E[i-1]);
  mu=(1-E)*prms->mu[i-1]+E*prms->mu[i];
  //mu= 1e-10*mu;  //factor conversion from m^-1 to A^-1
  f=(1-E)*prms->f[i-1]+E*prms->f[i];

  //Calculation of Refractive Index

  rhoel= f*Na*(prms->rho*1e-24)/prms->Ar;     //Material's Number Density of Electrons [e/A^3] incl f' scattering length correction

  if (deltaN==0){
    delta= 2.0*M_PI*Re*rhoel/(k*k);
  } else delta=deltaN;
  //beta=mu/(2.0*k);            //mu and k in  A^-1
  //printf("Delta=%g\n",delta);
  Refractive_Index_Re = 1.0-delta;
  //Refractive_Index_Im = beta;

  //Ray Tracing

  incid.k[0]=kx;
  incid.k[1]=ky;
  incid.k[2]=kz;

  incid.coord[0]=x;
  incid.coord[1]=y;
  incid.coord[2]=z;

  for (nr=0;nr<=(N-1);nr++){
    parab.constants[3]=nr*d+nr*2*w; // d constant
    parab.constants[4]=1.0/Refractive_Index_Re; // M constant
    parab.constants[5]=-1.0; // Sign constant

    refr=intersection(incid,parab);

    if(refr.k[0]==0 && refr.k[1]==0 && refr.k[2]==0) continue;

    dl=sqrt( (refr.coord[0]-x)*(refr.coord[0]-x) + (refr.coord[1]-y)*(refr.coord[1]-y) + (refr.coord[2]-z)*(refr.coord[2]-z) );
    PROP_DL(dl);
    SCATTER;

    kx=refr.k[0];
    ky=refr.k[1];
    kz=refr.k[2];
```

```
      //alter parabolic input to match second parabola

      parab.constants[3]=(nr+1)*d+nr*2*w;
      parab.constants[4]=Refractive_Index_Re;
      parab.constants[5]=1.0;

      outg=intersection(refr,parab);

      dl=sqrt( (outg.coord[0]-x)*(outg.coord[0]-x) + (outg.coord[1]-y
          )*(outg.coord[1]-y) + (outg.coord[2]-z)*(outg.coord[2]-z) );
      PROP_DL(dl);
      SCATTER;

      kx=outg.k[0]; ky=outg.k[1]; kz=outg.k[2];
      incid=outg;
    }
    // transmission calculation
      double mu_rho, ap;

      mu_rho=mu/(prms->rho*1e2); // mass absorption coefficient [cm2]

      ap=mu_rho*((parab.constants[0]*N*delta*prms->Ar*k*k)/(M_PI*Na*
          Re*1e-10*(prms->Z+f)))*1e16; //1e16 -dimension coefficient
      // ap - effective aperture

     if (T==0)
        ABSORB;
     else
       T=exp(-mu*N*d)*(1/(2*ap))*(1-exp(-2*ap));
     p*=T;

%}

MCDISPLAY
%{
   magnify("xy");
   double z_c,zdepth,w;
   w=(yheight*yheight)/(8*r);
   zdepth=N*(2*w+d);
   z_c=zdepth/2.0-w;
   box(0,0,z_c,yheight/2,yheight/2,zdepth);
%}

END
```

```
/*******************************************************
*
* McXtrace, X-ray tracing package
*         Copyright, All rights reserved
*         Risoe National Laboratory, Roskilde, Denmark
*         Institut Laue Langevin, Grenoble, France
*         University of Copenhagen, Copenhagen, Denmark
*
* Component: Lens_Kinoform
*
* Written by: Jana Baltser and Erik Knudsen
*
* Date: January 2012
* Version: 1.0
* Release: McXtrace 0.1
* Origin: NBI
*
* KINOFORM. A model of a specific kinoform used by the BNL team during the APS beamtime.
*       z: [0 0.002033m]
*       xmin=-0.0002634
*       xmax=0.0002634
*       y - height of the lens.
* the principles of the kinoform's operation are described here: http://neutrons.ornl.gov/workshops/nni_05/presentations/min050616_xray_evans-lutterodt_ken_nni05.pdf
*
*
*************************************************************/

DEFINE COMPONENT Lens_Kinoform
DEFINITION PARAMETERS (string datafile="kinoform.txt", material_datafile="Si.txt",Re=2.8179402894e-5,Na=6.02214179e23)
SETTING PARAMETERS (yheight=1e-2,xwidth=5.268e-4,deltaN=0)
OUTPUT PARAMETERS (prms,mat_data)

SHARE
%{
  %include "read_table-lib"
  struct KL_struct{
    double *z_KL, *x_KL;
  };

  struct data{
    int Z;
    double Ar, rho;
    double *E, *mu, *f;
  };

//  const double Re=2.8179402894e-5;      // Thomson Scattering length [Angstrom]
//  const double Na=6.02214179e23;        // Avogadro's number [atoms per gram-mole]
%}

DECLARE
%{
  struct KL_struct *prms;
```

```
  struct data *mat_data;
%}

INITIALIZE
%{
  // parsing the geometrical dimensions file
  int status=0;
  t_Table T;
  if ( (status=Table_Read(&T,datafile,0))==-1){
    fprintf(stderr,"Error: Could not parse file \"%s\" in COMP %s\n",datafile,NAME_CURRENT_COMP);
    exit(-1);
  }
  prms=calloc(1,sizeof(struct KL_struct));
  prms->z_KL=malloc(sizeof(double)*(T.rows+1));
  prms->x_KL=malloc(sizeof(double)*(T.rows+1));
  int i;
  for(i=0;i<T.rows;i++){
      prms->z_KL[i]=T.data[i*T.columns];
      prms->x_KL[i]=T.data[1+i*T.columns];

  }
  Table_Free(&T);


  // parsing the material datafile
  int st=0;
  t_Table TT;
  if ( (st=Table_Read(&TT,material_datafile,0))==-1){
    fprintf(stderr,"Error: Could not parse file \"%s\" in COMP %s\n",material_datafile,NAME_CURRENT_COMP);
    exit(-1);
  }
  char **header_parsed;
  header_parsed=Table_ParseHeader(TT.header,"Z","A[r]","rho",NULL);
  mat_data=calloc(1,sizeof(struct data));
  if (!mat_data->Z) mat_data->Z=strtol(header_parsed[0],NULL,10);
  if (!mat_data->Ar) mat_data->Ar=strtod(header_parsed[1],NULL);
  if (!mat_data->rho) mat_data->rho=strtod(header_parsed[2],NULL);
  mat_data->E=malloc(sizeof(double)*(TT.rows+1));
  mat_data->f=malloc(sizeof(double)*(TT.rows+1));
  mat_data->mu=malloc(sizeof(double)*(TT.rows+1));
  int nr;
  for(nr=0;nr<TT.rows;nr++){
      mat_data->E[nr]=TT.data[nr*TT.columns];
      mat_data->mu[nr]=TT.data[5+nr*TT.columns]*mat_data->rho*1e2;  //mu is now in SI, [m^-1]
      mat_data->f[nr]=TT.data[1+nr*TT.columns];
  }
  Table_Free(&TT);
%}

TRACE
%{
  double F,k,di;
  double kxN,kyN,kzN;
  double E, mu,f,rhoel,e,delta,beta,T;
  double x_tmp,z_int;
  int i,nr;
```

```
k=sqrt(kx*kx+ky*ky+kz*kz);
e=K2E*k;

// determining delta

while (e>mat_data->E[i]){
  i++;
  if (mat_data->E[i]==-1){
    fprintf(stderr,"Photon energy (%g keV) is outside of the kinoform's material data\n",k); ABSORB;
  }
}
E=(e-mat_data->E[i-1])/(mat_data->E[i]-mat_data->E[i-1]);
mu=(1-E)*mat_data->mu[i-1]+E*mat_data->mu[i];
f=(1-E)*mat_data->f[i-1]+E*mat_data->f[i];
rhoel= f*Na*(mat_data->rho*1e-24)/mat_data->Ar;

if (deltaN==0) {
    delta= 2.0*M_PI*Re*rhoel/(k*k);
} else delta=deltaN;
mu*=1e-10; // factor conversion from m^-1 to A^-1
beta=mu/(2.0*k);

PROP_Z0;

if (x> -xwidth/2 && x< xwidth/2 &&
    y> -yheight/2 && y< yheight/2){
          //Interpolation of Table Values

        while (fabs(x)>prms->x_KL[nr]){
            nr++;
            if (nr<=1) nr=1;
            if (nr>=1345) nr=1345;
            if (prms->x_KL[nr]==-1){
                fprintf(stderr,"An error with parsing the kinoform dimensions' file\n"); ABSORB;
            }
        }
  x_tmp=prms->x_KL[nr]; z_int=prms->z_KL[nr];

  PROP_DL(z_int);
  SCATTER;

  F=((x*x)/(2*delta*z)) - (((2*delta-delta*delta)*z)/(2*delta));

  di=sqrt(x*x+(z-F)*(z-F)); // distance to the focal point with the subsequent calculation of a new k vector
  kxN=-(k*x)/di;
  kyN=0;
  kzN=(k*(F-z))/di;

  double knew_x,knew_y,knew_z;
  double NN,Nx,Ny,Nz,aa, aa1;

  NN=sqrt(kxN*kxN+kyN*kyN+kzN*kzN);
  Nx=kxN/NN;
  Ny=kyN/NN;
  Nz=kzN/NN;

```

```
    aa=Nz;
    aa1=sqrt(1-aa*aa);
    // Rotation of the incoming k vector by an angle alpha:

    if (x<0){
            knew_x=aa*kx+aa1*kz;          // rotation around Y axis
            knew_y=ky;
            knew_z=-aa1*kx+aa*kz;
    } else if (x>0){
      knew_x=-aa*kx+aa1*kz;
      knew_y=ky;
      knew_z=-aa1-aa*kz;
    }

    kx=knew_x;
    ky=knew_y;
    kz=knew_z;


  } else
  SCATTER;

    // transmission calculation
   T=exp(-2*M_PI*(beta/delta));
   p*=T;

%}

MCDISPLAY
%{
  magnify("xy"); // zdepth=0.002033
  double zdepth=0.002033,w;
  w=xwidth/2;
  box(0,0,zdepth,w,yheight/2,zdepth);
%}

END
```

```
/*******************************************************
*
* McXtrace, X-ray tracing package
*          Copyright, All rights reserved
*          Risoe National Laboratory, Roskilde, Denmark
*          Institut Laue Langevin, Grenoble, France
*          University of Copenhagen, Copenhagen, Denmark
*
* Component: KB_Multilayer_mirror
*
* %I
*
* Written by: Jana Baltser, Anette Vickery, Erik Knudsen, Jesper Buch Jensen, Peter Willendrup, Andrea Prodi
* Date: February 2013
* Version: 1.0
* Release: McXtrace 0.1
* Origin: NBI
*
* Elliptic multilayer mirror
*
* Reads reflectivity values from a data input file (Ref.dat) for a W/B4C multilayer.
* The multilayer code reflects ray in an ideal geometry, the reflectivity datafile accounts for surface roughness, sigma.
* Reflectivity coefficient is applied in the end of the code. An additional datafile stores a correlation between the z-coordinate of the photon's intersection point and the d spacing of the multilayer.
*
* The mirror is positioned such that the long axis of the mirror elliptical surface coincides with
* z-axis
*
* %D
* The algorithm:
*  Incoming photon's coordinates and direction (k-vector) are transformed into an elliptical reference frame
* (elliptical parameters are calculated according to the mirror's position and its focusing distances and the  * incident angle), the intersection point is then defined. A new, reflected photon is then starting at the
* point of intersection.
*
*
*
* %P
* Input parameters:
* theta [degrees] - incident angle
* s1 [m] - distance from the source to the multilayer
* s2 [m] - focusing distance of the multilayer
* length [m] - length of the mirrors
* width [m] - width of the mirror along x-axis
* R0 - reflectivity, R0=1 for an ideal situation, otherwise R0=0 - the code reads the reflectivity from the datafile
*
* (none)
*
```

```
* %E
*******************************************************/

DEFINE COMPONENT TwinKB_ML_v2
DEFINITION PARAMETERS (string reflectivity_datafile="Ref.txt",
    string curvature_datafile="Coord_d_ang.txt")
SETTING PARAMETERS (theta=1.2,s1,s2,length=0.6,width=0.2,R0=0)
OUTPUT PARAMETERS (prms_m, a,b,c,M,Z0,Y0,xi,cost0)

SHARE
%{
   %include "read_table-lib"

  struct ML_curv{
     double *Coord;      //z-coordinate of the intersection point (
         theta)
     double *d_sp;       // d_spacing
     double *ang;
   };

  struct data{
     double *Q;
     double **R;
   };

  /*something that would be relevant for ALL elliptical mirrors*/
  /* coordinate transformation McXtrace-Ellipse (ME) and Ellipse-
      McXtrace(EM) functions */
  void CoordTransME(double *x_el, double *y_el, double *z_el,
                    double x0, double y0, double z0, double Zmir,
                        double Ymir, double xi_mir)
  {
   *x_el=x0;
   *y_el= cos(xi_mir)*y0+sin(xi_mir)*z0+Ymir;
   *z_el=-sin(xi_mir)*y0+cos(xi_mir)*z0+Zmir;
  }

  void CoordTransEM(double *x_gen, double *y_gen,double *z_gen,
                    double x0, double y0, double z0, double Zmir,
                        double Ymir,double xi_mir)
  {
   *x_gen=x0;
   *y_gen= cos(xi_mir)*(y0-Ymir)-sin(xi_mir)*(z0-Zmir);
   *z_gen= sin(xi_mir)*(y0-Ymir)+cos(xi_mir)*(z0-Zmir);
  }

%}

DECLARE
%{
  double a,b,c,M,Z0,Y0,xi,cost0;
  struct ML_curv *ml_surf;
  struct data *ml_refl;
  Rotation Q1,Q2;

%}

INITIALIZE
%{
```

```
/* calculation of the elliptical parameters according to the input mirror parameters:
ellipse major axis a/2, minor axis b/2, M-magnification factor, Z0&Y0 - position of the mirror centre in the elliptical coordinate system.*/
double Theta=DEG2RAD*theta;

M=s2/s1;
cost0 = (1-M)/sqrt(1-2*M + M*M + 4*M*(cos(Theta)*cos(Theta)));
a = (s1*sqrt(1-cost0*cost0+cos(Theta)*cos(Theta)*cost0*cost0))/(cost0*cos(Theta)+sqrt(1-cost0*cost0+ (cos(Theta)*cos(Theta))*cost0*cost0));
c = a*cos(Theta)/sqrt(1-cost0*cost0+(cos(Theta)*cos(Theta))*cost0*cost0);
b = sqrt(a*a-c*c);
Z0 = a*cost0;
Y0 = -b*sin(acos(cost0));
xi = -atan((Z0*b*b)/(Y0*a*a));


  // surface datafile parsing
int st=0;
t_Table TT;
if ((st=Table_Read(&TT, curvature_datafile,0))==-1){
  fprintf(stderr,"Error: Could not parse the curvature data file \"%s\" in COMP %s\n",curvature_datafile,NAME_CURRENT_COMP);
  exit(-1);
}
ml_surf=malloc(sizeof(struct ML_curv));
(ml_surf->Coord)=malloc(sizeof(double)*(TT.rows+1));
(ml_surf->d_sp)=malloc(sizeof(double)*(TT.rows+1));
(ml_surf->ang)=malloc(sizeof(double)*(TT.rows+1));
  int nr;
  for (nr=0;nr<TT.rows;nr++){
     ml_surf->Coord[nr]=TT.data[nr*TT.columns];
     ml_surf->d_sp[nr]=TT.data[1+nr*TT.columns];
     ml_surf->ang[nr]=TT.data[2+nr*TT.columns];
  }
  Table_Free(&TT);

  // reflectivity datafile parsing
int status=0;
t_Table t;
if ((status=Table_Read(&t, reflectivity_datafile,0))==-1){
  fprintf(stderr,"Error: Could not parse the reflectivity data file \"%s\" in COMP %s\n",reflectivity_datafile,NAME_CURRENT_COMP);
  exit(-1);
}
ml_refl=malloc(sizeof(struct data));
(ml_refl->R)=malloc(sizeof(double *)*(t.rows));
(ml_refl->Q)=malloc(sizeof(double)*(t.rows));
  int i,j;
  for (i=0;i<t.rows;i++){
     ml_refl->R[i]=malloc(sizeof(double)*(t.columns));
  }
  for (i=0;i<t.rows;i++){
    ml_refl->Q[i]=t.data[i*t.columns];
      for (j=0;j<t.columns;j++){
```

```
            ml_refl->R[i][j]=t.data[i*t.columns+j];
          }
      }
       Table_Free(&t);


%}

TRACE
%{
   double K,vink;
   double x_e1,y_e1,z_e1,kx_e1,ky_e1,kz_e1;       // beginning coordinates transformed into the ellipse system
   double x_e2,y_e2,z_e2,kx_e2,ky_e2,kz_e2;       // kvector transformed into the ellipse system, hence

   double A,B,C,D,l01,l11,l02,l12;
   double x_test1,y_test1,z_test1,x_test2,y_test2,z_test2,dist;  // intersection with the elliptical surface
   double nx,ny,nz;
   double kxn,kyn,kzn;            // reflected ray's kvector

   int status1,status2,bounce;

   /* get the photon's coordinates and kvector in the ellipse frame */
   K=sqrt(kx*kx+ky*ky+kz*kz);

   bounce=CHAR_MAX;
   while (bounce){

      bounce=0;
      /*switch to the ellipsoid frames. Note that the order of x and y has been swapped in the second set of calls*/
      CoordTransME(&x_e1,&y_e1,&z_e1,x,y,z,Z0,Y0,xi);
      CoordTransME(&kx_e1,&ky_e1,&kz_e1,kx,ky,kz,0,0,xi);
      NORM(kx_e1,ky_e1,kz_e1);
      CoordTransME(&y_e2,&x_e2,&z_e2,y,x,z,Z0,Y0,xi);
      CoordTransME(&ky_e2,&kx_e2,&kz_e2,ky,kx,kz,0,0,xi);
      NORM(kx_e2,ky_e2,kz_e2);
#ifdef MCDEBUG
      printf("coord transform1: r=(%g %g %g) k=(%g %g %g) => r=(%g %g %g) k=(%g %g %g) Z0,Y0=(%g,%g)\n",x,y,z,kx,ky,kz,x_e1,y_e1,z_e1,kx_e1,ky_e1,kz_e1,Z0,Y0);
      printf("coord transform2: r=(%g %g %g) k=(%g %g %g) => r=(%g %g %g) k=(%g %g %g)\n",x,y,z,kx,ky,kz,x_e2,y_e2,z_e2,kx_e2,ky_e2,kz_e2);
#endif
      double QQ[3][3]={{1,0,0},{0,1,0},{0,0,1}};
      /*compute intersections with the ellipsoid surfaces that contain the mirror surfaces
        using 1e6 as a half-axis to emulate something flat in that dimension*/
      status1=ellipsoid_intersect(&l01,&l11,x_e1,y_e1,z_e1,kx_e1,ky_e1,kz_e1,1e6,b,a,QQ);
      status2=ellipsoid_intersect(&l02,&l12,x_e2,y_e2,z_e2,kx_e2,ky_e2,kz_e2,b,1e6,a,QQ);
#define SWAP(a,b) \
      do { \
```

```
      double tmp=(a); \
      (a)=(b);(b)=tmp;\
    } while(0)\



    if (status1) {
      if (l01>0){
        double dl=l01;
        double xx,yy,zz;
        xx=x_e1+kx_e1*dl; yy=y_e1+ky_e1*dl; zz=z_e1+kz_e1*dl;
        if ((yy)<=0 && xx>0 && xx<width && fabs(zz-Z0)<length/2.0){
          ABSORB;
        }
      }
      if(l11>0){
        double dl=l11;
        double xx,yy,zz;
        xx=x_e1+kx_e1*dl; yy=y_e1+ky_e1*dl; zz=z_e1+kz_e1*dl;
        if ((yy)<=0 && xx>0 && xx<width && fabs(zz-Z0)<length/2.0){
          if(bounce!=1){
            bounce|=1;
          }
          x_test1=xx;y_test1=yy;z_test1=zz;
        }
      }
    }

    if (status2) {
      if(l02>0){
        double dl=l02;
        double xx,yy,zz;
        xx=x_e2+kx_e2*dl; yy=y_e2+ky_e2*dl; zz=z_e2+kz_e2*dl;
        if ((xx)<=0 && yy>0 && yy<width && fabs(zz-Z0)<length/2.0){
      }
      }
      if (l12>0){
        double dl=l12;
        double xx,yy,zz;
        xx=x_e2+kx_e2*dl; yy=y_e2+ky_e2*dl; zz=z_e2+kz_e2*dl;
        if ((xx)<=0 && yy>0 && yy<width && fabs(zz-Z0)<length/2.0){
          if (bounce!=2) bounce|=2;
          x_test2=xx;y_test2=yy;z_test2=zz;
        }
      }
    }
    /*if we're about to hit both mirrors - pick the first one*/
    if (bounce==3){
      if (l11<l12){
        bounce=1;
      }else{
        bounce=2;
      }
    } else if (!bounce)
      continue;

    /*propagate to the selected mirror and reflect
      first store the old wavevector though*/
    double kxo,kyo,kzo;
```

```
256        kxo=kx;kyo=ky,kzo=kz;
257
258        if (bounce==1){
259          PROP_DL(l11);
260          SCATTER;
261          nx=0;
262          if (fabs(z_test1)<FLT_EPSILON){
263            ny=-1;
264            nz=0;
265          } else {
266            ny=(a*a*y_test1)/(b*b*z_test1);
267            nz=1.0;
268          }
269          NORM(nx,ny,nz);
270          vink=scalar_prod(nx,ny,nz,kx_e1,ky_e1,kz_e1);
271          kxn=kx_e1-2.0*vink*nx;
272          kyn=ky_e1-2.0*vink*ny;
273          kzn=kz_e1-2.0*vink*nz;
274          NORM(kxn,kyn,kzn);
275          CoordTransEM(&kx,&ky,&kz,kxn,kyn,kzn,0,0,xi);
276        }else if (bounce==2){
277          PROP_DL(l12);
278          SCATTER;
279          ny=0;
280          if (fabs(z_test2)<FLT_EPSILON){
281            nx=1;
282            nz=0;
283          } else {
284            nx=(a*a*x_test2)/(b*b*z_test2);
285            nz=1.0;
286          }
287          NORM(nx,ny,nz);
288          vink=scalar_prod(nx,ny,nz,kx_e2,ky_e2,kz_e2);
289          kxn=kx_e2-2.0*vink*nx;
290          kyn=ky_e2-2.0*vink*ny;
291          kzn=kz_e2-2.0*vink*nz;
292          NORM(kxn,kyn,kzn);
293          CoordTransEM(&ky,&kx,&kz,kyn,kxn,kzn,0,0,xi);
294        }
295
296        kx=K*kx;
297        ky=K*ky;
298        kz=K*kz;
299    #ifdef MCDEBUG
300          printf("ko=(%g %g %g)\n",kx,ky,kz);
301    #endif
302        PROP_DL(FLT_EPSILON);
303
304        // apply reflectivity
305        int g=0,r=0;
306        double co, d_sp,ang,Refl,Q,mono_energy=8.048;
307      // parsing the correlation of surface and d_spacing datafile
308        while (g<=31){
309          if (z < (ml_surf->Coord[g])) break;
310         g++;
311       }
312        if (g<1) g=1;
313        else if (g>31) g=31;
314
```

```
    co=ml_surf->Coord[g];
    d_sp=ml_surf->d_sp[g];
    ang=ml_surf->ang[g];

    if ( fabs(K2E*(sqrt(kx*kx+ky*ky+kz*kz))-mono_energy)<=0.01 ){
      Q=(4*M_PI*K2E*(sqrt(kx*kx+ky*ky+kz*kz))*sin(DEG2RAD*ang))
          /12.398;
#ifdef MCDEBUG_R
      printf("Q1:Q=%g\n",Q);
#endif
    } else {
      Q=sqrt((kx-kxo)*(kx-kxo)+(ky-kyo)*(ky-kyo)+(kz-kzo)*(kz-kzo))
          ;
#ifdef MCDEBUG_R
      printf("Q2:Q=%g\n",Q);
#endif

    }

      while (r<=6000){
            if(Q<(ml_refl->Q[r])) break;
             r++;
            }
          if (r<1)r=1;
          else if (r>6000) r=6000;

    int in=7;
    Refl=ml_refl->R[r-1+in][g+1];
#ifdef MCDEBUG_R
        printf(" d_sp=%g, r=%i, Refl=%g\n \n", d_sp,r,Refl);
#endif

    if (R0==0)
      p*=Refl;
    else if (!R0)
      p*=R0;
}
%}

MCDISPLAY
%{
  int i,j,N=10;
  double w_2=width/2.0;
  double l_2=length/2.0;
  const double x_e[]={w_2,0,0,2*w_2,2*w_2};
  double y_e[]={Y0,0,0,0,0};
  double z_e[]={Z0,0,0,0,0};
  if (s1<s2){
    y_e[1]=Y0-l_2*sin(xi);
    y_e[2]=y_e[3]=Y0+l_2*sin(xi);
    y_e[4]=y_e[1];
    z_e[1]=Z0-l_2*cos(xi);
    z_e[2]=z_e[3]=Z0+l_2*cos(xi);
    z_e[4]=z_e[1];
  }else if (s2<=s1){
    y_e[1]=Y0+l_2*sin(xi);
    y_e[2]=y_e[3]=Y0-l_2*sin(xi);
    y_e[4]=y_e[1];
    z_e[1]=Z0-l_2*cos(xi);
```

```
      z_e[2]=z_e[3]=Z0+l_2*cos(xi);
      z_e[4]=z_e[1];
   }
   double xx[5],yy[5],zz[5];
   for (i=0;i<5;i++){
      CoordTransEM(xx+i,yy+i,zz+i,x_e[i],y_e[i],z_e[i],Z0,Y0,xi);
   }

   multiline(5,xx[1],yy[1],zz[1],xx[2],yy[2],zz[2],xx[3],yy[3],zz
       [3],xx[4],yy[4],zz[4],xx[1],yy[1],zz[1]);
   multiline(3,xx[1],yy[1],zz[1],xx[0],yy[0],zz[0],xx[3],yy[3],zz
       [3]);
   multiline(3,xx[2],yy[2],zz[2],xx[0],yy[0],zz[0],xx[4],yy[4],zz
       [4]);

   for (i=0;i<5;i++){
      CoordTransEM(yy+i,xx+i,zz+i,x_e[i],y_e[i],z_e[i],Z0,Y0,xi);
   }

   multiline(5,xx[1],yy[1],zz[1],xx[2],yy[2],zz[2],xx[3],yy[3],zz
       [3],xx[4],yy[4],zz[4],xx[1],yy[1],zz[1]);
   multiline(3,xx[1],yy[1],zz[1],xx[0],yy[0],zz[0],xx[3],yy[3],zz
       [3]);
   multiline(3,xx[2],yy[2],zz[2],xx[0],yy[0],zz[0],xx[4],yy[4],zz
       [4]);

%}

END
```

```
/*******************************************************
 *
 * McXtrace X-ray tracing software
 * Copyright, All Rights Reserved
 * Risoe-DTU, Roskilde, Denmark
 *
 *
 * Component: Source_gaussian
 *
 * Written by: Jana Baltser & Erik Knudsen
 * Date: April, 2011.
 * Version: 1.0
 * Origin: NBI
 * Release: McXtrace 0.1
 *
 * Gaussian cross-section source
 *
 * A simple source model emitting photons from a gaussian distribution in the X-Y plane with the specified
 * standard deviations (in mm). A square target centered on the beam (Z-axis)
 restricts the beam to that aperture.
 * Further, the beam is restricted to emit photons between E0+-dE keV, or lambda0+-dlambda, whichever is given.
 * Flux is given in the unit
 *
 * Example: Source_gaussian(sig_x=10e-6,sig_y=10e-6,dist=15,sigPr_x=9e-6, sigPr_y=9e-6,E0=sensible, dE=sensible)
 * sig_x - Horizontal source size [microns]
 * sig_y - Vertical source size [microns]
 * dist [meters]
 * sigPr_x - sigmaPrime - angular divergence Horizontal [microrad]
 * sigPr_y - sigmaPrime - angular divergence Vertical [microrad]
 *
 *******************************************************/

DEFINE COMPONENT Source_gaussian
DEFINITION PARAMETERS ()
SETTING PARAMETERS (sig_x=1,sig_y=0,sigPr_x=0,sigPr_y=0,flux=1,dist=1,gamma=0,E0=0, dE=0, lambda0=0,dlambda=-1,phase=-1)
OUTPUT PARAMETERS ()

SHARE
%{
  double Gauss2D(double sigmaX, double sigmaY, double x, double y, double A){
    double F;
    F=A*exp(-(((x*x)/(2.0*sigmaX*sigmaX))+((y*y)/(2.0*sigmaY*sigmaY))));
    return F;
  }
%}

DECLARE
%{
 double l, pmul;
%}

```

```
52
53 INITIALIZE
54 %{
55   if (!sig_y) sig_y=sig_x;
56
57   if (!sigPr_x || !sigPr_y){
58     fprintf(stderr,"Source_gaussian_J (%s): Must define horizontal
         and vertical angular divergences \n",NAME_CURRENT_COMP);
59     exit(0);
60   }
61
62   if (E0){
63     lambda0=2*M_PI/(E0*E2K);
64     if (dE) {
65       dlambda=2*M_PI/(E2K*E0*E0)*dE;
66     } else {
67       dlambda=0;
68     }
69   }else if (!lambda0) {
70     fprintf(stderr,"Source_gaussian (%s): Must specify either
         wavelength or energy distribution\n",NAME_CURRENT_COMP);
71     exit(0);
72   }
73   //calculate the X-ray weight from the flux
74   if (flux){//pmul=flux;
75     pmul=flux*1.0/((double) mcget_ncount());
76   }else{
77     pmul=1.0/((double) mcget_ncount());
78   }
79 %}
80
81
82 TRACE
83 %{
84   double xx,yy,spX,spY,x1,y1,z1;
85   double k;
86   double F1,F2;
87   double dx,dy,dz;
88
89   // initial source area
90   xx=randnorm();
91   yy=randnorm();
92   x=xx*sig_x;
93   y=yy*sig_y;
94   z=0;
95
96   // Gaussian distribution at origin
97   F1=Gauss2D(sig_x,sig_y,x,y,pmul);
98
99   if (dlambda){
100    l=lambda0+dlambda*randnorm();
101  }else{
102    l=lambda0;
103  }
104
105  k=(2*M_PI/l);
106
107  // Beam's footprint at a dist calculation
108  spX=sqrt(sig_x*sig_x+sigPr_x*sigPr_x*dist*dist);
```

```
  spY=sqrt(sig_y*sig_y+sigPr_y*sigPr_y*dist*dist);

  // targeted area calculation
  x1=randnorm()*spX;
  y1=randnorm()*spY;
  z1=dist;

  dx=x1-x;
  dy=y1-y;
  dz=sqrt(dx*dx+dy*dy+dist*dist);

  kx=(k*dx)/dz;
  ky=(k*dy)/dz;
  kz=(k*dist)/dz;

  // Guassian distribution at a distance
  F2=Gauss2D(spX,spY,x1,y1,F1);

    //randomly pick phase
  if (phase==-1){
    phi=rand01()*2*M_PI;
  }else{
    phi=phase;
  }

  //set polarization vector
  Ex=0;Ey=0;Ez=0;
    p*=erf(F2)*pmul;

%}

MCDISPLAY
%{
  double radius;
  if (sig_x<sig_y) radius=sig_x;
  else radius=sig_y;

  magnify("xy");
  circle("xy",0,0,0,radius);
%}

END
```

Appendix C

Instruments source codes

```
/*******************************************************
*  McXtrace instrument definition URL=http://www.mcxtrace.org
*
* Instrument: SAXS-instrument
*
* %Identification
* Written by: Erik Knudsen (erkn@risoe.dtu.dk) & Jana Baltser (jana.baltser@fys.ku.dk)
* Date: 22/03/2011
* Origin: NBI
* Release: McXtrace
* Version: 0.2
*
* Description
* The small-angle scattering (SAXS) instrument generally consists of the following parts:
* the X-ray source (the system includes rotating copper anode and KB multilayer mirrors), a pinhole collimation system and a detector.
*
*
*
* %Parameters
* Gamma [deg] - glancing angle
* dG1 [] -
* dG2 [] -
* S1 [m] - Distance from the source to the multilayer's surface
* S2 [m] - Focal distance of the multilayer
* L [m] - distance between two mirrors
* Energy [keV] - primary energy of the photon beam
* mirror_in - number of mirrors in interaction: mirror_in=0 - no mirrors, mirror_in=1 or 2 -either the first or the second mirror is interacting, mirror_in=3 - both mirrors are involved
*
* %End
*************************************************************/

DEFINE INSTRUMENT SAXS(Gamma=1.2,GammaP=0,S1=.045,S2=.9,Energy=8.05,int miss1=0,int miss2=0,int mirror_in=3)

DECLARE
%{
```

```
36  //  const double source_h=25e-6;                //nominal value: 10
        e-6
37  //  const double source_v=25e-6;
38  //  const double div_h=4e-3;            //nominal value: 9e-3
39  //  const double div_v=4e-3;
40      const double source_h=10e-6;
41      const double source_v=10e-6;
42      const double div_h=9e-3;
43      const double div_v=9e-3;
44     const double slitsize=1.5e-3;        //nominal value: 1.5e-3
45     const double xdet=0.106;
46     const double ydet=0.084;
47
48     #define NXval 619
49     #define NYval 487
50
51     double mwidth=0.02;
52     double mlength=0.06;
53     int term_miss1;
54     int term_miss2;
55     int Scatt;
56     double delta;
57
58     const double detOffSet=3e-2;
59 %}
60
61
62 INITIALIZE
63 %{
64    int term_miss1=miss1;
65    int term_miss2=miss2;
66
67    if (GammaP) Gamma=GammaP/sqrt(2);
68
69
70 %}
71
72 TRACE
73
74 COMPONENT Origin = Progress_bar()
75 AT (0,0,0) ABSOLUTE
76
77 COMPONENT Source=Source_gaussian(sig_x=source_h,sig_y=source_v,
       sigPr_x=div_h,sigPr_y=div_v,dist=0.015,E0=8.07,dE=0.5,flux=1e15)
78 AT(0,0,0) RELATIVE Origin
79 ROTATED (0,0,45) RELATIVE Origin
80
81 COMPONENT energy_BEF=E_monitor(nE=500,filename="energy_BEF.dat",
       xwidth=xdet,yheight=ydet,Emin=7,Emax=9,restore_xray=1)
82 AT(0,0,1e-3) RELATIVE Origin
83
84 COMPONENT mirror_entry_slit=Slit(
85      xwidth=slitsize,yheight=slitsize)
86 AT(0,.63e-3,S1-mlength/2.0) RELATIVE Origin
87 //AT(0,-1e-3,S1-mlength/2.0) RELATIVE Origin
88 ROTATED (0,0,-135) RELATIVE Origin
89
90 COMPONENT mirror_mnt=Arm()
91   AT(0.0,0,S1) RELATIVE Origin
```

```
  ROTATED (0,0,-135) RELATIVE Origin

COMPONENT x_mirror_rot=Arm()
AT(0,0,0) RELATIVE mirror_mnt
ROTATED(-Gamma,0,0) RELATIVE mirror_mnt

COMPONENT y_mirror_rot=Arm()
AT(0,0,0) RELATIVE mirror_mnt
ROTATED (0,Gamma,0) RELATIVE x_mirror_rot


//COMPONENT mirror=TwinKB_ML(theta=Gamma,s1=S1,s2=S2,length=mlength,width=mwidth,R0=0,reflectivity_datafile="Ref_W_B4C.txt")
COMPONENT mirror=TwinKB_ML_v2(theta=Gamma,s1=S1,s2=S2,length=mlength,width=mwidth,R0=0,reflectivity_datafile="NEW_Ref_W_B4C.txt",curvature_datafile="Coord_d_ang.txt")
  WHEN (mirror_in) AT(0,0,0) RELATIVE mirror_mnt
ROTATED (0,0,0) RELATIVE y_mirror_rot

COMPONENT mirror_out=Arm()
  AT(0,0,0) RELATIVE mirror_mnt
ROTATED (2*M_SQRT2*Gamma,0,0) RELATIVE Origin

COMPONENT mirror_exit=Slit(
     xwidth=slitsize,yheight=slitsize)
AT(0,-0.90e-3-2.17e-3,S1+mlength/2.0) RELATIVE Origin
//AT(0,-2.3e-3,S1+mlength/2.0) RELATIVE Origin
ROTATED (0,0,-135) RELATIVE Origin


COMPONENT psd1=PSD_monitor(filename="psd1.dat",xwidth=xdet,yheight=ydet,restore_xray=1,nx=NXval,ny=NYval)
AT (0,0,.160) RELATIVE mirror_out

//COMPONENT energy_psd1_D=E_monitor(nE=500,filename="energy_psd1_D.dat",xwidth=1e-3,yheight=1e-3,Emin=7,Emax =9,restore_xray=1)
//AT (0,0,1e-4) RELATIVE PREVIOUS

//COMPONENT energy_psd1_SR=E_monitor(nE=500,filename="energy_psd1_SR.dat",xwidth=2e-3,yheight=2e-3,Emin=7,Emax =9,restore_xray=1)
//AT (2.5e-3,2.5e-3,1e-4) RELATIVE PREVIOUS

COMPONENT psd2=PSD_monitor(filename="psd2.dat",xwidth=xdet,yheight=ydet,restore_xray=1,nx=NXval,ny=NYval)
AT (0,0,.310) RELATIVE mirror_out

COMPONENT psd3=PSD_monitor(filename="psd3.dat",xwidth=xdet,yheight=ydet,restore_xray=1,nx=NXval,ny=NYval)
AT (0,0,.460) RELATIVE mirror_out

COMPONENT psd4=PSD_monitor(filename="psd4.dat",xwidth=xdet,yheight=ydet,restore_xray=1,nx=NXval,ny=NYval)
AT (0,0,.610) RELATIVE mirror_out

COMPONENT psd5=PSD_monitor(filename="psd5.dat",xwidth=xdet,yheight=ydet,restore_xray=1,nx=NXval,ny=NYval)
AT (0,0,.760) RELATIVE mirror_out

```

```
COMPONENT psd6=PSD_monitor(filename="psd6.dat",xwidth=xdet,yheight=ydet,restore_xray=1,nx=NXval,ny=NYval)
AT (0,0,.910) RELATIVE mirror_out

COMPONENT psd7=PSD_monitor(filename="psd7.dat",xwidth=xdet,yheight=ydet,restore_xray=1,nx=NXval,ny=NYval)
AT (0,0,1.060) RELATIVE mirror_out
// now - inside the vacuum chamber mode
COMPONENT psd_in1=PSD_monitor(filename="psd_in1.dat",xwidth=xdet,yheight=ydet,restore_xray=1,nx=NXval,ny=NYval)
AT (0,0,1.540) RELATIVE mirror_out

//COMPONENT energy_AFT=E_monitor(nE=500,filename="energy_AFT.dat",xwidth=1e-2,yheight=1e-2,Emin=7,Emax =9,restore_xray=1)
//AT (0,0,1e-3) RELATIVE PREVIOUS

//COMPONENT energy_AFT_SR=E_monitor(nE=500,filename="energy_AFT_SR.dat",xwidth=2e-2,yheight=2e-2,Emin=7,Emax =9,restore_xray=1)
//AT (2e-2,2e-2,1e-4) RELATIVE PREVIOUS

COMPONENT psd_in2=PSD_monitor(filename="psd_in2.dat",xwidth=xdet,yheight=ydet,restore_xray=1,nx=NXval,ny=NYval)
AT (0,0,.15) RELATIVE psd_in1

COMPONENT psd_in3=PSD_monitor(filename="psd_in3.dat",xwidth=xdet,yheight=ydet,restore_xray=0,nx=NXval,ny=NYval)
AT (0,0,0.30) RELATIVE psd_in1

COMPONENT psd_in4=PSD_monitor(filename="psd_in4.dat",xwidth=xdet,yheight=ydet,restore_xray=0,nx=NXval,ny=NYval)
AT (0,0,0.45) RELATIVE psd_in1
COMPONENT psd_in5=PSD_monitor(filename="psd_in5.dat",xwidth=xdet,yheight=ydet,restore_xray=0,nx=NXval,ny=NYval)
AT (0,0,0.60) RELATIVE psd_in1
COMPONENT psd_in6=PSD_monitor(filename="psd_in6.dat",xwidth=xdet,yheight=ydet,restore_xray=0,nx=NXval,ny=NYval)
AT (0,0,0.75) RELATIVE psd_in1
COMPONENT psd_in7=PSD_monitor(filename="psd_in7.dat",xwidth=xdet,yheight=ydet,restore_xray=0,nx=NXval,ny=NYval)
AT (0,detOffSet,0.90) RELATIVE psd_in1
COMPONENT psd_in8=PSD_monitor(filename="psd_in8.dat",xwidth=xdet,yheight=ydet,restore_xray=0,nx=NXval,ny=NYval)
AT (0,detOffSet,1.05) RELATIVE psd_in1
// if to rescale the detector, since the single reflections are outside the monitor, xdet+0.05, ydet+.07
COMPONENT psd_in9=PSD_monitor(filename="psd_in9.dat",xwidth=xdet,yheight=ydet,restore_xray=0,nx=NXval,ny=NYval)
AT (0,detOffSet,1.2) RELATIVE psd_in1

COMPONENT psd_in10=PSD_monitor(filename="psd_in10.dat",xwidth=xdet,yheight=ydet,restore_xray=0,nx=NXval,ny=NYval)
AT (0,detOffSet,1.35) RELATIVE psd_in1

COMPONENT psd_in11=PSD_monitor(filename="psd_in11.dat",xwidth=xdet,yheight=ydet,restore_xray=0,nx=NXval,ny=NYval)
AT (0,detOffSet,1.41) RELATIVE psd_in1


END
```

```
/*******************************************************
* McXtrace instrument definition URL=http://www.mcxtrace.org
*
* Instrument: Transfocator_ID11
*
* Written by: Jana Baltser
* Date: July 2011
* Origin: NBI & BNL
* Release: McXtrace
* Version: 0.2
*
* Description:
* Transfocator is a device consisting of a number of compound refractive lenses.
* The present instrument file simulates the transfocator as a low-tech monochromator.
* An input polychromatic radiation is monochromatised by a slit, which is placed at
* the focal length of the primary radiation. The size of the slit varies. The degree
* of monochromatisation by various slit openings is simulated by the present instrument.
*
*
* Parameters:
* L [m] -        distance between the source and the transfocator's centre
* Energy [keV]- the primary radiation energy
* dEnergy [keV]- the energy range
* L2 [m] -       distance between the source and the slit
* D [m] -        length of the Be CRL
*
* End
*******************************************************/

DEFINE INSTRUMENT Transfocator_ID11(L=31.47545, Energy=35.61, dEnergy=0, L2=41.5, D=21.8e-3)

DECLARE
%{
        const double source_h=48.23e-6;
        const double source_v=9.525e-6;
        const double div_h=100.04e-6;
        const double div_v=4.33e-6;

        const double slit_x=200e-6;
        const double slit_y=20e-6;
%}

INITIALIZE
%{
%}

TRACE

COMPONENT Origin=Progress_bar()
AT (0,0,0) ABSOLUTE

```

```
COMPONENT Source=Source_gaussian(sig_x=source_h, sig_y=source_v,
    sigPr_x=div_h, sigPr_y=div_v, E0=Energy, dE=dEnergy, distance=L,
    flux=7e18)
AT (0,0,0) RELATIVE Origin

COMPONENT Emon0=E_monitor(nE=500,filename="Emon0.dat",xwidth=12e-3,
    yheight=2e-3,Emin=33,Emax=37,restore_xray=1)
AT (0,0,1e-2) RELATIVE Origin

COMPONENT Aperture=Slit(radius=1e-3)
AT (0,0,L-1e-1) RELATIVE Origin

COMPONENT Det0=PSD_monitor(filename="psd0.dat",xwidth=12e-3,yheight
    =2e-3,restore_xray=1,nx=500,ny=500)
AT (0,0,L-1e-2) RELATIVE Origin

COMPONENT IVT_Be=Lens_parab(r=.2e-3,yheight=1e-3,xwidth=1e-3,d=.05e
    -3,material_datafile="Be.txt",N=16)
AT (0,0,L) RELATIVE Origin

COMPONENT IVT_Al=Lens_parab(r=.2e-3,yheight=1e-3,xwidth=1e-3,d=.02e
    -3,material_datafile="Al.txt",N=21)
AT (0,0,L+D) RELATIVE Origin

COMPONENT Det_aux=PSD_monitor(filename="psd_aux.dat",xwidth=.08e-3,
    yheight=.08e-3,restore_xray=1,nx=500,ny=500)
AT (0,0,L2-1e-5) RELATIVE Origin

COMPONENT Slit=Slit(xwidth=slit_x, yheight=slit_y)
AT (0,0,L2) RELATIVE Origin

COMPONENT Det_aft=PSD_monitor(filename="psd_aft.dat",xwidth=80e-6,
    yheight=80e-6,restore_xray=1,nx=500,ny=500)
AT (0,0,L2+1e-5) RELATIVE Origin

COMPONENT Emon=E_monitor(nE=500,filename="Emon.dat",xwidth=2e-3,
    yheight=2e-3,Emin=33,Emax=37,restore_xray=1)
AT (0,0,L2+1e-2) RELATIVE Origin

END
```

```
/*******************************************************
* McXtrace instrument definition URL=http://www.mcxtrace.org
*
* Instrument: APS_test4
*
* Written by: Jana Baltser
* Date: January 2012
* Origin: NBI
* Release: McXtrace
* Version: 0.2
*
* Description:
* This is the modelling of experimental results of the beamtime at APS in December 2011.
* test4 - vertical focusing with a 1D Be CRL (N=4) @ 9.99 keV
*         horizontal focusing wiht a KL at pos2
*
* Parameters:
*  L  [m] - distance from the source to the SS1 - secondary source aperture.
*  L2 [m] - position of the CRL from the centre of the undulator straight section.
*  L3 [m] - location of Slits2 from the centre of the undulator straight section.
*  L4 [m] - pos1 of the kinoform lens.
*  L5 [m] - pos2 of the kinoform lens.
*  L6 [m] - distance to the Yag crystal (the distance is considered as the detector position, due the fact that the optical axis is rotated 90 degrees by a mirror right at the position of the Yag crystal.)
*  Energy [keV] - primary energy used at the beamline.
*
* End
*******************************************************/

DEFINE INSTRUMENT Exp_test4(L1=36,L2=36.25,L3=70.93,L4=71.13,L5=71.30,L6=74.98,Energy=9.99)

DECLARE
%{
      const double source_h=129e-6;
      const double source_v=21e-6;
      const double div_h=21.7e-6;
      const double div_v=2.7e-6;

      const double slit1_x=1e-2;
      const double slit1_y=1e-2;
      const double slit2_x=1e-2;
      const double slit2_y=1e-2;

      const double det_x=1715e-6;
      const double det_y=1372e-6;

%}

INITIALIZE
%{
%}
```

```

TRACE

COMPONENT Origin=Progress_bar()
AT (0,0,0) ABSOLUTE

COMPONENT Source=Source_gaussian(sig_x=source_h,sig_y=source_v,
    sigPr_x=div_h,sigPr_y=div_v,E0=Energy,dE=0.1,
 dist=L1,flux=3.55e9)
AT (0,0,0) RELATIVE Origin

COMPONENT addDet=PSD_monitor(filename="addDet.dat",xwidth=det_x,
    yheight=det_y,nx=1280,ny=1024,restore_xray=1)
AT (0,0,L1-1e-5) RELATIVE Origin

COMPONENT Slit1=Slit(xwidth=slit1_x,yheight=slit1_y)
AT (0,0,L1) RELATIVE Origin

COMPONENT CRL_v=Lens_parab_Cyl_rough(r=.5e-3,yheight=1.2e-3,xwidth
    =1.2e-3,d=.08e-3,N=4,material_datafile="Be.txt",rough_xy=0,
    rough_z=0)
AT (0,0,L2) RELATIVE Origin

COMPONENT Slit2=Slit(xwidth=6e-4,yheight=.1e-3)
AT (0,0,L3) RELATIVE Origin

COMPONENT KF1=Lens_Kinoform(yheight=.1e-3,xwidth=5.268e-4,
    material_datafile="Si.txt")
AT (0,0,L5) RELATIVE Origin

COMPONENT Det=PSD_monitor(filename="test4_det.dat",xwidth=det_x,
    yheight=det_y,nx=1280,ny=1024,restore_xray=1)
AT (0,0,L6) RELATIVE Origin

COMPONENT Det1=PSD_monitor(filename="Det1.dat",xwidth=det_x,yheight
    =det_y,nx=1280,ny=1024,restore_xray=1)
AT (0,0,L6+2) RELATIVE Origin

END
```

Bibliography

[1] O. Chubar, P. Elleaume, and A. Snigirev. Phase analysis and focusing of synchrotron radiation. *Nucl. Instrum. Methods Phys. Res.*, A 435:495, 1999.

[2] J. Bahrdt. Wave-front propagation: design code for synchrotron radiation beam lines. *Appl. Opt.*, 36(19):4367, 2007.

[3] J. Bahrdt, U. Flechsig, S. Gerhardt, and I. Schneider. PHASE: a universal software package for the propagation of time-dependent coherent light pulses along grazing incidence optics. *Proc. of SPIE*, 81410E:1–10, 2011.

[4] C. Welnak, G.J. Chen, and F. Cerrina. SHADOW: a synchrotron radiation and X-ray optics simulation tool. *Rev. Sci. Instrum.*, A 347:344–347, 1994.

[5] B. Lai, K. Chapman, and F. Cerrina. *Nucl. Instr. Meth.*, A 246:544, 1986.

[6] F. Schäfers. RAY - the Bessy raytracing program. *Springer Series in modern optical sciences: Modern Developments in X-ray and Neutron Optics*, 137:9–41, 2008.

[7] K. Wille. *The Physics of Particle Accelerators.* Oxford University Press, 2005.

[8] B. Lengeler, C. Schroer, B. Benner, A. Gerhardus, T. F. Günzler, M. Kuhlmann, J. Meyer, and C. Zimprich. Parabolic refractive X-ray lenses. *J. Synchrotron Rad.*, 9:119–124, 2002.

[9] J. Als-Nielsen and D. McMorrow. *Elements of Modern X-Ray Physics.* John Wiley & Sons Ltd., 2001.

[10] C. Kittel. *Introduction to solid state physics.* John Wiley & Sons, Inc., 2005.

[11] A. Thompson and D. Vaughan et al. *X-ray data booklet.* Lawrence Berkeley National Laboratory, 2001.

[12] Website. `mcnp-green.lanl.gov`.

[13] Website. `paseeger.com`.

[14] K. Lefmann, P. Willendrup, L. Udby, B. Lebech, K. Mortensen, J. Birk, K. Klenø, E. Knudsen, P. Christiansen, J. Saroun, J. Kulda, U. Filges, M. Konnecke, P. Trigenna-Piggott, J. Peters, K. Lieutenant, G. Szigmond,

P. Bentley, and E. Farhi. Virtual experiments: the ultimate goal of neutron ray-tracing simulations. *J. Neutron Research*, 16:97–111, 2008.

[15] K. Lefmann and K. Nielsen. Mcstas, a general software package for neutron ray-tracing simulations. *Neutron News*, 10(3):20–23, 1999.

[16] G. Zsigmond and K. Lieutenant abd F. Mezei. *Neutron news*, 13(4):11, 2002.

[17] J. Saroun and J. Kulda. *Physica B*, 1102:234–236, 1997.

[18] W.-T. Lee, X.-L. Wang, J.L. Robertson, F. Klose, and C. Rehm. *Appl. Phys.*, A 74:S1502, 2002.

[19] McStas website. `www.mcstas.org`.

[20] F. James. Monte Carlo theory and practice. *Rep. Prog. Phys.*, 43:1145, 1980.

[21] H. W. Jensen et al. Monte Carlo Ray Tracing. Course notes, 2003.

[22] G. H. Spencer and M. V. R. K. Murty. General ray-tracing procedure. *J. Opt. Society of America*, 52 (6):672–678, 1962.

[23] B. Roe. *Probability and statistics in experimental physics*. Springer Verlag, 2001.

[24] A. Snigirev, V. Kohn, I. Snigireva, and B. Lengeler. A compound refractive lens for focusing high energy x-rays. *Nature (London)*, 384:49, 1996.

[25] E. Bergbäck Knudsen, A. Prodi, J. Baltser, M. Thomsen, P. K. Willendrup, M. Sanchez del Rio, C. Ferrero, R. Feidenhans'l, K. Mortensen, M. Meedom Nielsen, H. Friis Poulsen, E. Farhi, S. Schmidt, and K. Lefmann. McXtrace - a general software package for simulation of X-ray optics, beamlines, and experiments. *J. of Applied Crystallography*, in press, 2013.

[26] A. Prodi, E. Knudsen, P. Willendrup, S. Schmidt, C. Ferrero, R. Feidenhans'l, and K. Lefmann. A Monte Carlo approach for simulating the propagation of partially coherent X-ray beams. *Proc. of SPIE*, 814108, 2011.

[27] D. Attwood. Synchrotron radiation for material science application, 2007.

[28] R.P. Walker. Near field effects in off-axis undulator radiation. *Nucl. Instrum. Methods Phys. Res.*, A 246:71–76, 1986.

[29] O. Chubar and P. Elleaume. Accurate and efficient computation of synchrotron radiation in the near field region. *Proc. EPAC-98*, pages 1177–1179, 1998.

[30] M. Born and E. Wolf. *Principles of Optics, fourth ed.* Pergamon Press, 1968.

[31] O. Chubar, Y. S. Chu, K. Kaznatcheev, and H. Yan. Application of partially coherent wavefront propagation calculations for design of coherence-preserving synchrotron radiation beamlines. *Nuclear Instrum. and Methods in Physics Research*, A 649:118–122, 2011.

[32] A. Fluerasu, O. Chubar, K. Kaznatcheev, J. Baltser, K. Evans-Lutterodt L. Wiegart, M. Carlucci-Dayton, and L. Berman. Analysis of the optical design of the NSLS-II coherent hard x-ray beamline. *Proceedings of the SPIE*, 8141, 2011.

[33] O. Glatter and O. Kratky. *Small Angle X-ray Scattering.* Academic Press, 1982.

[34] L.A. Feigin and D. I. Svergun. *Structure Analysis by Small-Angle X-ray and Neutron Scattering.* Plenum Press, 1987.

[35] Website. `http://bl1231.als.lbl.gov/2011/07/course\_on\_saxs\_from\_.php`.

[36] A. Paar. The SAXS guide. Getting acquainted with the principles, 2011.

[37] E. Knudsen, A. Prodi, P. K. Willendrup, and K. Lefmann. Component manual for the x-ray-tracing package mcxtrace, 2011.

[38] Osmic Inc. Confocal Max-Flux Optics, 2011.

[39] G. Vaughan, J. Wright, A. Bytchkov, M. Rossat, H. Gleyzolle, I. Snigireva, and A. Snigirev. X-ray transfocators: focusing devices based on compound refractive lenses. *J. Synchrotron Rad.*, 18:125–133, 2011.

[40] A. Snigirev, I. Snigireva, G. Vaughan, J. Wright, M. Rossat, A. Bytchkov, and C. Curfs. High energy x-ray transfocator based on al parabolic lenses for focusing and collimation. *J. Phys. Conf. Ser.*, 186:012073, 2009a.

[41] M. Rossat, G. B. M. Vaughan, A. Snigirev, J. P. Wright, A. Bytchkov, Y. Dabin, and L. Zhang. Design and technical aspects of a new in vacuum transfocator at esrf beamline id11. *AIP Conf. Proc.*, 1234:744–747, 2009.

[42] B. Lengeler, C. Schroer, J. Tummler, B. Benner, M. Richwin, A. Snigirev, I. Snigireva, and M. Drakopoulos. Imaging by parabolic refractive lenses in the hard x-ray range. *J. Synchrotron Rad.*, 6:1153–1167, 1999.

[43] O. Chubar, P. Elleaume, S. Kuznetsov, and A. Snigirev. Physical optics computer code optimized for synchrotron radiation. *Proc. SPIE*, 4769:145, 2002.

[44] O. Chubar, L. Berman, Y.S. Chu, A. Fluerasu, S. Hilbert, M. Idir, K. Koznatcheev, D. Shapiro, Q. Shen, and J. Baltser. Development of partially-coherent wavefront propagation simulation methods for 3d and 4th generation synchrotron radiation sources. *Proc. SPIE*, 8141:to be published, 2011.

[45] O. Chubar, A. Fluerasu, Y. S. Chu, L. Berman, L. Wiegart, W.-K. Lee, and J. Baltser. Experimental characterization of X-ray transverse coherence in the presence of the beam transport optics. *Journal of Physics, Conf. Series*, in press, 2013.

[46] A. Stein, K. Evans-Lutterodt, N. Bozovic, and A. Taylor. Fabrication of silicon kinoform lenses for hard x-ray focusing by electron beam lithography and deep reactive ion etching. *J. Vac. Sci. Technol. B*, 26(1):122–127, 2008.

[47] Website. `flash.desy.de`.

[48] Anette Vickery. Optical elements for hard X-ray radiation. PhD thesis, 2007.